

COMPUTATIONAL FLUID DYNAMICS ANALYSIS AND NOISE MODELING
OF JETS WITH INTERNAL FORCED MIXERS

A Thesis
Submitted to the Faculty
of
Purdue University
by
Loren Armstrong Garrison

In Partial Fulfillment of the
Requirements for the Degree
of
Doctor of Philosophy

May 2006

Purdue University
West Lafayette, Indiana

ACKNOWLEDGMENTS

I would like to thank my advisors Dr. Anastasios Lyrnitzis and Dr. Gregory Blaisdell for their guidance throughout my graduate studies. I would also like to thank Dr. Marc Williams and Dr. Luc Mongeau for serving on my thesis committee.

I would like to gratefully acknowledge my funding for this research work, which has been provided by the Purdue Research Foundation and through grants from the Aeroacoustics Research Consortium (AARC). The RANS calculations were performed on the School of Aeronautics and Astronautics Linux cluster which was acquired by a Defense University Research Instrumentation Program (DURIP) grant sponsored by ARO.

I would like to thank Dr. Brian Tester and Dr. Mike Fisher at the Institute of Sound and Vibration Research who have invaluabley enriched my knowledge of jet noise through the collaborations on the AARC project. Their advice and guidance throughout the AARC project is gratefully acknowledged. I would also like to thank Bill Dalton at the Rolls-Royce Corporation for the advice and guidance that he has provided both during my graduate studies and during my internships at the Rolls-Royce Corporation. I would like to thank Nick Georgiadis at the NASA Glenn Research Center for his assistance with the WIND flow solver (in particular his advice concerning the use and modification of the turbulence models).

I would like to thank the many colleagues and officemates that I have had as a graduate student at Purdue. In particular, I would like to thank Phoi-Tack (Charlie) Lew and Ali Uzun who have been especially helpful during my graduate career. I would like to thank my wife, Heather, for her patience during my doctoral studies. Finally, I would like to thank my parents for providing me with an endless supply of love and encouragement.

TABLE OF CONTENTS

	Page
LIST OF TABLES	v
LIST OF FIGURES	vi
NOMENCLATURE	xii
ABSTRACT	xv
1 Introduction	1
1.1 Motivation	1
1.2 Jet Noise Prediction Methods	1
1.3 Previous RANS Analysis of Jet Flows	8
1.4 Objectives of the Present Research	15
2 RANS CFD Analysis	19
2.1 Objectives	19
2.2 Lobed Mixer Experimental Data	19
2.3 Computational Details	29
2.4 Confluent Mixer Analysis	33
2.4.1 Grid Sensitivity	33
2.4.2 Turbulence Model Sensitivity	35
2.4.3 Final Confluent Mixer Results	37
2.5 Lobed Mixer Analysis	50
2.5.1 Grid Sensitivity	50
2.5.2 Final Lobed Mixer Results	53
3 Two-Source Noise Model	71
3.1 Methodology	71
3.2 CFD-Based Noise Model Parameters	79
3.3 Model Performance	84

	Page
4 Multi-Source Noise Model	91
4.1 Methodology	91
4.2 Model Parameters	96
4.3 Single Section Multi-Source Model Predictions	101
4.4 Four Section Multi-Source Model Predictions	107
5 High Mach Number Lift Noise Source	115
6 Conclusions and Recommendations for Future Work	123
6.1 Conclusions	123
6.2 Recommendations for Future Work	125
LIST OF REFERENCES	129
APPENDICES	
A PIV Data Processing	139
B Grid Generation	145
VITA	151

LIST OF TABLES

Table	Page
2.1 Mixer properties	23
2.2 Nozzle properties	23
2.3 Nominal set point operating conditions	23
2.4 Nominal set point characteristic jet properties	24
2.5 Grid point distribution for the standard confluent mixer grid (G1) . .	33
2.6 Grid point distribution for the standard 20UH mixer grid (G1)	51
3.1 Two-source model empirically derived parameters using the ARP876C single jet prediction method for set point 110.	77
3.2 Two-source model empirically derived parameters using the ESDU single jet prediction method for set point 110.	78
3.3 CFD-based two-source model parameters for set point 110.	82
4.1 CFD-based upstream region characteristic jet properties.	101

LIST OF FIGURES

Figure	Page
2.1 Aeroacoustic Propulsion Laboratory facility at the NASA Glenn Research Center.	25
2.2 Sample configuration of an internal forced mixer and nozzle.	26
2.3 Mixer geometries: (a) confluent mixer, (b) 12CL, (c) 12UM, (d) 12UH, (e) 20UH, (f) 20DH.	27
2.4 Definition of the forced mixer penetration height: (a) lobed mixer trailing edge profile and (b) lobed mixer side view.	28
2.5 Nozzle geometry profiles: (a) L0, L1, and L2 nozzles (b) L2 nozzle (c) L1 nozzle and (d) L0 (baseline) nozzle.	28
2.6 Schematic of the boundary conditions.	32
2.7 Schematic of the confluent mixer geometry with the baseline L0 nozzle.	38
2.8 Zone layout for the confluent mixer grids.	39
2.9 Nozzle interior region of the standard (G1) confluent mixer grid.	39
2.10 Variation of y_2^+ along the nozzle interior wall for the confluent mixer at set point 312 for the G1, G2 and G3 grids.	40
2.11 Boundary layer profiles at the nozzle exit plane for the confluent mixer at set point 312 for the G1, G2 and G3 grids.	40
2.12 Centerline velocities for the confluent mixer at set point 312 for the G1, G2 and G3 grids.	41
2.13 Velocity profiles for the confluent mixer at set point 312 for the G1, G2 and G3 grids at $X/D =$ (a) 0.1, (b) 1.0, (c) 2.0, (d) 5.0, (e) 7.0, (f) 10.0. Solid black line is the PIV data; other line types are the same as Figure 2.12.	42
2.14 Turbulence intensity profiles for the confluent mixer at set point 312 for the G1, G2 and G3 grids at $X/D =$ (a) 0.1, (b) 1.0, (c) 2.0, (d) 5.0, (e) 7.0, (f) 10.0. Solid black line is the PIV data; other line types are the same as Figure 2.12.	43
2.15 Centerline velocities for the confluent mixer (G1 grid) at set point 312 for various turbulence models.	44

Figure	Page
2.16 Centerline velocities for the confluent mixer (G1 grid) at set point 312 for WIND and FLUENT with the SST turbulence model.	44
2.17 Velocity profiles for the confluent mixer (G1 grid) at set point 312 for various turbulence models at $X/D =$ (a) 0.1, (b) 1.0, (c) 2.0, (d) 5.0, (e) 7.0, (f) 10.0. Solid black line is the PIV data; other line types are the same as Figure 2.15.	45
2.18 Turbulence intensity profiles for the confluent mixer (G1 grid) at set point 312 for various turbulence models at $X/D =$ (a) 0.1, (b) 1.0, (c) 2.0, (d) 5.0, (e) 7.0, (f) 10.0. Solid black line is the PIV data; other line types are the same as Figure 2.15.	46
2.19 Velocity profiles for the conflent mixer at set point 5000 scaled with η ; (a) CFD; (b) PIV.	47
2.20 Turbulence intenstity profiles for the conflent mixer at set point 5000 scaled with η ; (a) CFD; (b) PIV. Line types are the same as Figure 2.19.	48
2.21 Turbulence intenstity profiles for the conflent mixer at set point 312 scaled with R/D ; (a) CFD; (b) PIV. Line types are the same as Figure 2.19.	49
2.22 Schematic of the s typical lobed mixer geometry with the baseline L0 nozzle.	56
2.23 Zone layout for the lobed mixer grids.	56
2.24 Nozzle interior region of the standard (G1) 20UH mixer grid. Every fourth azimuthal grid point is shown for clarity.	57
2.25 Comparison of the axial vorticity at the nozzle exit plane for the G1, G2, and G3 20UH mixer grids.	58
2.26 Comparison of the turbulence intensities at the nozzle exit plane for the G1, G2, and G3 20UH mixer grids.	59
2.27 Comparison of the peak turbulence intensities in the plume for the G1, G2, and G3 20UH mixer grids.	60
2.28 Comparison of the CFD and PIV mean streamwise velocities in the jet plume at $X/D = 0.1$ and $X/D = 1.0$	61
2.29 Comparison of the CFD and PIV turbulence intensities in the jet plume at $X/D = 0.1$ and $X/D = 1.0$	62

Figure	Page
2.30 Comparison of the CFD and PIV azimuthally averaged profiles of mean streamwise velocity and turbulence intensity at various axial locations in the jet plume for the 12CL mixer; solid line, PIV data; dash-dot line, CFD data.	63
2.31 Comparison of the CFD and PIV azimuthally averaged profiles of mean streamwise velocity and turbulence intensity at various axial locations in the jet plume for the 12UM mixer; solid line, PIV data; dash-dot line, CFD data.	64
2.32 Comparison of the CFD and PIV azimuthally averaged profiles of mean streamwise velocity and turbulence intensity at various axial locations in the jet plume for the 12UH mixer; solid line, PIV data; dash-dot line, CFD data.	65
2.33 Comparison of the CFD and PIV azimuthally averaged profiles of mean streamwise velocity and turbulence intensity at various axial locations in the jet plume for the 20UH mixer; solid line, PIV data; dash-dot line, CFD data.	66
2.34 Comparison of the CFD and PIV azimuthally averaged profiles of mean streamwise velocity and turbulence intensity at various axial locations in the jet plume for the 20DH mixer; solid line, PIV data; dash-dot line, CFD data.	67
2.35 Comparison of the PIV turbulence intensities in the jet plume for the 12-lobed mixers at set point 312.	68
2.36 Comparison of the CFD turbulence intensities in the jet plume for the 12-lobed mixers at set point 312.	69
3.1 Structure of a jet plume with an internal forced mixer.	76
3.2 F_U and F_D functions for $f_c = 1000$ Hz	76
3.3 Spectral filter functions for $f_c = 1000$ Hz	77
3.4 Axial variation of the peak turbulence intensities in the jet plume.	82
3.5 CFD and PIV estimated upstream turbulence enhancement for set point 312.	83
3.6 Two-source model noise predictions for the 12CL mixer at set point 110.	86
3.7 Two-source model noise predictions for the 12UM mixer at set point 110.	87

Figure	Page
3.8 Two-source model noise predictions for the 12UH mixer at set point 110.	88
3.9 Two-source model noise predictions for the 20UH mixer at set point 110.	89
3.10 Two-source model noise predictions for the 20DH mixer at set point 110.	90
4.1 Structure of a jet plume with an internal forced mixer.	94
4.2 Sample source distribution functions for Strouhal numbers 0.5, 1, and 5.	94
4.3 Sample spectral filter functions for the multi-source noise model.	95
4.4 Sample spectral filter function attenuations for the multi-source noise model.	95
4.5 Schematic of the numerical estimation of the main jet shear layer inside edge location.	98
4.6 Sample velocity profiles for 12CL mixer; shear layer inside edge locations are marked with a circle.	98
4.7 Axial variation of the main jet shear layer inside edge location.	99
4.8 Axial variation of the characteristic jet velocity scale.	99
4.9 Axial variation of the centerline velocity.	100
4.10 Two-source model noise predictions for the 12CL mixer at set point 110 using CFD-based velocity and temperature scales.	102
4.11 Two-source model noise predictions for the 12UM mixer at set point 110 using CFD-based velocity and temperature scales.	103
4.12 Two-source model noise predictions for the 12UH mixer at set point 110 using CFD-based velocity and temperature scales.	104
4.13 Two-source model noise predictions for the 20UH mixer at set point 110 using CFD-based velocity and temperature scales.	105
4.14 Two-source model noise predictions for the 20DH mixer at set point 110 using CFD-based velocity and temperature scales.	106
4.15 Characteristic jet properties for the multi-source model predictions with four upstream sections.	108
4.16 Multi-source model noise predictions for the 12CL mixer at set point 110.	109

Figure	Page
4.17 Multi-source model noise predictions for the 12UM mixer at set point 110.	110
4.18 Multi-source model noise predictions for the 12UH mixer at set point 110.	111
4.19 Multi-source model noise predictions for the 20UH mixer at set point 110.	112
4.20 Multi-source model noise predictions for the 20DH mixer at set point 110.	113
5.1 Far-field Sound Pressure Level spectra at 70° for the 12UM mixer with the L0 nozzle and the 12CL mixer with the L0, L1, and L2 nozzles at set point 310.	118
5.2 Axial variation of the angle between the interior nozzle wall and the jet axis for the L0, L1, and L2 nozzles.	118
5.3 CFD Mach number contours for the 12UM mixer in the lobe peak azimuthal plane at set point 312 with the (a) L0 nozzle, (b) L1 nozzle, and (c) L2 nozzle.	119
5.4 Axial Mach number variation in lobe peak azimuthal plane of the 12UM mixer with the L0 nozzle at set point 312 (a) Mach number contours and profile locations (b) Mach number profiles (along lines offset from the nozzle wall).	120
5.5 Axial Mach number variation in lobe peak azimuthal plane of the 12UM mixer with the L1 nozzle at set point 312 (a) Mach number contours and profile locations (b) Mach number profiles (along lines offset from the nozzle wall).	120
5.6 CFD turbulence kinetic energy upstream of the normal shock for the L0 nozzle with the (a) 12CL mixer, (b) 12UM mixer, and (c) 12UH mixer at set point 310; bold contours, supersonic region; thin contours, subsonic region.	121
5.7 Estimated HML noise source strength on the shock surface for the L0 nozzle with the (a) 12CL mixer, (b) 12UM mixer, and (c) 12UH mixer at set point 310.	121
5.8 Estimated HML noise source peak frequencies for the 12CL mixer with the L0 nozzle at set point 310.	122
5.9 Estimated HML noise source directivity at for the 12CL mixer with the L0 nozzle at set point 310.	122

Figure	Page
A.1 PIV data mean streamwise velocities in the jet plume for the 12CL mixer at set point 310.	142
A.2 PIV data jet centerline location results for the 12CL mixer at set point 310.	142
A.3 PIV data final averaged jet centerline location results: (a) vertical shift, (b) horizontal shift.	143
A.4 Comparison of the Cartesian and cylindrical PIV data grids (every 3 rd grid point is shown).	144
B.1 Zone arrangement for the confluent mixer grid.	148
B.2 Boundary grid point specification for zones 1 and 2.	148
B.3 Boundary grid point specification for zone 3.	149
B.4 Boundary grid point specification for zone 4.	149
B.5 Boundary grid point specification for zone 5.	150
B.6 Boundary grid point specification for zone 6 (every other grid point is shown).	150

NOMENCLATURE

Roman Symbols

a	Speed of Sound
A	Jet Area
D	Jet Diameter
f	Frequency
F_U	Spectral Filter Function (Upstream Region)
F_D	Spectral Filter Function (Downstream Region)
H	Lobe Penetration Height
k	Turbulence Kinetic Energy
L_s	Lobe Scallop Length
M	Mach Number
M_a	Acoustic Mach Number (V/a_o)
p	Pressure
R	Radial Coordinate
St	Strouhal Number
T	Jet Static Temperature
V	Jet Velocity
X	Axial Coordinate

Greek Symbols

α	Peak Turbulence Intensity
β	Area Ratio (A_s/A_p)
δ	Density Ratio (ρ_s/ρ_p)
ϵ	Turbulence Dissipation Rate
γ	Ratio of Specific Heats

Γ_U	Ratio of Peak Turbulence Intensities (Upstream Region)
Γ_D	Ratio of Peak Turbulence Intensities (Downstream Region)
η	Shear Layer Similarity Parameter
λ	Velocity Ratio (V_s/V_p)
θ	Far-field Angular Location
ρ	Density
ω	Specific Turbulence Dissipation Rate

Subscripts

$(\cdot)_D$	Downstream Region Property
$(\cdot)_f$	Flight Stream Property
$(\cdot)_m$	Mixed Jet Property
$(\cdot)_o$	Ambient Property
$(\cdot)_p$	Primary Flow Property
$(\cdot)_s$	Secondary Flow Property
$(\cdot)_U$	Upstream Region Property

Abbreviations

AAPL	Aeroacoustic Propulsion Laboratory
CFD	Computational Fluid Dynamics
DNS	Direct Numerical Simulation
ESDU	Engineering Sciences Data Unit
HFJER	High Flow Jet Exit Rig
HML	High Mach number Lift
LES	Large Eddy Simulation
MBGK	Mani, Balsa, Glibe, Khavaran
NATR	Nozzle Acoustic Test Rig
<i>NPR</i>	Nozzle Pressure Ratio
<i>NTR</i>	Nozzle Temperature Ratio

OASPL	Overall Sound Pressure Level
PIV	Particle Image Velocimetry
RANS	Reynolds Averaged Navier-Stokes
SAE	Society of Automotive Engineers
<i>SPL</i>	Sound Pressure Level

ABSTRACT

Garrison, Loren Armstrong. Ph.D., Purdue University, May, 2006. Computational Fluid Dynamics Analysis and Noise Modeling of Jets with Internal Forced Mixers. Major Professors: Anastasios S. Lyrintzis and Gregory A. Blaisdell.

The goal of the current research work is to develop a stand-alone jet noise prediction methodology. The current project is focused on jets with internal forced mixers, which are used in regional jet aircraft. In the current approach a two-step method is adopted. First, the turbulence properties in the jet plume are determined from Computational Fluid Dynamics (CFD) analysis using the Reynolds Averaged Navier-Stokes (RANS) equations with a two-equation turbulence model. Second, the far-field noise spectrum is predicted using a noise model based on the combination of simple single stream jet components taken from an existing experimental database. The results of this study show that the CFD predictions of the mean velocity field in the jet plume are in good agreement with experimental particle image velocimetry data. It is also observed that the CFD analysis over-predicts the turbulence levels in a simple single jet shear layer. However, it is determined that the CFD analysis under-predicts the enhancement of the shear layer turbulence levels for the forced mixers. Despite this deficiency, it is seen that the trends in the peak turbulence levels for various mixer geometries are correctly predicted by the CFD analysis. In the current study the far-field noise spectra are predicted using a noise model based on the combination of simple single stream jet components. It is found that the CFD-based two-source model noise predictions are under-predicted when compared to experimental acoustic data. This under-prediction appears to result from the under-prediction of the enhanced turbulence levels in the plume of the jets with forced mixers. In addition to the two-source noise model, a new multi-source model is proposed and evaluated. This model, which has a more general form, takes

into account additional mean flow information from the jet plume. As a result, this model should be applicable to a wider range of geometric configurations. The results using this new multi-source model show a slight improvement for the less aggressive mixers. Additional discrepancies seen in the high penetration mixers are believed to be due to the deficiencies in the CFD predicted turbulence levels.

1. Introduction

1.1 Motivation

The noise generated by modern turbofan aircraft engines is an important issue due to current FAA regulations and airport policies. In addition, stricter regulations and penalty fees for noisy aircraft are expected in the future. Despite over fifty years of research, the problem of predicting the jet noise from complex jet configurations remains unsolved. For the case of subsonic jets, this noise is created by the turbulent mixing of the jet stream with the ambient air. For coaxial jets, additional noise may also be generated by the mixing of the primary and secondary flows. Furthermore, complex jet configurations can have additional mixing enhancement devices, such as forced mixers or chevrons. Consequently, to predict the noise from a complex jet configuration, one must overcome two substantial obstacles. First, the properties of the turbulent flow field in the jet plume must be determined accurately, and second a noise model which relates the turbulence properties to the far-field sound must be developed. Currently, there are no industrial design tools for the prediction of the noise characteristics resulting from complex jet flows. As a result, the jet noise levels of modern turbofan jet engine configurations can only be determined by expensive experimental testing after they have been designed and built. The efforts of the current work are focused on jets with internal forced mixers, which are currently used in regional jet aircraft.

1.2 Jet Noise Prediction Methods

Direct numerical simulations (DNS) have recently been used to find the far-field noise of low Reynolds number jets [1, 2]. Using this approach the time history of the

flow field is determined from a numerical simulation which solves the time dependent Navier-Stokes equations and resolves all of the relevant length scales in the turbulent flow. The flow field data is then post-processed using Lighthill's acoustic analogy to determine the far-field sound. The advantage of this approach is that no turbulence models are required in the application of the acoustic analogy, since the time history of the entire unsteady turbulent flow field is known. However, DNS is currently limited to relatively low Reynolds numbers, on the order of 3,000-4,000 for turbulent jets. As a result, at this time this approach is not feasible for the high Reynolds number application of modern jet engines.

A second jet noise prediction approach currently being investigated involves the use of a large eddy simulation (LES). A large eddy simulation also solves the time dependent Navier-Stokes equations; however, a spatial filter is applied to remove the small scales that are not resolved by the grid. Using this method, the large scale motion is calculated directly and a subgrid-scale model is used to account for the effects of the unresolved small scales. The LES solution provides the time history of the unsteady pressure fluctuations on a surface that encloses the noise source mechanisms. These pressure fluctuations are then extended to the far field by the use of Kirchhoff's method or the Ffowcs Williams-Hawkins method to determine the far-field noise characteristics. A comprehensive overview of applications of LES to jet noise prediction is given by Uzun [3]. LES-based approaches to the prediction and understanding of jet noise show much future promise. However, even with the use of the most advanced supercomputers, presently it is not practical to perform LES calculations for Reynolds numbers that are consistent with modern jet engines, which can be on the order of 10 million. This limitation is especially true if the internally mixed flow region is included due to the fine grid resolution that is required near solid wall boundaries. Consequently, it is not feasible at this time to use LES as a design tool for the application at hand.

A third approach that is currently used to make jet noise predictions combines the turbulent flow field from a Reynolds averaged Navier-Stokes (RANS) solution

with the acoustic analogy. The acoustic analogy was first formed by Lighthill [4, 5] through the derivation of an equation to describe aerodynamically generated noise by rearranging the Navier-Stokes equations. In particular, Lighthill derived the acoustic analogy by combining the continuity and momentum equations. He then formed a wave equation on the left hand side and moved all other terms to the right hand side. In this form the wave operator on the left hand side represents the propagation of the sound and the terms on the right hand side are regarded as known source terms that are responsible for the generation of the sound. Further developments have been made to the standard acoustic analogy developed by Lighthill to account for noise sources that are embedded in a mean flow. An acoustic analogy was derived by Lilley [6] in which the governing equation is linearized about a parallel sheared mean flow, which is representative of the mean flow in a jet. An added benefit of this approach is that in addition to the propagation of the sound it also accounts for the refraction of sound waves by the jet's mean flow.

However, both the strength and the weakness of the acoustic analogy theory lies in the simplicity of the model. For the case of a turbulent jet, to appropriately model the sources on the right hand side of the acoustic analogy equations it is necessary to have information regarding the turbulence statistics. In particular, this method requires models for the two-point space-time correlations of the turbulence statics. Measurement of these statistics is difficult at best and has been completed for only a limited number of flow fields. Based on the data that is available, a number of closure models have been developed but none have proven universally acceptable. As a result, this predictive method, which requires a detailed description of the turbulence, is not of sufficient accuracy at this time to use for engine design purposes.

Despite the drawbacks of the acoustic analogy approach, a number of jet noise prediction methods have been developed based on this method. One of the first general applications of the acoustic analogy approach, commonly referred to as MGB, was developed by Mani, Gliebe, and Balsa [7–10]. In their application the mean flow and turbulence properties of an arbitrary jet configuration are estimated using an

extension of Reichardt's method. The MGB methodology was latter extended by Khavaran [11, 12] to use the mean flow and turbulence properties determined from a solution to the Reynolds averaged Navier-Stokes (RANS) equations using a two-equation turbulence model. This updated approach is now commonly referred to as MGBK. Early applications of the MGBK methodology were made by Khavaran and Georgiadis [13] for supersonic elliptic jets and by Hamed *et al.* [14] for a high bypass coplanar coaxial jet. In addition, Barber *et al.* [15] applied the MGBK methodology to axisymmetric multi-stream jets and jets with forced mixers by azimuthally averaging the CFD flow fields. Noise predictions for the axisymmetric geometries were in agreement with experimental data; however, predictions for the forced mixers did not recover the correct trends. More recently, Barber *et al.* [16] investigated MGBK predictions for high speed round jets using the flow fields from the WIND flow solver. Koch *et al.* [17] compared MGBK noise predictions for a coaxial jet using the flow fields from three different RANS codes. Koch *et al.* [18] also evaluated MGBK noise predictions for two isothermal subsonic jets using the flow fields from the WIND flow solver. Koch *et al.* [19] and Engblom *et al.* [20] applied the WIND/MGBK methodology for the case of separate flow jets with chevron mixers. In both studies the peak turbulence levels in the jet plume were under-predicted by the WIND analysis using the SST turbulence model. It was found that although the absolute levels of the predicted spectra were not in agreement, the trends in the noise spectra were predicted correctly. In particular, the chevron mixer results showed a low frequency reduction and a high frequency enhancement compared to a baseline axisymmetric configuration. In addition, Engblom *et al.* [20] found that the ΔdB values for the chevron mixers were in good agreement with experimental noise data.

Recently Khavaran and researches at the NASA Glenn Research Center have been working to refine the MGBK methodology, which has been subsequently renamed JeNo [21]. In particular Khavaran and Bridges [22, 23] have worked to improve the spectral shape of the noise predictions at high frequencies by investigating alternative model functions for the source terms in the acoustic analogy. Additional

studies of various model functions for the acoustic analogy source terms have also been performed by Goldstein and Khavaran [24], Self [25], Morris and Farassat [26], and Woodruff *et al.* [27]. There have been some recent experimental efforts to measure the turbulent statistics that are required for the models of the source terms in acoustic analogy based noise predictions. Harper-Bourne [28] measured the second and fourth order two-point space-time correlations for the axial velocity in low speed air jets using hot-wire anemometry. Bridges and Wernet [29] measured two-point space-time velocity correlations in hot, high speed turbulent jets using particle image velocimetry (PIV).

In addition to the MGBK application of the acoustic analogy, a number of other researchers have developed RANS-based jet noise prediction methodologies. Self and Bassetti [30] and Page *et al.* [31] have applied a noise prediction methodology based on the Lighthill acoustic analogy for the cases of isothermal single stream and coaxial jets, respectively. Furthermore, researchers at the NASA Langley Research Center [32, 33] developed a jet noise prediction code based on the Lighthill acoustic analogy (Jet3D) that uses flow fields from the PAB3D flow solver with a temperature corrected $k - \epsilon$ turbulence model and anisotropic Reynolds stress modeling. In this application a full three-dimensional integration is performed to allow for complex jet configurations that have mixing enhancement devices. An alternative RANS based noise model has been developed by Tam [34]. This approach explicitly models the noise sources based on a modeled space-time correlation function. The sound from these sources is then propagated to the far-field through the use of the linearized Euler equations. The implementation of this method is similar to the acoustic analogy models and in fact it was shown by Morris and Farassat [26] that Tam's model produces the same results as the acoustic analogy if consistent assumptions are made concerning the turbulence statistics.

An important limitation of any RANS based noise model is the fact that good quality RANS solutions are required to obtain accurate noise predictions. As a result, for jets with complex geometries and flow fields, an accurate solution must

first be obtained before running the acoustic solver. For the application of the current study, the jet has a strongly rotating flow field due to presence of streamwise vortices produced by the forced mixers. Consequently, it may be fairly difficult to obtain a reliable solution of the turbulent flow field using traditional two-equation turbulence models. A comprehensive review of past RANS analysis of jet flows, including those with mixing enhancement devices, is presented latter in this chapter.

A fourth approach to the prediction of jet noise relies on the interpolation of an experimental database. The noise from a single stream jet is only dependent on three characteristic parameters, the velocity, temperature, and diameter. As a result, experimental databases are typically used to make noise predictions for these simple configurations. The Society of Automotive Engineers (SAE) has outlined a method for predicting single stream jet noise in the standard ARP876: Gas Turbine Jet Exhaust Noise Prediction [35]. This methodology was developed based on the experimental jet exhaust noise data of full scale engines without mixing devices such as forced mixers, tabs, or chevrons. In this methodology the overall sound pressure level at various far field observer angles is determined based on the jet acoustic Mach number, M_a , defined as,

$$M_a = \frac{V}{a_o}, \quad (1.1)$$

where V is the fully expanded jet velocity and a_o is the speed of sound in the ambient fluid. The fully expanded jet velocity is determined based on the assumption that the flow isentropically expands to the ambient pressure. Next, the far field normalized sound pressure level similarity spectra at each observer angle is interpolated for a given acoustic Mach number and jet total temperature ratio, defined as the jet total temperature normalized by the ambient temperature. These normalized similarity spectra are given as a function of Strouhal number, St , defined as

$$St = \frac{fD}{V}, \quad (1.2)$$

where f is the frequency and D is the jet diameter. The normalized spectra is then scaled using the OASPL values, jet nozzle area, observer radius, and ambient pressure.

A similar approach is used by the Engineering Sciences Data Unit (ESDU) in their single stream jet noise prediction code, ESDU 98019 [36]. The jet noise prediction method used in the ESDU 98019 code uses an experimental database with a test matrix of various jet velocities and temperatures. The database of jet noise spectra are interpolated or extrapolated based on the jet velocity and temperature for each far field angular location and then normalized based on the jet nozzle exit area, jet density, observer distance, and ambient pressure to yield a single jet noise prediction.

Although the aerodynamic process that leads to the generation of sound in a coaxial jet is the same as that of a single stream jet, the aerodynamic structure of a coaxial jet is greatly different. In addition, the coaxial jet structure is dependent on a number of additional variables such as the velocity, temperature, and area ratios between the two streams. Furthermore, the effects of various parameters are not always separable. These additional complexities make it difficult to develop a noise prediction method that is based solely on the interpolation of an experimental database. Even so, there are a few coaxial jet noise prediction methods that are based on interpolating an experimental database. In particular, the SAE standard, AIR1905: Gas Turbine Coaxial Exhaust Flow Noise Prediction [37], and the ESDU program ESDU 01004 [38] provide coaxial jet noise predictions based on the interpolation of an experimental database. However, there are two main limitations to these methods. First, they require the interpolation over a multi-dimensional matrix of experimental data. Second, the predictions are only valid within the bounds of the matrix of jet conditions, thereby limiting the range of jet conditions which can be predicted.

An alternative approach to predicting the noise from a coaxial jet, named the four-source method, has recently been developed by Fisher *et al.* [39–41]. This method is based on the observation that in coaxial jets distinct regions can be iden-

tified which exhibit similarity relationships that are identical to those observed in simple single stream jets. Based on this fact, it is then proposed that the noise of a simple coaxial jet can be described as the combination of four noise producing regions each of whose contribution to the total far field noise levels is the same as that produced by a single stream jet with the appropriate characteristic velocity, temperature, and length scales. This approach allows existing experimental databases of single stream jet noise spectra to be used as a foundation for determining the noise from a coaxial jet.

1.3 Previous RANS Analysis of Jet Flows

In recent years there has been a considerable research effort at the NASA Glenn Research Center in the calculation of jet flows using the WIND code. Many of these studies have supported the ongoing developments of the WIND/MGBK noise prediction methodology. In particular, Koch *et al.* have performed a series of studies using RANS calculations of the flow field from the WIND code along with a MGBK prediction of the far-field noise for round jets [18], coaxial jets [17], and jets with chevrons [19]. In the study of a round jet [18] the WIND analysis with the Chien $k - \epsilon$ turbulence model produced both mean velocity and turbulence kinetic energy fields that were in general agreement with particle image velocimetry (PIV) data. In the coaxial jet study [17] it was found that analysis using the WIND code with the Chien $k - \epsilon$ turbulence model produced longer potential core lengths. In addition, the peak turbulence levels in the upstream part of the plume ($X/D = 1$) were over-predicted; however, the peak turbulence levels further downstream ($X/D > 6$) were under-predicted. In the chevron study [19] the WIND flow solver was used with the shear stress transport (SST) turbulence model. The results from this analysis showed good agreement with PIV data for the distributions of both the mean axial velocity and turbulence kinetic energy. A recent study of unheated and heated jet flow fields with a variety of chevron configurations was also performed by Engblom *et*

al. [20] using the WIND flow solver with the SST turbulence model. The results from this study showed longer potential core lengths for the WIND solutions as compared to experimental PIV data. Reasonable agreement was seen in the peak turbulence levels in the jet plume for the round jet cases. However, the enhancement of the peak turbulence levels in the upstream region of the plume was under-predicted by the WIND analysis. This trend was particularly noted for the most aggressive chevron configurations.

In addition to the WIND/MGBK research effort, researchers at the NASA Glenn Research Center have investigated the application the WIND flow solver to a number of additional nozzle exhaust flow fields. Georgiadis *et al.* [42] compared the performance of three RANS flow solvers (NPARC, WIND, PAB) for a 2-D ejector nozzle and a Mach 1.9 elliptic jet. The mean velocities for both configurations were in general agreement with measured data. However, some discrepancies were seen in the development of the velocity profiles for the calculations of an elliptic jet. Dal-Bello [43] applied the WIND flow solver with the SST turbulence model to the case of unheated and heated supersonic jets using both the frozen and perfect gas chemistry packages in WIND. The results showed good agreement in the predicted potential core lengths. However, the mean velocities and temperatures further downstream were under-predicted. An appraisal of the two-equation turbulence models in WIND was performed by Dembowski *et al.* [44] for heated and unheated Mach 2.0 jets. The results from all of the turbulence models studied were similar to those of DalBello, which showed an over-prediction of the decay rate of the centerline velocity. A recent study by Georgiadis *et al.* [45] has investigated the effects of turbulence models on the calculation of lobed nozzle flow fields. The results of this study showed that the linear two-equations turbulence models predicted a delay in the initial mixing rates and hence longer potential core lengths. However, reasonable agreement with experimental data was seen farther downstream. This study also showed that a nonlinear two-equation explicit algebraic stress model provided the best agreement with the experimental turbulence intensities.

Franko *et al.* [46] performed a study of high speed coaxial jets using the WIND code with the SST turbulence model. The test cases all had a heated Mach 1.5 primary flow and a parametric array of various subsonic secondary flow speeds and nozzle areas. The results of this study suggest that grid points should be packed near the nozzle exit and near the centerline to accurately resolve the plume flow field. It was also found that for heated jet flows the effects of varying the turbulent Prandtl number are Mach number dependent. Georgiadis *et al.* [47] also performed calculations of coaxial jets flows using the WIND code with the SST turbulence model. In this study both standard coaxial and eccentric configurations were evaluated. Both cases used a heated Mach 1.5 primary stream and a subsonic secondary stream. The WIND results were able to reproduce the experimental trend of a reduced potential core length for the eccentric nozzle configuration. However, both the standard coaxial and eccentric configurations produced longer potential core lengths compared to the experimental data. In addition, for the eccentric nozzle case at axial locations far downstream ($X/D = 20$) the experimental velocity profiles show a noticeable asymmetry; however, the WIND results at this location are completely mixed and have a symmetric profile. DalBallo *et al.* [48] studied axisymmetric circular-arc boattail nozzles at off design transonic Mach numbers using the WIND code. In this study it was noted that for flow fields with separation the steady-state (variable time-stepping) mode often does not produce a converged solution. As a result the time accurate (constant time-stepping) mode is required to obtain a converged flow field. It was observed that the SST turbulence model demonstrated the best agreement with external afterbody and internal nozzle pressure distributions.

Early investigations of nozzle flows were also made using the NPARC code, the predecessor to WIND. Debonis *et al.* [49] validated the NPARC code for nozzle afterbody flows at transonic speeds. Georgiadis *et al.* [50] studied the performance of the NPARC code on a number of nozzle exhaust flow fields. Furthermore, Georgiadis *et al.* [51] provided grid resolution and boundary condition recommendations for NPARC calculations. Kahavaran and Georgiadis [13] also studied an early applica-

tion of the MGBK methodology to supersonic elliptic jets using the flow fields from the NPARC code with the Chien $k - \epsilon$ turbulence model. A Mach 2.0 supersonic jet test case was evaluated by Barber *et al.* [52] with the NPARC code.

There are a few researchers who have previously investigated forced mixer flows using RANS CFD. Barber *et al.* [15] performed RANS simulations of jets with forced mixers and applied the MGBK noise prediction code to the azimuthally averaged flow fields. However, the RANS flow fields were not compared to experimental data. The use of structured versus unstructured grids and the application of turbulence models with a non-linear Boussinesq approximation were studied by Salman [53, 54] for jet flows with forced mixers.

Arguably one of the weakest links in current RANS flow simulations lies in the turbulence model. A number of research efforts have been made to not only assess the capabilities of current turbulence models for jet flow fields, but to also improve their performance through the applications of corrections and modifications. Bardina *et al.* [55] evaluated the performance of the standard $k - \epsilon$, the Wilcox $k - \omega$, the Menter SST, and the Spalart-Allmaras turbulence for a variety of free shear flows, including a round jet. In this study the mean velocity profiles and jet spreading rates were compared to experimental data. It was found the that the $k - \epsilon$ and SST turbulence models produced the best agreement with the experimental data. Woodruff *et al.* [56] evaluated the performance of a $k - \epsilon$ and an algebraic stress two-equation turbulence model for a Mach 2.0 single stream jet. Their results, which compared the centerline mean velocities and temperatures, showed that variations between various flow solvers were greater than those between various turbulence models. Their results also showed the general trend of RANS simulations of supersonic jets in over-predicting the decay rate of the centerline velocities downstream of the potential core. Mani *et al.* [57] studied the performance of the Baldwin-Barth, Spalart-Allmaras and the SST turbulence models for internal and external flows using the NASTD code. In this study a heated and unheated Mach 2.0 axisymmetric jet and an eight lobed mixer/ejector configuration were tested. The results from this study showed that

the SST turbulence model performed the best of the three models tested. Lebedev *et al.* [58] studied the performance of the Spalart-Allmaras and several variations of a $k - \epsilon$ turbulence model for conical and chevron nozzle flows. It was found that the chevron nozzle flow showed less sensitivity to the choice of turbulence model for the prediction of the mean velocities. In addition, it was found that the Pope vortex stretching correction [59] led to large reductions in the mixing of chevron nozzle flows and resulted in poor agreement with experimental data of the centerline velocities. Birch *et al.* [60] applied a new zonal $k - \epsilon$ turbulence model to coaxial and chevron nozzle flows. In this model one set of model coefficients is used in the near field of the jet plume (upstream of the potential core) and a second set of model coefficients is used in the far field of the jet plume (downstream of the potential core). Results using this zonal model showed good agreement in the turbulence intensities in the upstream region ($X/D = 2$). However, the turbulence levels further downstream ($X/D = 12$) were greatly under-predicted. Birch *et al.* [61] latter compared far-field noise predictions of a single stream and chevron nozzle using flow fields calculated with both the standard and zonal $k - \epsilon$ turbulence models. These noise predictions, which were made using a form of the acoustic analogy, show negligible differences at the spectral peak for the single stream jet case. However, a difference of more than 4dB was seen in the spectral peak for the chevron nozzle case.

A number of researchers have investigated modifications to the standard $k - \epsilon$ turbulence model to improve the performance for jet flow fields. Thies *et al.* [62] and Tam *et al.* [63] have re-calibrated the model constants of a $k - \epsilon$ turbulence model to yield better agreement in the mean velocities for round jet and heated jet flows, respectively. However their re-calibration process only considered the mean velocities and recent studies [64] have shown that their models considerably under-predict the turbulence intensities in the jet plumes of single stream jets. Abdol-Hamid *et al.* [65] implemented corrections to the standard $k - \epsilon$ turbulence model to improve the performance for subsonic and supersonic heated jets. Engblom *et al.* [66] investigated a variable diffusion turbulence model correction for round jets.

In this model a correction is applied to the Chien $k - \epsilon$ turbulence model to locally increase the turbulent diffusion near the end of the potential core. Results using this new modification were compared to experimental PIV data and show considerable improvements in both the mean velocity and turbulence kinetic energy fields in the entire jet plume. Georgiadis *et al.* [64] recently evaluated the performance of a number of modified two-equation turbulence models for jet flow predictions. In their study the flow fields were calculated using the WIND flow solver and compared to experimental PIV data. As a result, their analysis provides the most comprehensive comparison of jet plume mean velocities and turbulence intensities to date. In this study both unheated and heated subsonic single stream jets were evaluated using the SST and several variations of the standard $k - \epsilon$ turbulence model, including models by Thies *et al.* [62], Tam *et al.* [63], Abdol-Hamid *et al.* [65], and Engblom *et al.* [66]. Their results show that many new turbulence model modifications that improve the mean velocities of jets adversely affect the turbulence kinetic energy. Of all the models tested the variable-diffusion model [66] showed the best agreement with both the mean velocity and turbulence kinetic energy profiles.

Over the past 5 years researchers at Combustion Research and Flow Technology, Inc. (CRAFT Tech) have investigated turbulence models for jet applications . Kenzakowski *et al.* [67] evaluated the performance of the standard $k - \epsilon$ turbulence model for a coaxial jet and jets with chevrons and tabs. Comparisons of the total pressure and total temperature at various planes in the jet plume of the calculated flow fields showed good agreement with experimental data. Kenzakowski *et al.* [68] studied the application of a number of turbulence models including an explicit algebraic stress turbulence model (EASM) and the Speziale and Gatski anisotropic dissipation rate turbulence model (ADRM) for low and high speed shear layers and round and planar jets. In addition, they investigated the use of variable Prandtl and Schmidt numbers. Their results for the round jet test case showed that the $k - \epsilon$ model with the Pope vortex stretching correction [59] and the ADRM model with the Pope vortex stretching correction produced the best agreement with Reynolds

stress profiles in the plume. Kenzakowski *et al.* [69] and Papp *et al.* [70] re-calibrated the coefficients of the EASM turbulence model to improve the predictions for jet flow fields. In their study they compared the performance of the standard $k - \epsilon$ model, the standard EASM model, and the re-calibrated EASM model (EASM/J) for a low speed mixing layer, a low speed cold planar jet, a low speed cold round jet, a high speed mixing layer, a Mach 2.2 cold round jet, a Mach 2.2 hot round jet, a subsonic cold round jet, and a coaxial jet. For all of the test cases profiles of mean velocity and Reynolds stresses are compared to experimental data. For the coaxial jet test case the predictions are compared to experimental PIV data. Kenzakowski *et al.* [71] applied the EASM/J turbulence model to jets with corrugated nozzles. In addition, they studied the impact of a number of $k - \epsilon$ model corrections on the developing region of a round jet. In this study the predictions were compared to experimental PIV data for both cold and hot round jets. Kenzakowski *et al.* [72] also evaluated the impact of a number of corrections to the $k - \epsilon$ model on the developing region of a round jet. The flow field predictions in this study were also compared to experimental PIV data. Results from this investigation suggest that use of the Pope vortex stretching correction should be delayed until downstream of the potential core. Kenzakowski *et al.* [73] have continued work to improve the prediction of turbulence anisotropy in round jets using the EASM/J turbulence model. Brinckman *et al.* [74] have also investigated modifications to the $k - \epsilon$ model to allow variable Prandtl and Schmidt numbers based on scalar fluctuation models. Kenzakowski *et al.* [75] recently applied the EASM/J turbulence model to a range of subsonic unheated and heated jets with varying chevron configurations. Comparisons of the mean centerline velocities showed good agreement for the cold cases. However, for the heated cases the potential core length was over-predicted by 1-2 diameters.

Based on the preceding literature review it is observed that there is a limited amount of published work on the CFD analysis of jet flow fields with lobed mixers. However, based on the available literature for these configurations, and the closely related configuration of chevrons, it appears that the SST turbulence model generally

provides some of the highest quality flow fields when compared to other traditional turbulence models.

The initial RANS CFD work of the mixers evaluated in this study was performed by the Rolls-Royce Corporation. This initial CFD work supplemented an earlier set of mixer tests in the NASA Glenn Research Center [76–82]. Additional CFD analysis was performed to aid in the design of a new mixer geometry and to help design the 2003 NASA Glenn experimental test program. This initial CFD work was performed using the ADPAC flow solver using the one-equation Spalart-Allmaras turbulence model.

Additional CFD work on the present set of mixer geometries using the ADAPAC code began at Purdue University in the Fall of 2001. In the following Spring, the Purdue CFD effort continued with a more extensive study of a selection of the present forced mixers using the WIND flow solver [83–85]. This CFD analysis was focused on the set points with a Mach 0.2 flight stream and covered only the 12-lobe mixer geometries.

1.4 Objectives of the Present Research

The primary goal of this research is to develop a noise prediction methodology for jets with internal forced mixers that is both independent of experimental testing of new designs and computationally feasible as part of a design process. In the current approach a two-step method is adopted. First, the turbulence properties in the jet plume are determined from Computational Fluid Dynamics (CFD) analysis using the Reynolds Averaged Navier-Stokes (RANS) equations with a two-equation turbulence model. Second, the far-field noise spectrum is predicted using noise models that are based on the combination of simple single stream jet components taken from an existing experimental database. The specific objectives of the research are as follows:

1. Assess the ability of CFD using the RANS equations with a two-equation turbulence model to accurately predict the turbulence kinetic energy in the

plume of both simple and complex jet configurations including axisymmetric coaxial jets and jets with internal forced mixers. In this study the RANS flow fields are compared to experimental PIV data of the jet plumes.

2. Calculate the source strength parameters in a two-source noise model from the turbulence properties in a RANS flow field and compare the resulting noise predictions to experimental far field acoustic data.
3. Propose and validate a new multi-source noise model for more robust noise predictions of jets with mixing enhancement devices. Using this new methodology both mean flow and turbulence properties from a RANS flow field are used as inputs to the noise model. Noise predictions are compared to experimental far field acoustic data.
4. Investigate additional noise sources in the forced mixer jet noise spectra, such as the High Mach number Lift (HML) phenomenon, using RANS CFD analysis.

This thesis is organized as follows. The details of the RANS CFD analysis are given in Chapter 2. In this chapter a discussion of the grid and turbulence model sensitivity is discussed for the axisymmetric confluent mixer geometry. In addition, the confluent mixer RANS flow fields are compared to experimental PIV data for set points 312 and 5000. Furthermore, a discussion of the azimuthal resolution of the lobed mixer grids is also provided. Finally, the lobed mixer RANS flow fields are compared to the experimental PIV data for set point 312. In Chapter 3 the two-source noise model formulation is presented. The calculation of the noise model source strength parameters is discussed and the resulting noise predictions are compared to the experimental far field acoustic data. In Chapter 4 the multi-source noise model formulation is presented. The process for extracting the noise model input parameters from a RANS flow field is described. Furthermore, multi-source model noise predictions are compared to the experimental far field acoustic data. In chapter 5 the high Mach number lift (HML) noise source is investigated using RANS

CFD. In particular, the source strength of the noise generated by the interaction of the turbulent streamwise voriticies and a normal shock is estimated using a RANS solution. The CFD-based estimates of these noise levels are compared to experimental acoustic data. Finally, concluding remarks and future recommendations are given in Chapter 6.

Parts of this work were published as conference papers listed as References [99, 100]. In addition, portions of this work were reported in project Final Reports submitted to the Aeroacoustics Research Consortium, which are listed as References [101, 102].

2. RANS CFD Analysis

2.1 Objectives

The primary objective of the current project is the development of a stand-alone noise prediction methodology for jets with forced mixers. Since the far-field noise characteristics of a particular jet configuration are strongly dependent on the aerodynamic properties of the jet plume, it is critical to have detailed information of the mean flow and turbulence properties in the jet plume for a particular configuration. In the current project this information is efficiently obtained using Computational Fluid Dynamics (CFD) analysis with the Reynolds averaged Navier-Stokes (RANS) equations along with a two-equation turbulence model. The CFD predictions of the jet flow fields are compared to experimental PIV data. In this chapter details of the experimental program are described, followed by a summary of the CFD analysis of the axisymmetric confluent mixer and the forced mixer geometries.

2.2 Lobed Mixer Experimental Data

The experimental acoustic and aerodynamic data for the mixers used in this study was taken in the Aeroacoustic Propulsion Laboratory (AAPL) at the NASA Glenn Research Center during the spring of 2003 [103]. The Aeroacoustic Propulsion Laboratory, shown in Figure 2.1, is an anechoic geodesic dome, which is 130 feet in diameter and 65 feet high. This facility houses the Nozzle Acoustic Test Rig (NATR), which is a 53 inch diameter free-jet acoustic wind tunnel. This rig is capable of producing jet flows in simulated flight conditions up to Mach 0.30. The NATR rig is fed by the High Flow Jet Exit Rig (HFJER). This rig can provide nozzle flow conditions up to 1425°F (1050 K) with a nozzle pressure ratio (*NPR*) of 4.5. In

addition, it has the capability to provide dual flow configurations with independent primary and secondary flow temperature and pressure ratios. The AAPL facility has two far field microphone arrays located at approximately 50 feet from the nozzle exit of the Nozzle Acoustic Test Rig.

Mixer and Nozzle Geometries

A number of mixer and nozzle geometries are evaluated in the current study. A sample mixer-nozzle configuration is shown in Figure 2.2. The geometries of all six mixers that are evaluated in this study are shown in Figure 2.3. These geometries are the baseline axisymmetric confluent mixer (CFM), the 12-lobe low penetration mixer (12CL), the 12-lobe medium penetration mixer (12UM), the 12-lobe high penetration mixer (12UH), the 20-lobe high penetration mixer (20UH), and the 20-lobe high penetration scalloped mixer (20DH). The forced mixer geometries, which are essentially convoluted splitter plates, are parameterized by three properties, the number of lobes, the lobe penetration height and the amount of scalloping. The lobe penetration height is defined as the difference between the maximum and minimum radii at the end of the splitter plate, as shown in Figure 2.4. The amount of scalloping is defined by the depth of the cut-outs in the sidewalls of the lobes. The properties of the five forced mixer geometries evaluated in this study are given in Table 2.1. In addition to the six mixer geometries, three nozzle geometries that have varying lengths are also evaluated. The wall contours of these nozzles are shown in Figure 2.5 and their corresponding geometric properties are given in Table 2.2.

During the experimental tests at the AAPL facility the aerodynamic properties of the primary flow, secondary flow and simulated flight streams were recorded for each run. These properties include the primary and secondary flow total temperatures, total pressures, and mass flow rates. In addition, measurements of the ambient pressure, temperature and relative humidity were taken during each run. Seven of the set points in the experimental test program will be utilized in this study. The

flight stream Mach numbers (M_f), nozzle total pressure ratios (NPR) and nozzle total temperature ratios (NTR) of these operating set points are shown in Table 2.3. In addition, the corresponding nominal ideal primary, secondary, and fully mixed jet properties are shown in Table 2.4.

Acoustic Data

All of the experimental jet noise data used in this study was taken in the acoustic far field at a radius of approximately 80 jet diameters. The acoustic data is supplied in the form of 1/3 octave Sound Pressure Level (SPL) spectra. These SPL spectra cover a frequency range of 158.5 Hz to 79432.8 Hz (1/3 octave bands 22 to 49), at angles from 55° to 165° in 5° increments, as referenced from the intake axis. The experimental tests were run with a one-quarter scale model, consequently, acoustic data was recorded for frequencies up to 80 kHz, which corresponds to a full scale upper frequency limit of 20 kHz, the upper limit of normal human hearing. The acoustic data is supplied in three main formats. The first format (as measured) contains SPL data that is corrected for microphone response. The second format (standard day, polar arc) contains SPL data that is corrected for microphone response, normalized to a 50 ft arc, and referenced to an acoustic standard day ($T_o = 298.3$ K, $p_o = 98.595$ kPa, 70% relative humidity). The third format (one-foot lossless) contains SPL data that is corrected for microphone response, normalized to a 1 foot distance, and corrected to remove all atmospheric absorption. In the current research effort noise predictions are compared to the experimental data in the one-foot lossless format.

Particle Image Velocimetry Data

Particle Image Velocimetry (PIV) data was taken for the six mixers with the baseline L0 nozzle at set point 312. Additional PIV data was also taken for the confluent mixer at set point 5000, and for the 12CL mixer at set points 112 and 310.

The PIV data was acquired using a dual camera stereoscopic PIV apparatus arranged to record data in planes perpendicular to the jet axis [103]. Using this procedure, all three components of the mean and RMS velocities were measured. For each data point, twelve planes of PIV data were acquired downstream of the final nozzle exit at X/D locations of 0.1, 0.2, 0.3, 0.5, 0.7, 1.0, 1.4, 2.0, 3.0, 5.0, 7.0, and 10.0. The PIV data planes were centered to capture approximately one quadrant of the jet cross-section and supplied on a Cartesian grid (137×103). This data was later interpolated onto a polar grid (100×97) with uniform radial and azimuthal spacing. The PIV data was then re-centered to align the jet centerline with the origin of the PIV data reference frame to aid in further data post-processing and for comparison to the CFD results. Additional details of the PIV data post-processing procedure is given in Appendix A.

Table 2.1 Mixer properties

Mixer ID	Number of Lobes	H [in]	L_s [in]	Description
CFM	0	0.00	0.00	Confluent (Axisymmetric)
12CL	12	1.44	0.00	12 Lobe, Low Penetration
12UM	12	1.80	0.00	12 Lobe, Intermediate Penetration
12UH	12	2.07	0.00	12 Lobe, High Penetration
20UH	20	2.03	0.00	20 Lobe, High Penetration
20DH	20	2.03	1.15	20 Lobe, High Penetration, Scalloped

Table 2.2 Nozzle properties

Nozzle ID	Length [in]	Diameter [in]	Description
L0	14.25	7.25	Baseline
L1	11.64	7.25	75% Baseline
L2	8.89	7.25	50% Baseline

Table 2.3 Nominal set point operating conditions

Set Point	M_f	NPR_p	NPR_s	NTR_p	NTR_s
110	0.00	1.39	1.44	2.80	1.20
112	0.20	1.39	1.44	2.80	1.20
210	0.00	1.54	1.61	3.13	1.20
212	0.20	1.54	1.61	3.13	1.20
310	0.00	1.74	1.82	3.34	1.20
312	0.20	1.74	1.82	3.34	1.20
5000	0.00	1.44	1.44	1.01	1.01

Table 2.4 Nominal set point characteristic jet properties

Jet Property	Units	110	210	310	5000
λ	[]	0.69	0.65	0.62	1.00
δ	[]	2.38	2.65	2.83	1.00
β	[]	3.11	2.90	2.90	2.90
V_p	[m/s]	382.1	460.1	533.6	239.3
T_p	[K]	739.2	806.9	832.8	259.6
D_p	[m]	0.0909	0.0899	0.0902	0.0968
V_p/a_o	[]	1.12	1.35	1.57	0.70
T_p/T_o	[]	2.57	2.80	2.89	0.90
V_s	[m/s]	261.7	296.8	330.0	239.3
T_s	[K]	310.6	300.8	290.4	259.6
D_s	[m]	0.1842	0.1842	0.1842	0.1842
V_s/a_o	[]	0.77	0.87	0.97	0.70
T_s/T_o	[]	1.08	1.04	1.01	0.90
V_m	[m/s]	281.6	321.8	360.7	239.3
T_m	[K]	381.2	378.2	372.4	259.6
D_m	[m]	0.1872	0.1881	0.1887	0.1841
V_m/a_o	[]	0.83	0.95	1.06	0.70
T_m/T_o	[]	1.32	1.31	1.29	0.90



Figure 2.1. Aeroacoustic Propulsion Laboratory facility at the NASA Glenn Research Center.

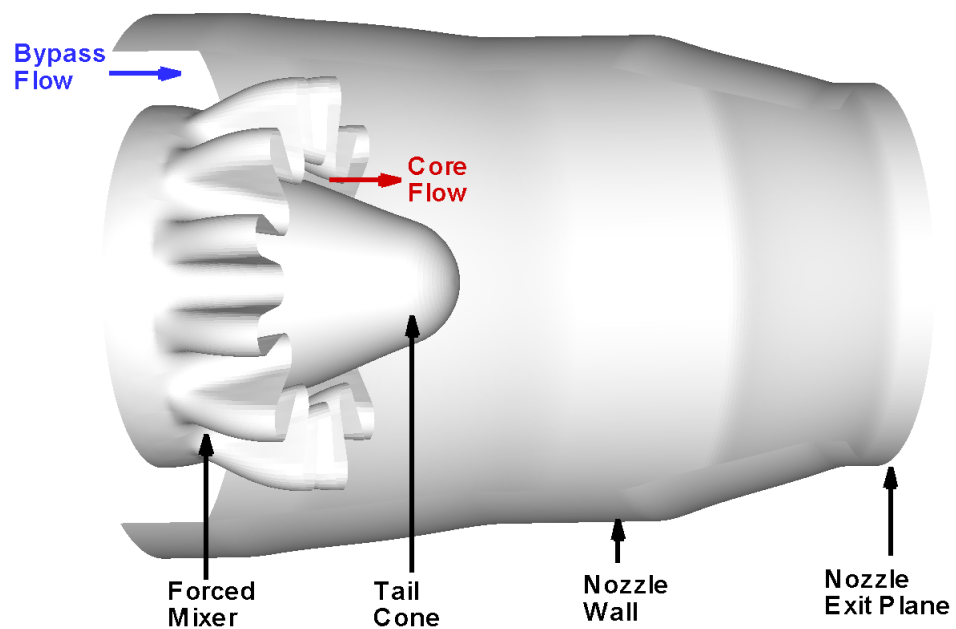


Figure 2.2. Sample configuration of an internal forced mixer and nozzle.

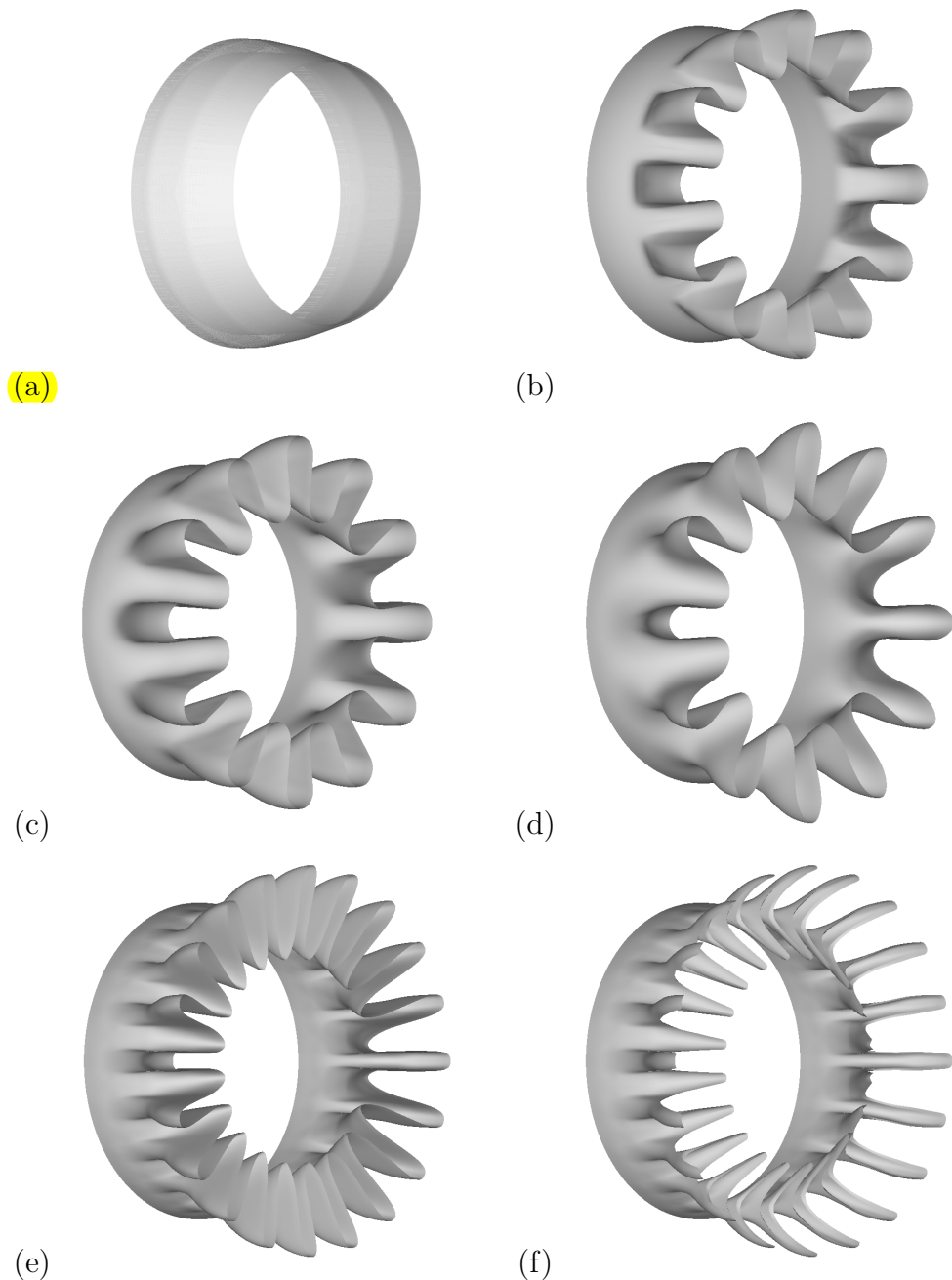


Figure 2.3. Mixer geometries: (a) confluent mixer, (b) 12CL, (c) 12UM, (d) 12UH, (e) 20UH, (f) 20DH.

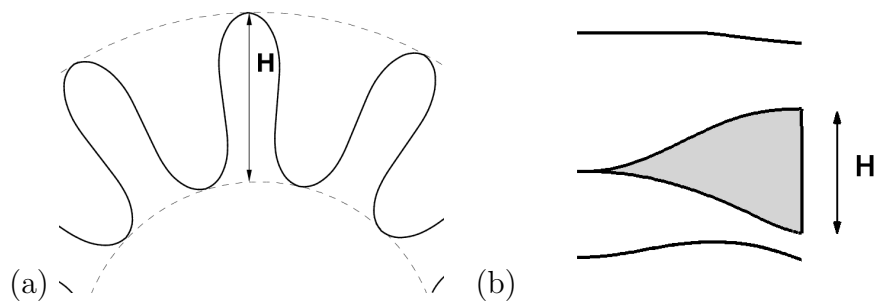


Figure 2.4. Definition of the forced mixer penetration height: (a) lobed mixer trailing edge profile and (b) lobed mixer side view.

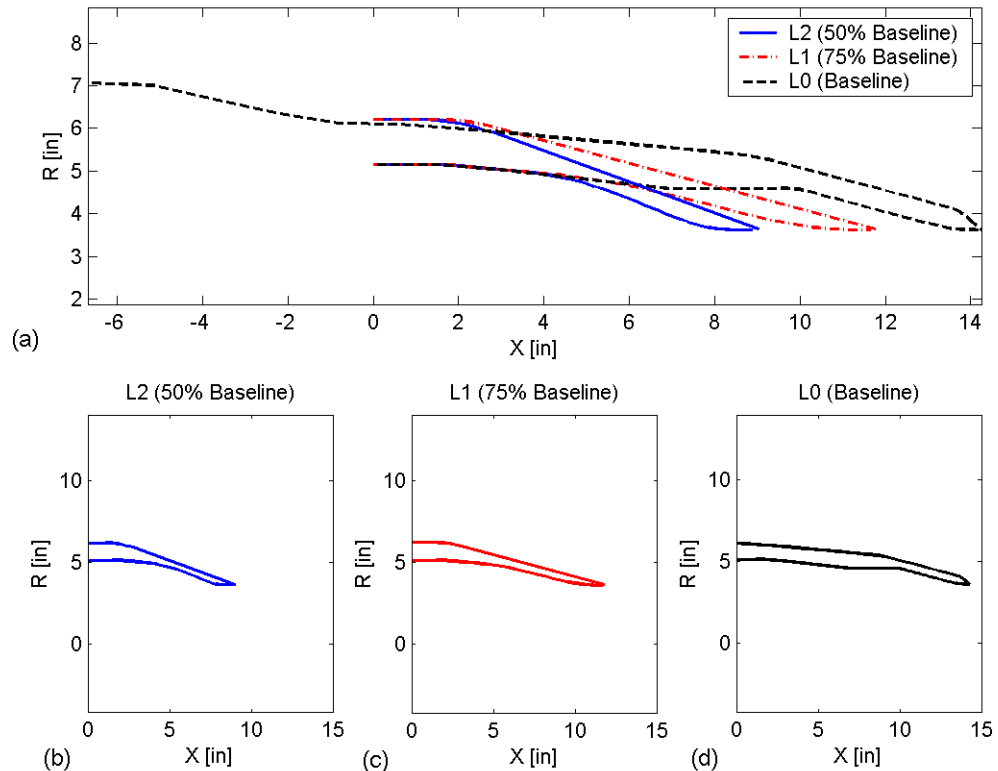


Figure 2.5. Nozzle geometry profiles: (a) L0, L1, and L2 nozzles (b) L2 nozzle (c) L1 nozzle and (d) L0 (baseline) nozzle.

2.3 Computational Details

The RANS calculations in this study are performed using the WIND flow solver [104, 105]. The WIND code is the production flow solver of the NPARC Alliance, which is a partnership between the NASA Glenn Research Center, the Arnold Engineering Development Center, and Boeing. **WIND (Version 5) is a structured, multi-zone, compressible flow solver with flexible chemistry and turbulence models.** WIND allows for either abutting or overlapping zonal interfaces providing the flexibility to treat complex geometries. A recently released version of WIND (WIND-US) also has the capability to use unstructured grids. The WIND code can run in parallel using a master-worker implementation. It has the capability to use either PVM or MPI for parallel communication. WIND uses a node-centered finite-volume formulation. The default numerical method uses a full block implicit operator and a Roe second-order, upwind-biased, explicit operator modified for stretched grids. For structured grid applications additional schemes and differencing orders are available for the explicit operator.

In addition to the Spalart-Allmaras one-equation turbulence model [106], three different two-equation turbulence models are available in WIND. These models are the Menter Shear-Stress Transport (SST) model [107], the Chein low Reynolds number $k - \epsilon$ model [108], and the Rumsey-Gatski low Reynolds number algebraic stress model [109–111]. The Rumsey-Gatski model is only available with WIND-US, the most recent version of WIND.

In this study all of the WIND calculations were performed on a 102-processor Linux cluster. **The axisymmetric confluent geometries were typically run using 1 processor and the 3-D lobed mixer cases were typically run using 10 processors.**

A schematic of the boundary conditions that are applied to each region of the computational grid is shown in Figure 2.6. **Viscous wall boundary conditions** are used on all solid wall surfaces. WIND’s Arbitrary Inflow boundary condition is used for the core and bypass stream inlets. **Freestream boundary conditions** are used on the outer

boundaries to represent the simulated flight stream. **Outflow boundary conditions** are applied to the downstream boundary. **Inviscid wall boundary conditions are used on the centerline.** For the 3-D lobed mixer cases the natural symmetry and periodicity of the geometry is exploited and only one half of a lobe is modeled computationally. As a result, reflection boundary conditions are applied to the symmetry planes for these cases.

At the core and bypass stream inflow boundaries the total pressures and total temperatures are specified. **These values are calculated based on the nozzle pressure ratio (NPR) and nozzle temperature ratio (NTR) for a given set point along with the ambient pressure and temperature.** For the freestream boundaries the inflow Mach number is specified. **A freestream Mach number of 0.05 is used for the static set points to aid in solution convergence.** In the experimental test program a freestream Mach number of 0.05 was also used for static set points during the acquisition of the PIV data.

When the SST turbulence model is selected WIND allows the user to specify the turbulence kinetic energy (k) and specific turbulence dissipation rate (ω) at the inflow and freestream boundaries. For all of the WIND cases that were run with the SST turbulence model these values were specified using the following assumptions: (1) **the core and bypass streams had an inflow turbulence intensity of 2%,** (2) the freestream had an inflow turbulence intensity of 5%, (3) all inflow streams had a turbulence viscosity ratio of 100. The first two assumptions were based on the background turbulence levels in the first plane of PIV data for the confluent mixer configuration. The third assumption was based on a small study of the inflow boundary conditions, which found that for inflow turbulence viscosity ratios of less than 100 the inflow turbulence levels would substantially decay between the inflow plane and the nozzle exit plane. The previously listed inflow turbulence assumptions result in a inflow turbulence length scale that is approximately 2% of the local duct height for the core and bypass flows.

In all of the calculations performed in this study wall functions were enabled. The WIND code is setup such that if wall functions are enabled, then they are only applied if the first grid point adjacent to the boundary is within the y_2^+ range of 15 to 100. If the y_2^+ value is less than 15 then WIND reverts back to a standard no-slip condition for viscous walls.

All pre- and post-processing is performed with grid and solution files in plot3d format. The computational meshes are generated using a combination of specially designed Matlab scripts and commercial grid generation software (Gridgen). The grid files are generated/exported in plot3d format and are then converted to the WIND common file format using the WIND utility *cfcnvt*. The boundary conditions are then applied using *gman*, a WIND pre-processor. Typically this process is semi-automated through the use of a *gman* journal script. If necessary, zones in the grid file are then split using the WIND utility *cfsplit*. After the completion of a run the solution file is converted to plot3d format using *cfpost*, the WIND post-processor. The plot3d format solution and grid files are then viewed in Tecplot or post-processed further with specially developed Fortran codes to extract specific data from the solution. In addition, the residual and integrated mass flow rate data is extracted from the WIND output file using the WIND utility *resplt*.

In all of the WIND calculations performed in this study the steady-state time stepping mode is used. This mode uses a constant CFL number, local time stepping method. Solution convergence is confirmed in a number of ways. First, the residual history is reviewed. Typically solution convergence begins to stall after the residuals drop by approximately 3 orders of magnitude. Second, the integrated mass flow rate histories are reviewed. The bulk mean flow values are typically converged once these quantities converge to a steady state value. Finally, the turbulence intensities along the lip-line in the jet plume are compared between sets of iterations. This technique has often been used by previous researchers at NASA Glenn who have calculated jet flow fields using the WIND flow solver.

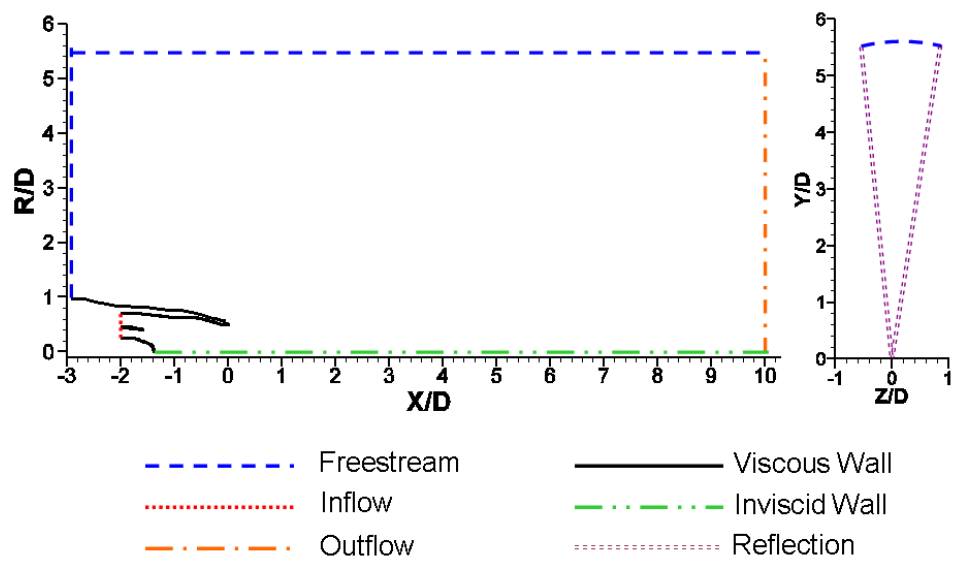


Figure 2.6. Schematic of the boundary conditions.

2.4 Confluent Mixer Analysis

A schematic of the confluent mixer configuration with baseline L0 nozzle is shown in Figure 2.7. This configuration consists of a simple axisymmetric splitter plate which separates the core and bypass flows inside of a convergent nozzle.

2.4.1 Grid Sensitivity

The standard grid (G1) for the confluent mixer configuration contains 65,750 grid points, which are divided into 6 zones. The zone layout for the confluent mixer grid is shown in Figure 2.8 and the grid point distribution for each zone is given in Table 2.5. The confluent mixer grid extends 5.5 diameters in the radial direction and 25 diameters in the axial direction. The wall normal grid spacings were set as 0.00005 D (3.625E-4 inches) at all viscous wall boundaries. In addition the axial spacing at the nozzle exit was set as 0.001 D (7.25E-3 inches). In the interior region of the zones the grid lines were packed near the primary-secondary shear layer and the main jet shear layer. Additional details of the procedures used to generate the confluent mixer grid are given in Appendix B. An example of the computational grid near the nozzle interior region of the confluent mixer configuration is shown in Figure 2.9.

Table 2.5 Grid point distribution for the standard confluent mixer grid (G1)

Zone	Axial Dimension	Radial Dimension
1	37	65
2	37	65
3	25	129
4	81	129
5	41	89
6	201	217

The grid stretching ratios in some parts of the nozzle interior region of the standard (G1) confluent mixer grid exceed values of 1.2, which is a general guideline for maximum grid stretching ratios. In light of this fact, a second grid (G2) was constructed which uses 81 points in the radial direction for zones 1 and 2. All other properties of the G2 grid are the same as the standard G1 grid. Consequently, the maximum stretching ratios in the G2 grid are all below a value of 1.2. A third grid (G3) was generated for the confluent mixer by doubling the amount of grid points in the G1 grid in both the axial and radial directions. As a result, the wall spacing values in the G3 grid are half that of those in the G1 grid.

The variation of y_2^+ along the nozzle interior wall for the G1, G2, and G3 confluent mixer grids at set point 312 is shown in Figure 2.10. In this figure it is seen that the values of y_2^+ vary between 15 and 35 for the G1 and G2 grids. As a result, for the G1 and G2 grids WIND uses wall functions at the viscous wall boundaries. However, for the G3 grid the y_2^+ values vary from 5 to 15. Consequently WIND disables the wall functions at the viscous wall boundaries for the refined G3 grid. The boundary layer profiles at the nozzle exit plane are shown for the three confluent mixer grids in Figure 2.11. In this figure it is seen that the boundary layer profiles are almost identical for the three grids.

The centerline velocity profiles for the three confluent mixer grids are shown in Figure 2.12. Here it is again seen that the results from the three grids are almost identical, with the refined G3 grid showing a slightly longer potential core length. However, it is noted that the all three confluent mixer solutions considerably over-predict the potential core length. Profiles of the mean streamwise velocity (V/V_m) of the three confluent mixer solutions are shown in Figure 2.13 for six axial locations in the jet plume. The profiles in this figure show that all three solutions are virtually identical, with only a slight variation present near the centerline in the $X/D = 10$ plane. Overall, in Figure 2.13 it is seen that there is good agreement in the mean velocities between the WIND results and the experimental PIV data. The major difference between the computations and the experimental data is the

discrepancy in the primary flow potential core length. This discrepancy appears to be due to an under-prediction of the mixing in the initial shear layer in the WIND computations. The corresponding comparison of the turbulence intensity ($k^{1/2}/V_m$) profiles are shown in Figure 2.14. It is again observed that the results from the three confluent mixer grids are virtually identical. Some differences are seen near the centerline in the turbulence shed by the separation at the end of the tailcone. It is seen, however, that these differences do not impact the turbulence intensities in the shear layers, which appear to be dictated entirely by the mean flow gradients. At this point it is important to note that for this coaxial jet configuration the WIND calculations are all over-predicting the turbulence intensities in the plume.

2.4.2 Turbulence Model Sensitivity

The sensitivity of the plume mean velocities and turbulence intensities to the choice of turbulence model was evaluated for the confluent mixer configuration at set point 312. Calculations were performed using the WIND code with the one-equation Spalart-Allmaras turbulence model and the two-equation Chien $k - \epsilon$ and Menter SST turbulence models. Due to the relatively limited number of turbulence models available in the WIND code, analysis with the FLUENT code was also performed. In particular, the Menter SST, Wilcox $k - \omega$, standard $k - \epsilon$, realizable $k - \epsilon$, RNG $k - \epsilon$, Spalart-Allmaras, and Reynolds Stress turbulence models were all evaluated using the FLUENT code. The FLUENT solutions were obtained by running 4000 iterations using the coupled solver (implicit) with first order accuracy. The solutions were then restarted with the segregated solver using second order accuracy and run for an additional 3000 iterations. The FLUENT runs were performed using the steady state, axisymmetric mode. In addition, the ideal gas law was enabled.

The turbulence kinetic energy (k) in both the WIND and FLUENT solutions with the one-equation Spalart-Allmaras turbulence model was approximated as

$$k = \frac{\nu_t \sqrt{2S_{ij}S_{ij}}}{2a_1}, \quad (2.1)$$

where ν_t is the kinematic eddy viscosity, S_{ij} is the mean strain rate tensor, and a_1 is a normalizing constant equal to 0.155. This approximation to the turbulence kinetic energy has been used by previous researchers in the evaluation of the Spalart-Allmaras turbulence model for jet flow applications [45].

The centerline velocity profiles for the turbulence model study runs are compared to the experimental PIV data in Figure 2.15. In this figure it is seen that the performance of most turbulence models is very similar with slight variations occurring in the predicted potential core lengths. Notable exceptions to the general trend are seen with the FLUENT $k - \omega$ model and the WIND Chien $k - \epsilon$ model, which appear to under-predict the mixing in the initial shear layer and asymptotic regions, respectively. In Figure 2.16 only the results using the SST turbulence model are plotted. Here it is noted that there is excellent agreement between the FLUENT and WIND runs with the SST turbulence model. Profiles of the mean streamwise velocity (V/V_m) are shown in Figure 2.17 for six axial locations in the jet plume. From these profiles it is seen that there are only slight differences between the various turbulence models for the mean velocities in the region upstream of the potential core. However, some variations are seen at axial locations further downstream ($X/D > 7$). Based on these mean velocity profiles it appears that the WIND SST, FLUENT SST, and FLUENT standard $k - \epsilon$ model solutions provide the best agreement with the experimental PIV data. Profiles of the turbulence intensity ($k^{1/2}/V_m(\%)$) at the same axial locations are shown in Figure 2.18. Again it is seen that most solutions from both WIND and FLUENT tend to over-predict the turbulence levels in the jet plume. The only exceptions are the results from the FLUENT $k - \omega$ and WIND Chien $k - \epsilon$ turbulence models, which were previously shown to have considerably poor agreement for the mean velocities.

2.4.3 Final Confluent Mixer Results

The final CFD runs for the confluent mixer were run with the standard G1 grid using WIND with the SST turbulence model. The mean velocity profiles for the confluent mixer at set point 5000 are shown in Figure 2.19. The core and bypass nozzle pressure ratios and nozzle temperature ratios are equal for set point 5000. As a result, this set point represents a simulated single stream jet. In Figure 2.19 the mean velocity profiles are scaled by the nondimensional shear layer parameter, η , which is defined as

$$\eta = \frac{R - D/2}{X} \quad (2.2)$$

where R is the radial coordinate, X is the axial coordinate, and D is the nozzle diameter. It is seen in Figure 2.19 that the velocity profiles collapse as expected when plotted as a function of η . The corresponding turbulence intensity profiles in the jet plume are shown in Figure 2.20. It is seen in Figure 2.20 that the turbulence intensity profiles also follow the expected behavior and collapse when plotted as a function of η . It is noted that Figure 2.20 shows that the WIND calculations of a simulated single stream jet over-predicts the turbulence intensities. The WIND calculations for this case have a peak turbulence intensity of 16.4%. Traditionally, experiment data has shown that single stream jets typically have peak turbulence intensities of 15% [112–116].

The turbulence intensity profiles of the final CFD analysis of the confluent mixer at set point 312 are shown in Figure 2.21. In this figure the turbulence intensity profiles are scaled by the nondimensional radius, R/D . Using the standard scaling laws [117] the peak turbulence levels in the bypass-ambient and core-bypass shear layers should be 10.9% and 8.5% of the mixed jet velocity, respectively for the set point 312 operating conditions. These expected peak turbulence intensities are calculated based on the ideal jet velocities for the core, bypass, and freestream flows. It is seen in Figure 2.21 that the WIND analysis over-predicts the turbulence in the shear layers, resulting in peak values of 13% for the bypass-ambient shear layer and

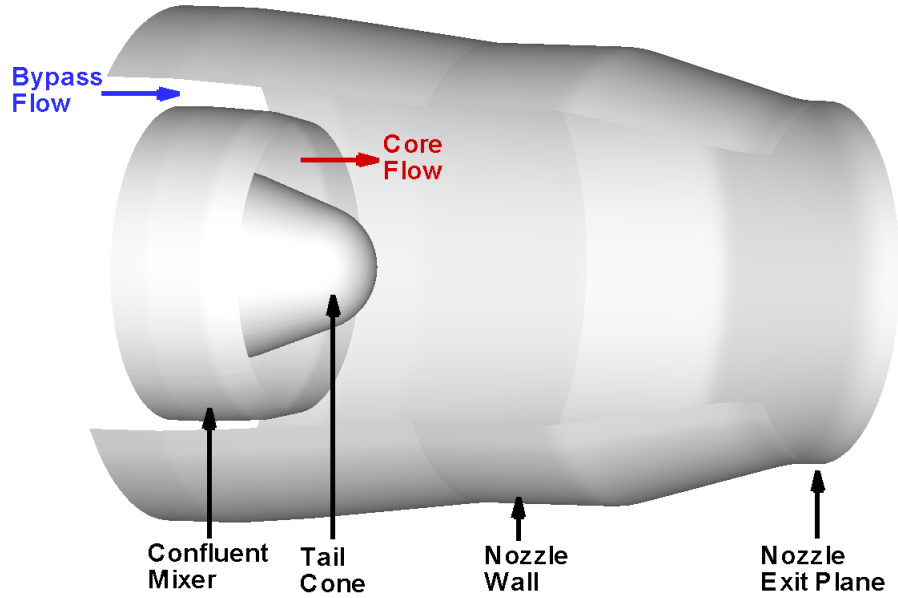


Figure 2.7. Schematic of the confluent mixer geometry with the baseline L0 nozzle.

10% for the core-bypass shear layer. It is noted in Figure 2.21 that for the PIV data the peak turbulence intensities in the bypass-ambient shear layer are in agreement with the expected values. However, it is noted that the peak turbulence intensities in the core-bypass shear layer are slightly higher than the expected values for axial locations greater than 2 diameters downstream. It is likely that this discrepancy is due to the interaction of the core-bypass shear layer with the turbulent flow that is shed by the separation over the end of the tailcone. Evidence supporting this theory is seen in the elevated turbulence levels near the centerline in the upstream planes of PIV data. It is also possible that some of the differences seen in the turbulence kinetic energy in the PIV data are due to the post-processing methodology, which is described in more detail in Appendix A.

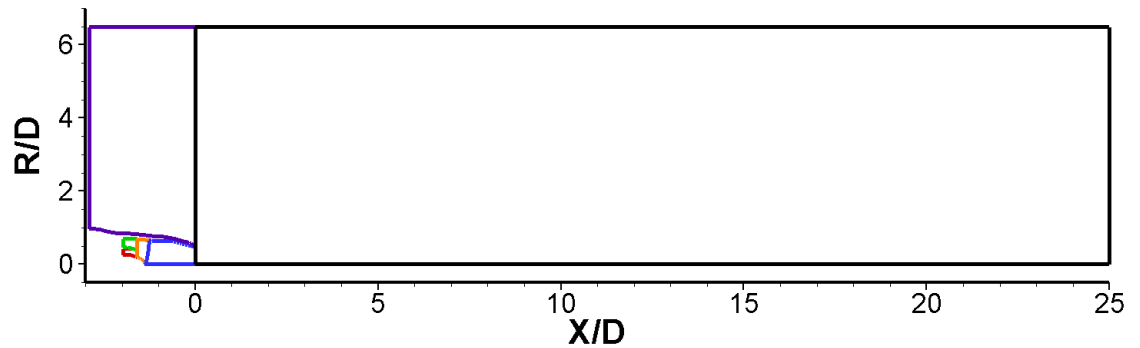


Figure 2.8. Zone layout for the confluent mixer grids.

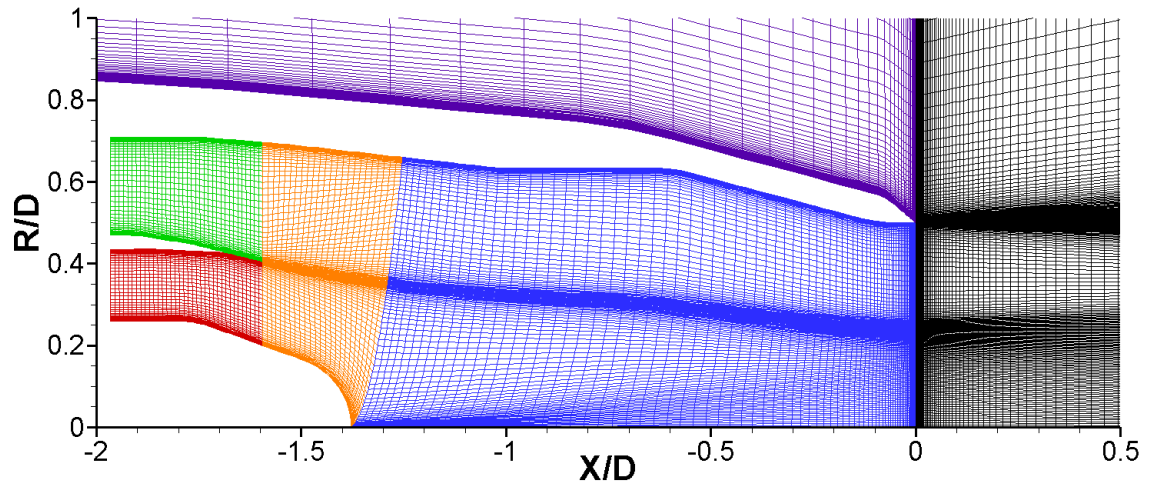


Figure 2.9. Nozzle interior region of the standard (G1) confluent mixer grid.

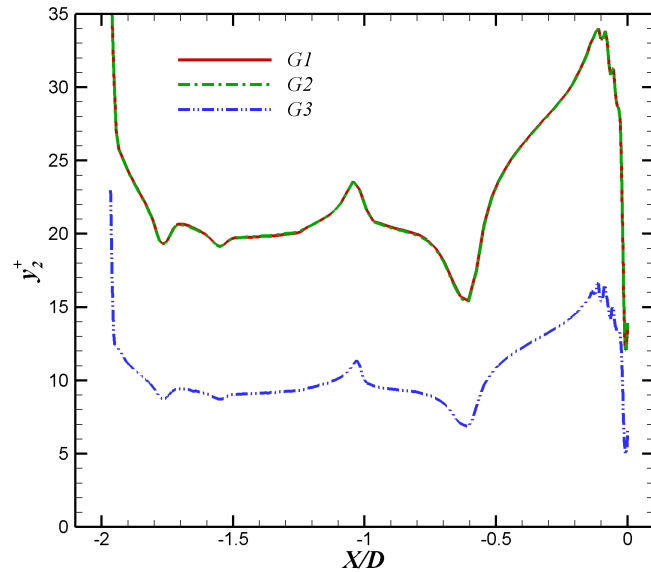


Figure 2.10. Variation of y_2^+ along the nozzle interior wall for the confluent mixer at set point 312 for the G1, G2 and G3 grids.

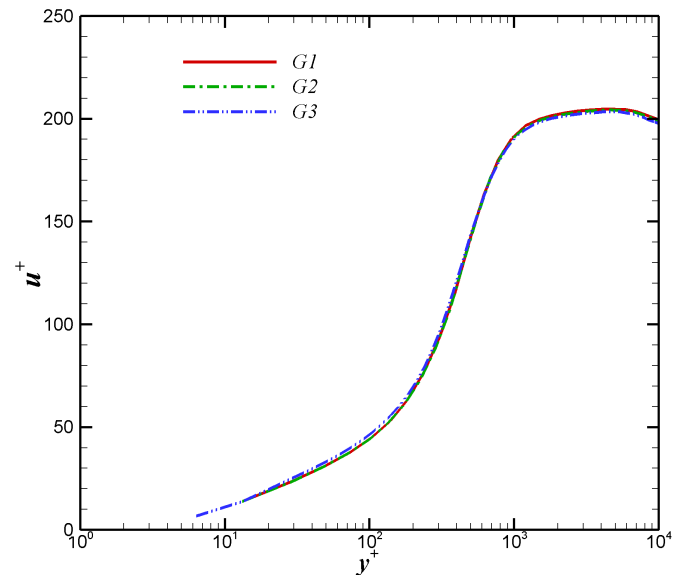


Figure 2.11. Boundary layer profiles at the nozzle exit plane for the confluent mixer at set point 312 for the G1, G2 and G3 grids.

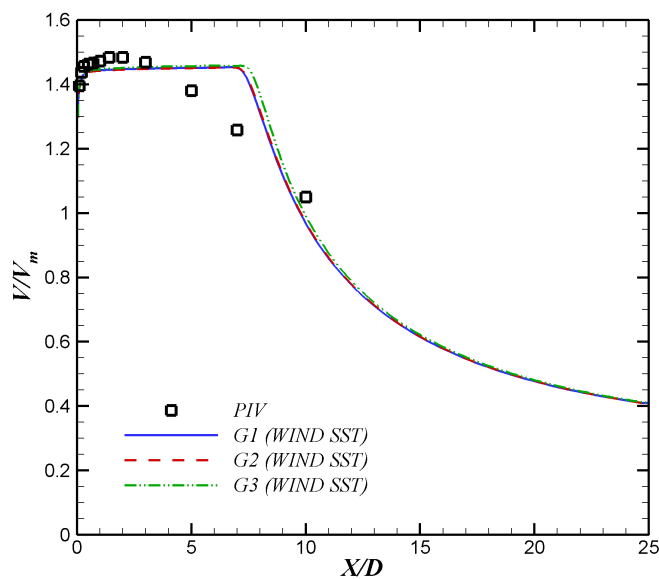


Figure 2.12. Centerline velocities for the confluent mixer at set point 312 for the G1, G2 and G3 grids.

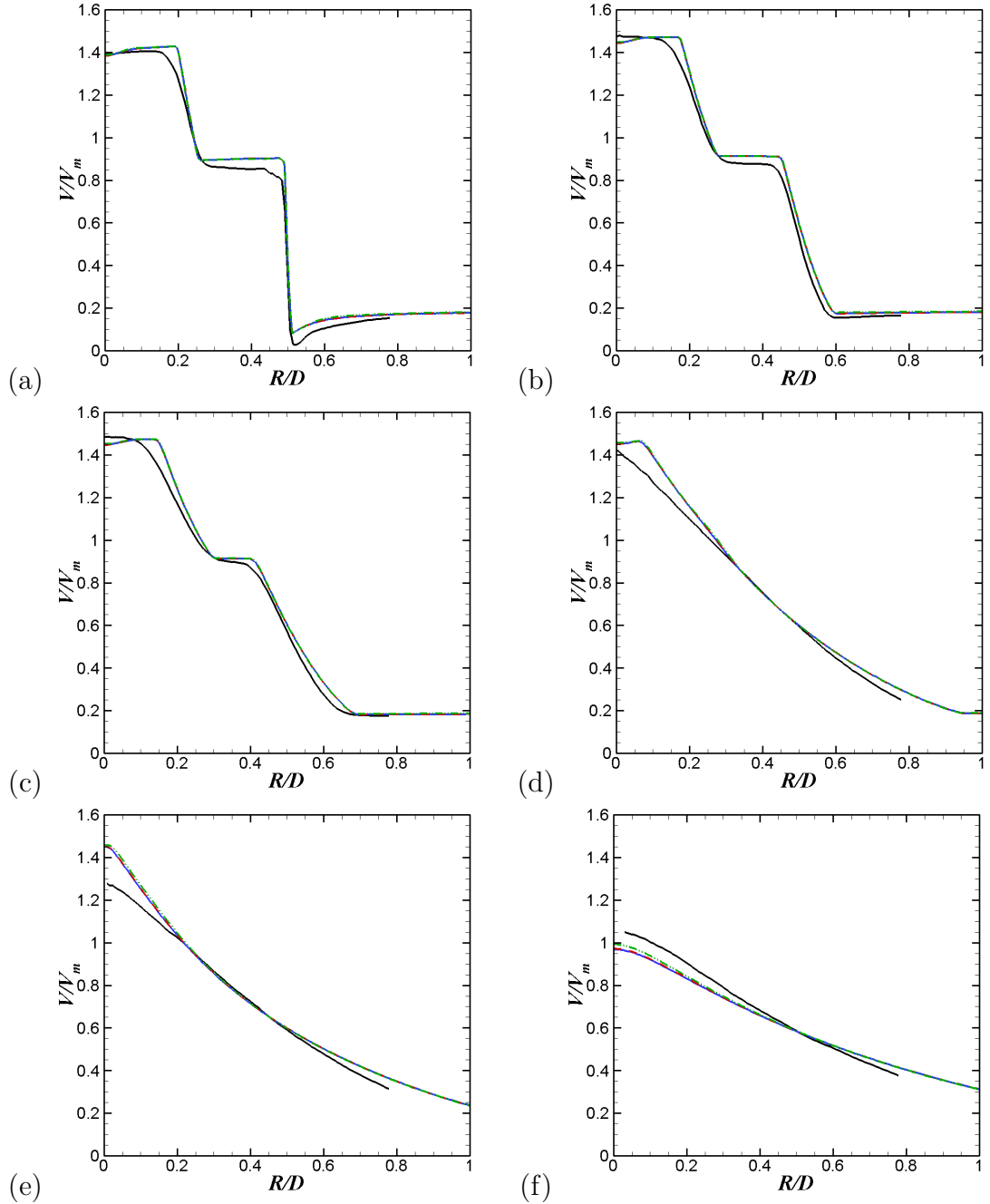


Figure 2.13. Velocity profiles for the confluent mixer at set point 312 for the G1, G2 and G3 grids at $X/D =$ (a) 0.1, (b) 1.0, (c) 2.0, (d) 5.0, (e) 7.0, (f) 10.0. Solid black line is the PIV data; other line types are the same as Figure 2.12.

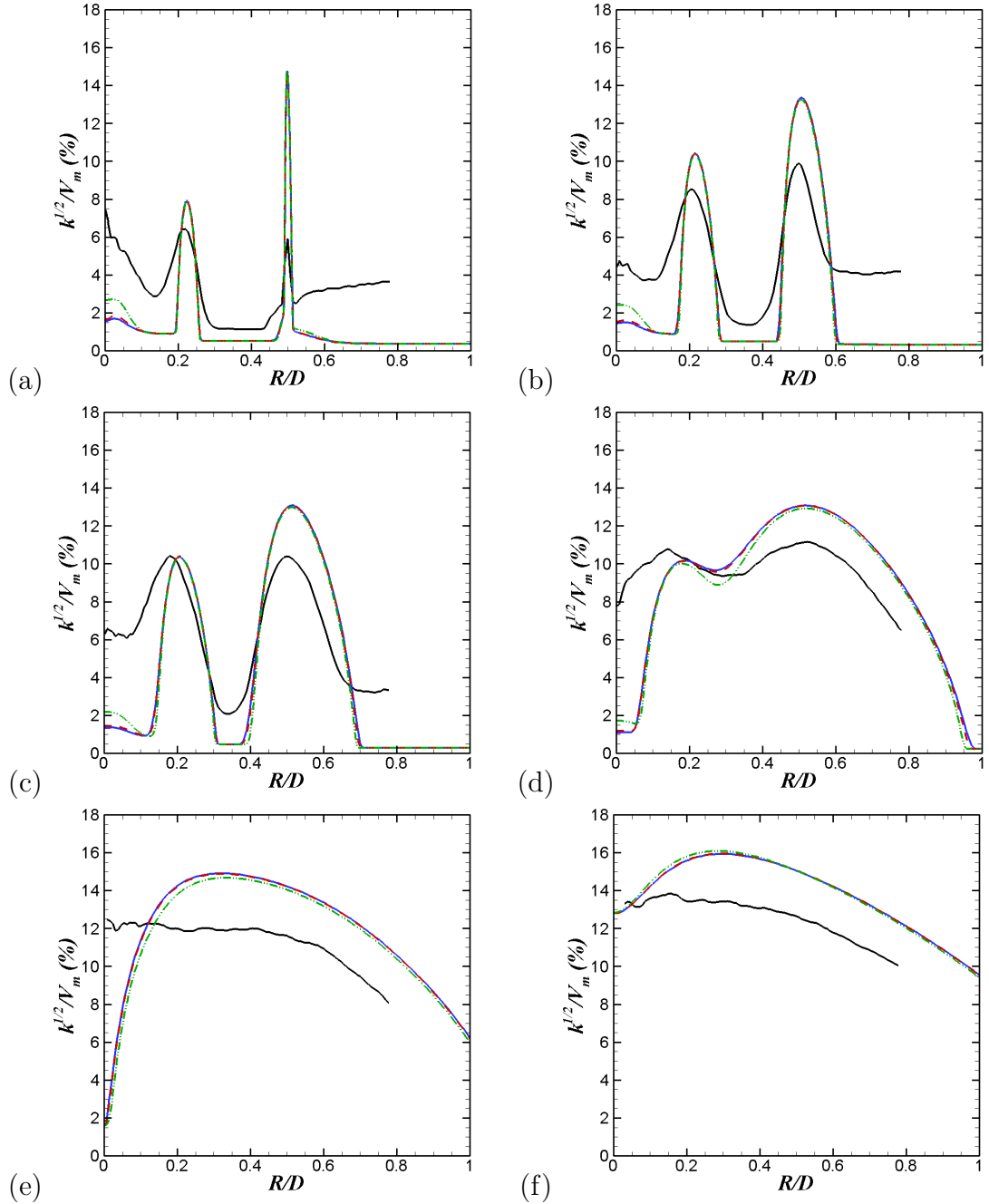


Figure 2.14. Turbulence intensity profiles for the confluent mixer at set point 312 for the G1, G2 and G3 grids at $X/D =$ (a) 0.1, (b) 1.0, (c) 2.0, (d) 5.0, (e) 7.0, (f) 10.0. Solid black line is the PIV data; other line types are the same as Figure 2.12.

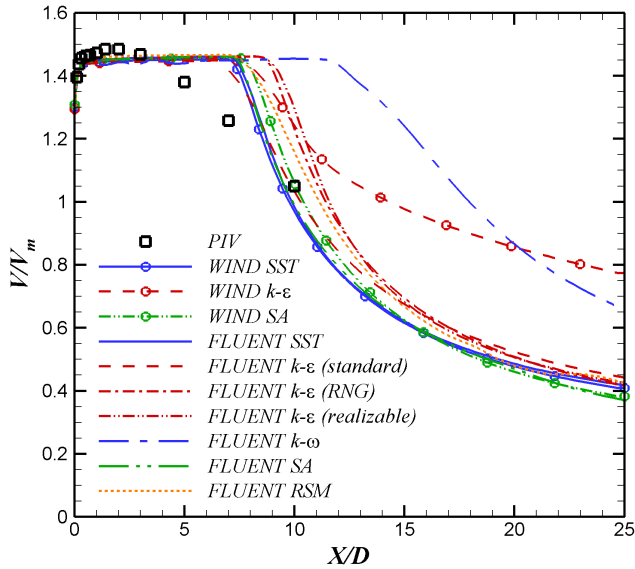


Figure 2.15. Centerline velocities for the confluent mixer (G1 grid) at set point 312 for various turbulence models.

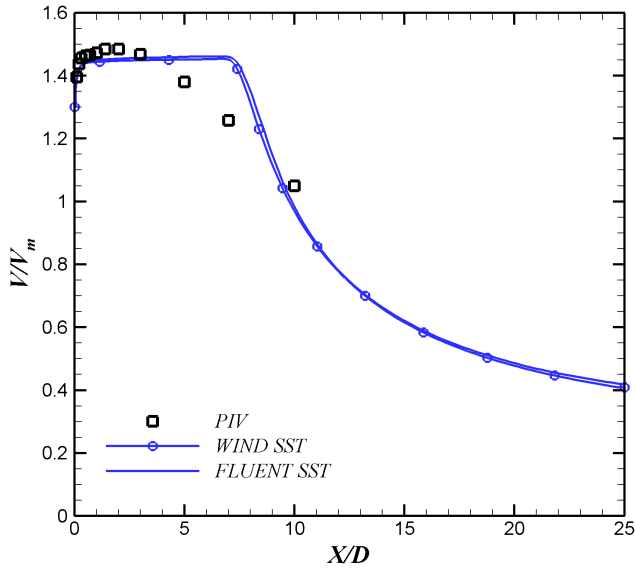


Figure 2.16. Centerline velocities for the confluent mixer (G1 grid) at set point 312 for WIND and FLUENT with the SST turbulence model.

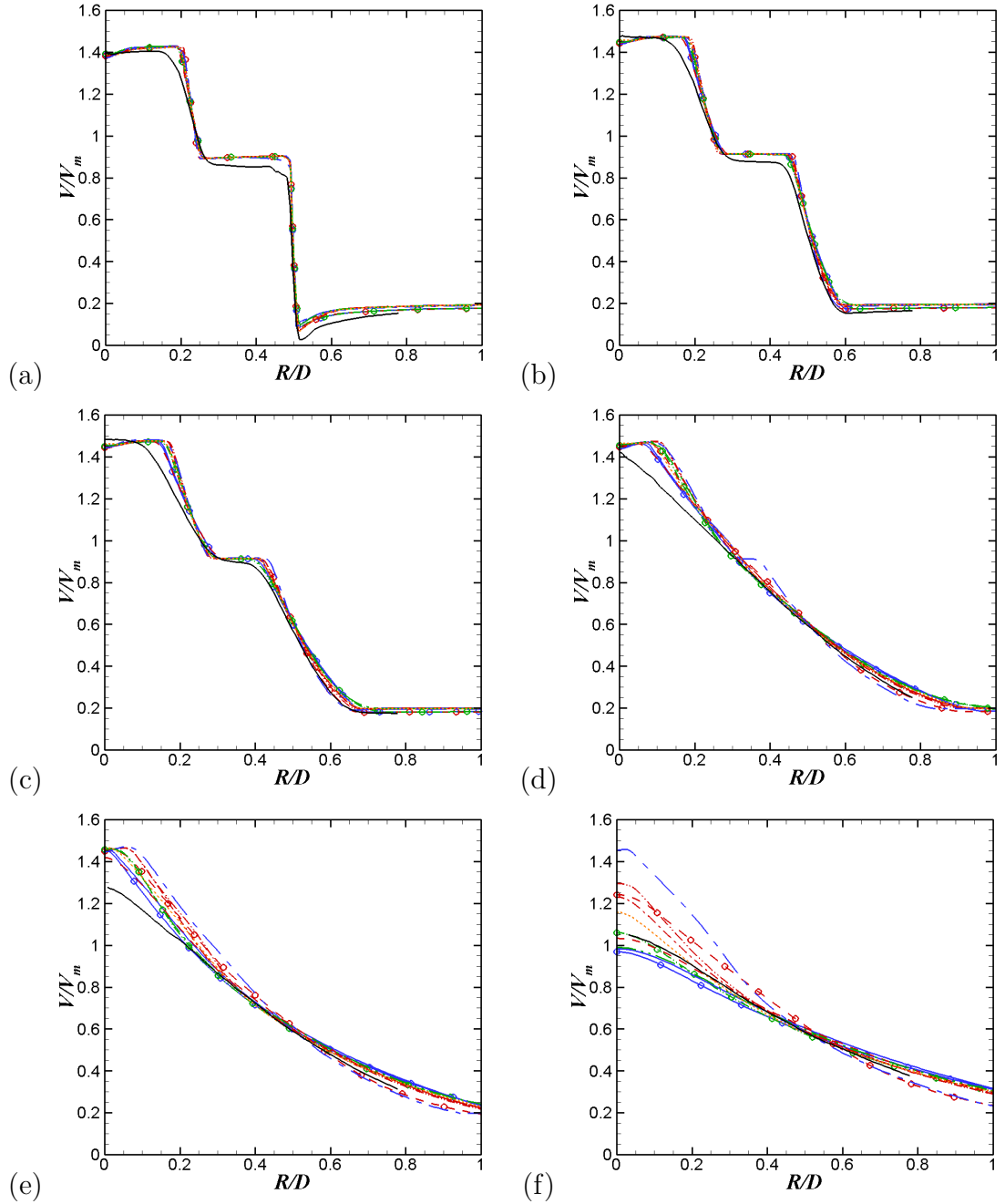


Figure 2.17. Velocity profiles for the confluent mixer (G1 grid) at set point 312 for various turbulence models at $X/D =$ (a) 0.1, (b) 1.0, (c) 2.0, (d) 5.0, (e) 7.0, (f) 10.0. Solid black line is the PIV data; other line types are the same as Figure 2.15.

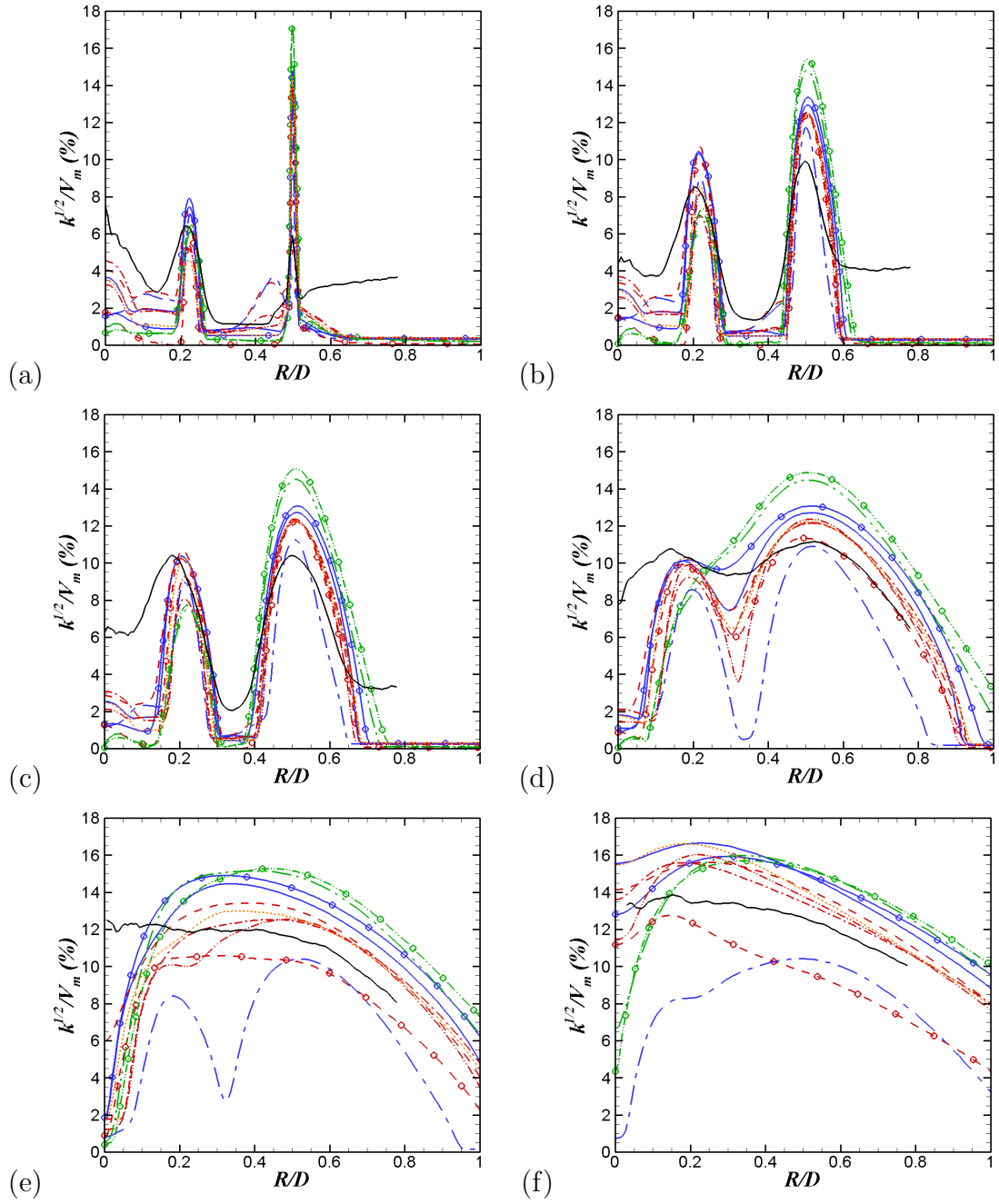


Figure 2.18. Turbulence intensity profiles for the confluent mixer (G1 grid) at set point 312 for various turbulence models at $X/D =$ (a) 0.1, (b) 1.0, (c) 2.0, (d) 5.0, (e) 7.0, (f) 10.0. Solid black line is the PIV data; other line types are the same as Figure 2.15.

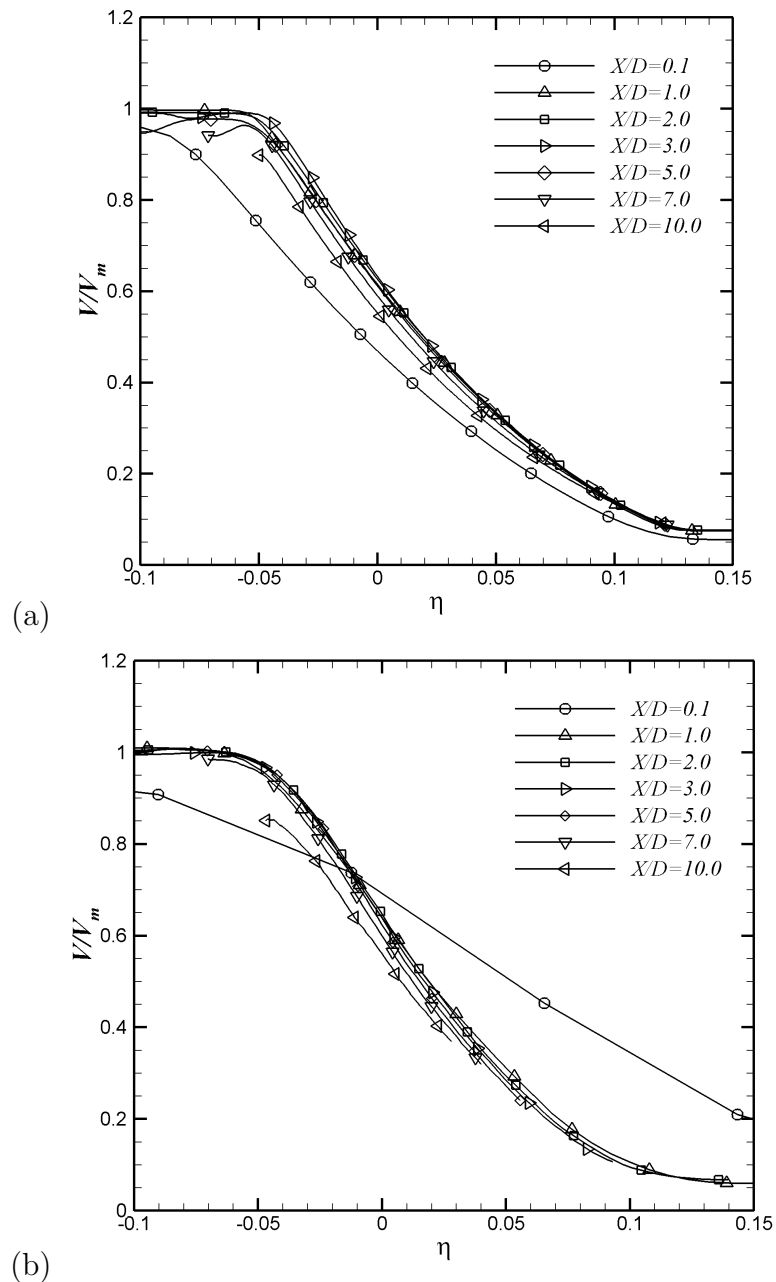


Figure 2.19. Velocity profiles for the confluent mixer at set point 5000 scaled with η ; (a) CFD; (b) PIV.

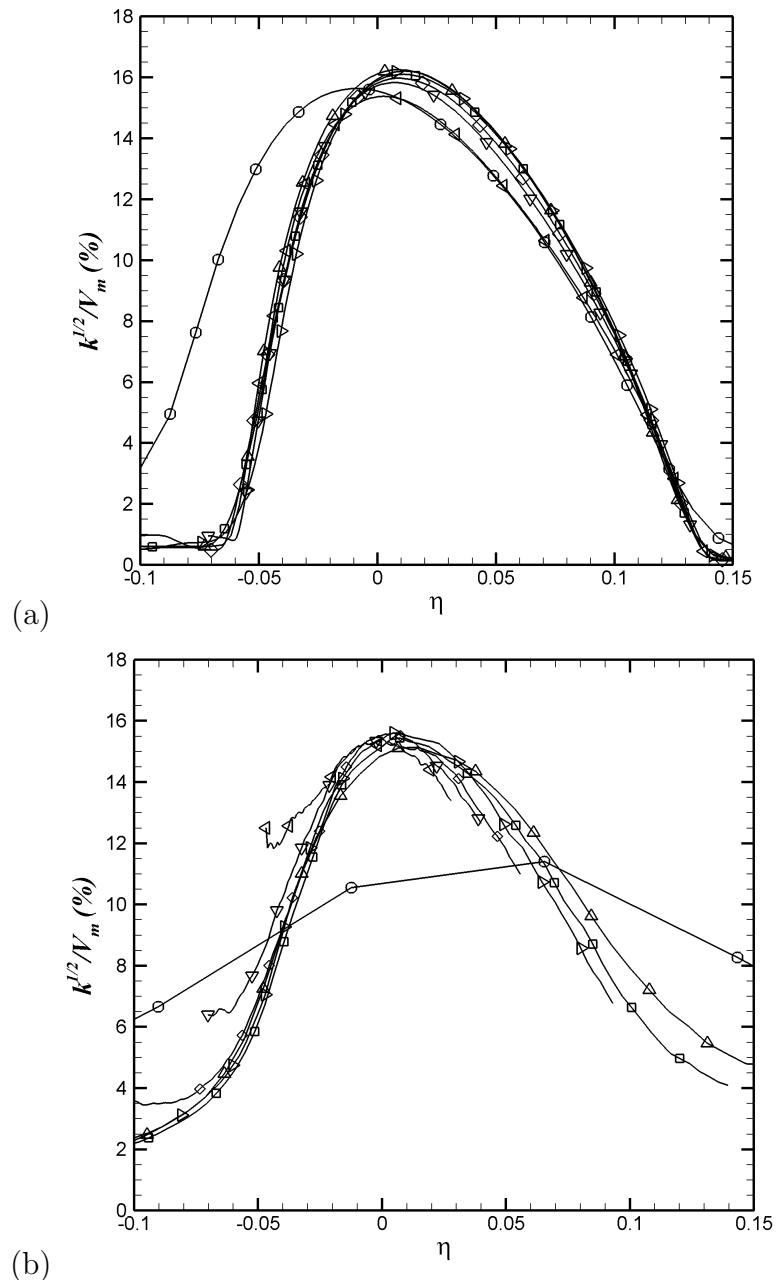


Figure 2.20. Turbulence intensity profiles for the confluent mixer at set point 5000 scaled with η ; (a) CFD; (b) PIV. Line types are the same as Figure 2.19.

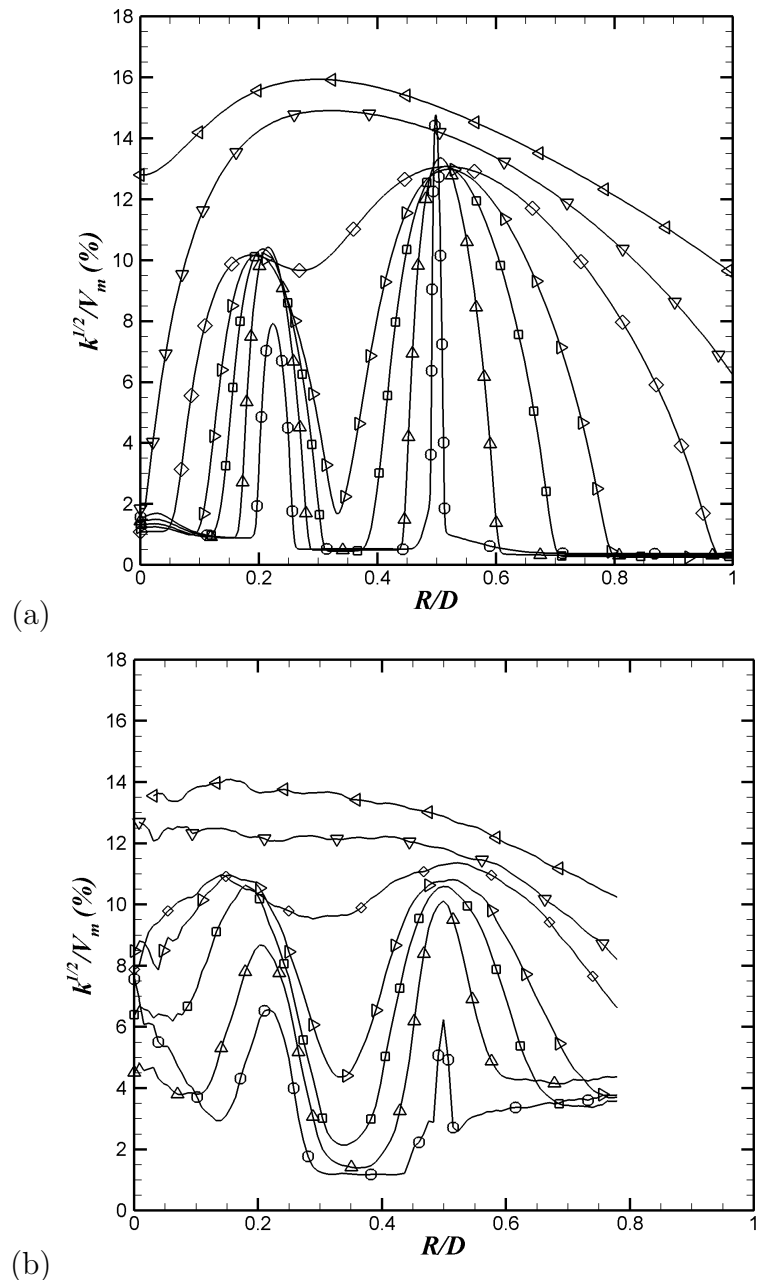


Figure 2.21. Turbulence intensity profiles for the confluent mixer at set point 312 scaled with R/D ; (a) CFD; (b) PIV. Line types are the same as Figure 2.19.

2.5 Lobed Mixer Analysis

A schematic of a typical lobed mixer configuration with baseline L0 nozzle is shown in Figure 2.22. In the lobed mixer configurations the simple axisymmetric splitter plate is replaced by a lobed mixer, which is essentially a convoluted splitter plate. The addition of the lobes to the mixer introduces streamwise vorticity, which leads to the formation of streamwise vortices that enhance the mixing of the bypass and core streams.

2.5.1 Grid Sensitivity

The standard grid (G1) for the 20-lobed, high penetration (20UH) mixer configuration contains 1.2 million grid points, which are divided into 12 zones. The zone layout for lobed mixer grids is shown in Figure 2.23. For the 3-D lobed mixer cases the plume region is divided into a number of separate zones, as shown in Figure 2.23. These extra zone divisions are necessary to improve the efficiency of the parallel computations. This increase in efficiency is obtained by increasing the maximum number of processors that can be used and by equalizing the load for each processor. When dividing the plume region it is important to avoid introducing zone boundaries that run through regions of high shear, such as the main jet shear layer. For instance, having a zone boundary at the nozzle lip line that runs the length of the plume will lead to large errors and sharp discontinuities in the mean flow and turbulence quantities. Many of these issues are due to the fact that WIND uses a zero order interpolation for the turbulence quantities across zone boundaries. Errors introduced by the zone coupling are minimized by dividing the plume region in a manner that produces zone boundaries that are perpendicular to the main jet shear layer, as shown in Figure 2.23. The grid point distribution for each zone in the standard (G1) 20UH mixer grid is given in [Table 2.6](#). This grid extends 5.5 diameters in the radial direction and 10 diameters in the axial direction. The wall normal grid spacings are set as $0.00005D$ (3.625E-4 inches) at all viscous wall boundaries. In

addition the axial spacing at the nozzle exit is set as $0.001D$ (7.25E-3 inches). These spacings are identical to those in the standard (G1) confluent mixer grid. In the interior region of the zones the grid lines were packed near the main jet shear layer and in the vicinity of the streamwise vortices. Additional details of the grid generation process are included in Appendix B. An example of the computational grid near the nozzle interior region of the standard 20UH mixer configuration is shown in Figure 2.24.

The standard (G1) 20UH mixer grid contains 33 points in the azimuthal direction. In addition to this standard grid, two additional grids were generated that contained 41 and 65 azimuthal points, which are referred to as the G2 and G3 grids, respectively. These additional grids were generated to check the azimuthal grid dependence of the resolution of the streamwise vortices that are produced by the lobed mixers. A comparison of the axial vorticity contours at the nozzle exit plane for the G1, G2, and G3 20UH mixer grids at set point 110 is shown in Figure 2.25. In this figure it is observed that there are only minor differences in the axial component of vorticity for the various grids. These minor differences occur in the secondary flow structure that forms between the primary vortex and the centerline. However, the

Table 2.6 Grid point distribution for the standard 20UH mixer grid (G1)

Zone	Axial	Radial	Azimuthal
	Dimension	Dimension	Dimension
1	33	65	33
2	33	65	33
3	37	129	33
4	89	129	33
5	37	89	33
6	145	217	33

structure of the main vortex appears to be adequately resolved by the coarsest grid (G1).

The primary quantity from the CFD analysis that is applied to the far field noise prediction models is the turbulence kinetic energy. It is important, therefore, to also check the azimuthal grid dependence of the turbulence levels in the streamwise vortices. In Figure 2.26 the turbulence intensities at the nozzle exit plane for the three 20UH grids are compared. Here it is again seen that the turbulence levels in the streamwise vortices are virtually identical for the three 20UH mixer grids. The peak turbulence intensities in the center of the vortices were 7.78%, 7.78%, and 7.73% for the G1, G2, and G3 grids, respectively. For the lobed mixer configurations downstream of the nozzle exit the turbulent streamwise vortices eventually interact with the growing main jet shear layer. When this interaction occurs the turbulence levels in the main shear layer are enhanced, resulting in increased noise. The noise models that are developed in the subsequent chapters are dependent on the variation of the peak turbulence levels in the jet plume, which vary based on the mixer configuration. Therefore, it is necessary to also check the azimuthal grid dependence of these peak turbulence intensities in the plume. In Figure 2.27 the axial variation of peak turbulence intensity is compared between the three 20UH mixer grids. It is observed that the finest grid (G3) shows some oscillations in the peak turbulence levels in the downstream portion of the domain where the solution has not yet converged to a steady-state value. However, the peak turbulence levels further upstream have converged. In this region it is noted that the peak levels in the axial variation are nearly identical for the three grids, which is expected since the turbulence levels in the streamwise vortices at the nozzle exit were virtually identical for the three 20UH mixer grids. Based on the preceding analysis it was determined that the standard grid (G1) adequately resolves the flow field for the lobed mixer cases, and it is used in the subsequent work.

2.5.2 Final Lobed Mixer Results

A comparison of the CFD and PIV mean velocities at the $X/D = 0.1$ and $X/D = 1.0$ axial planes for the five lobed mixer geometries is shown in Figure 2.28. In this figure it is seen that for the $X/D = 0.1$ plane the overall structure of the flow field for the 12-lobe mixers is well predicted by the CFD analysis. However, it is noted that for the 20-lobe mixers the CFD predictions show distinct variations in the velocities in the region surrounding the streamwise vortices, where the PIV data appears to show a more uniform velocity distribution. There are a number of possible reasons for these discrepancies. First, the CFD analysis creates a perfectly periodic flow field. It is possible that the experimental cases could have some asymmetries in the mixer geometries. These asymmetries could likely lead to a faster breakup of the vortex structures. Second, it is likely that there were some large scale oscillations in the mixer/nozzle geometry during the experiments that could result from vibrations in the rig. These large scale oscillations would tend to smooth the velocity distribution in the PIV data. Third, for the experiments the vortex trajectories could be unsteady, which would also lead to a smoother velocity distribution in the PIV data. The corresponding comparison of the CFD and PIV turbulence intensities at the $X/D = 0.1$ and $X/D = 1.0$ axial planes for the five lobed mixer geometries is shown in Figure 2.29. In this figure it is again seen that the overall structure of the flow field is well predicted by the CFD analysis. Again, in general it is observed that the PIV data turbulence intensity distribution does not exhibit the same level of definition as the CFD results. However, it is seen that there is reasonable agreement in the magnitude of the turbulence intensities in the vortex structures. To compare the CFD results to the PIV data in a more quantitative manner, azimuthally averaged profiles of the mean velocities and turbulence intensities are evaluated in addition to the previously described contour plots.

The CFD and PIV azimuthally averaged profiles of the mean velocity and turbulence intensity for the 12CL mixer are compared in Figure 2.30. In this comparison it

is observed that there is excellent agreement between the CFD and PIV azimuthally averaged mean velocities at all axial locations. Furthermore, it is observed that the overall structure of the azimuthally averaged turbulence intensity profiles is well predicted by the CFD analysis. However, notable differences are seen in the magnitude of the peak turbulence intensities in the main jet shear layer, with the CFD results showing a slight over-prediction.

The CFD and PIV azimuthally averaged profiles of the mean velocity and turbulence intensity for the 12UM mixer are compared in Figure 2.31. In this comparison it is again seen that there is excellent agreement between the CFD and PIV azimuthally averaged mean velocities at all axial locations. For the 12UM mixer data is seen that the peak turbulence intensities in the main jet shear layer are slightly over-predicted for the upstream planes ($X/D < 3$). However, farther downstream the peak turbulence intensities are slightly under-predicted by the CFD analysis.

The CFD and PIV azimuthally averaged profiles of the mean velocity and turbulence intensity for the 12UH mixer are compared in Figure 2.32. In this comparison it is seen that there is good agreement between the CFD and PIV azimuthally averaged mean velocities at all axial locations. It is also observed that for the 12UH mixer the peak turbulence intensities in the main jet shear layer are also slightly over-predicted for the upstream planes ($X/D < 5$). However, at the farthest downstream plane ($X/D = 10$) the peak turbulence intensities are slightly under-predicted by the CFD analysis.

The CFD and PIV azimuthally averaged profiles of the mean velocity and turbulence intensity for the 20UH mixer are compared in Figure 2.33. In this comparison it is seen that there is excellent agreement between the CFD and PIV azimuthally averaged mean velocities at all axial locations. Furthermore it is seen that the peak turbulence intensities in the main jet shear layer are also slightly over-predicted by the CFD analysis.

The CFD and PIV azimuthally averaged profiles of the mean velocity and turbulence intensity for the 20DH (scalloped) mixer are compared in Figure 2.34. In

in this comparison it is observed that there appear to be some differences in the CFD and PIV azimuthally averaged mean velocity profiles. In particular the CFD profiles show a larger radial variation in the streamwise velocities. Similar discrepancies in the profile structure are also seen in the turbulence intensity data. In addition, the peak turbulence intensities in the main jet shear layer are also over-predicted for the CFD analysis of the 20DH mixer.

In the preceding summary of the CFD analysis it was observed that the WIND-SST calculations typically over-predict the turbulence levels in a simple single jet shear layer, and they under-predict the enhancement of the peak turbulence levels for the forced mixer cases. Despite these discrepancies it is seen that the CFD calculations do predict the correct trends in the enhanced turbulence levels for various mixer configurations. These trends are highlighted in the contour plots of the turbulence levels in the PIV and CFD data shown in Figures 2.35 and 2.36, respectively. In particular, it is noted that the CFD predictions correctly identify the trend of increased turbulence enhancement with increased lobe penetration height. In addition, the CFD predictions correctly predict that the location of the enhanced turbulence moves upstream with increasing lobe penetration height. The correct prediction of these trends suggests that using these CFD results for noise modeling calculations should produce the correct trends in the acoustic predictions.

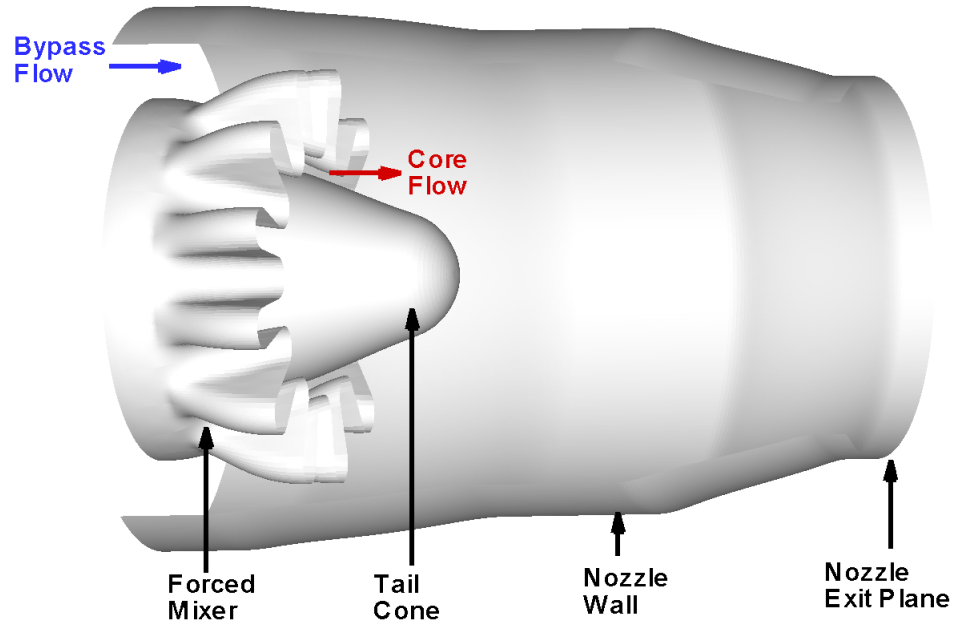


Figure 2.22. Schematic of the typical lobed mixer geometry with the baseline L0 nozzle.

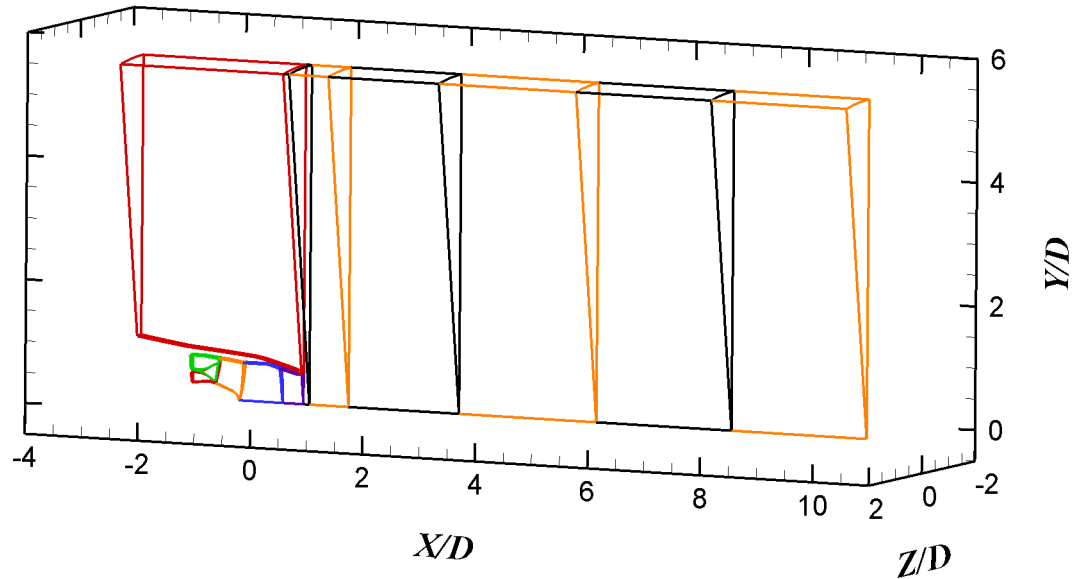


Figure 2.23. Zone layout for the lobed mixer grids.

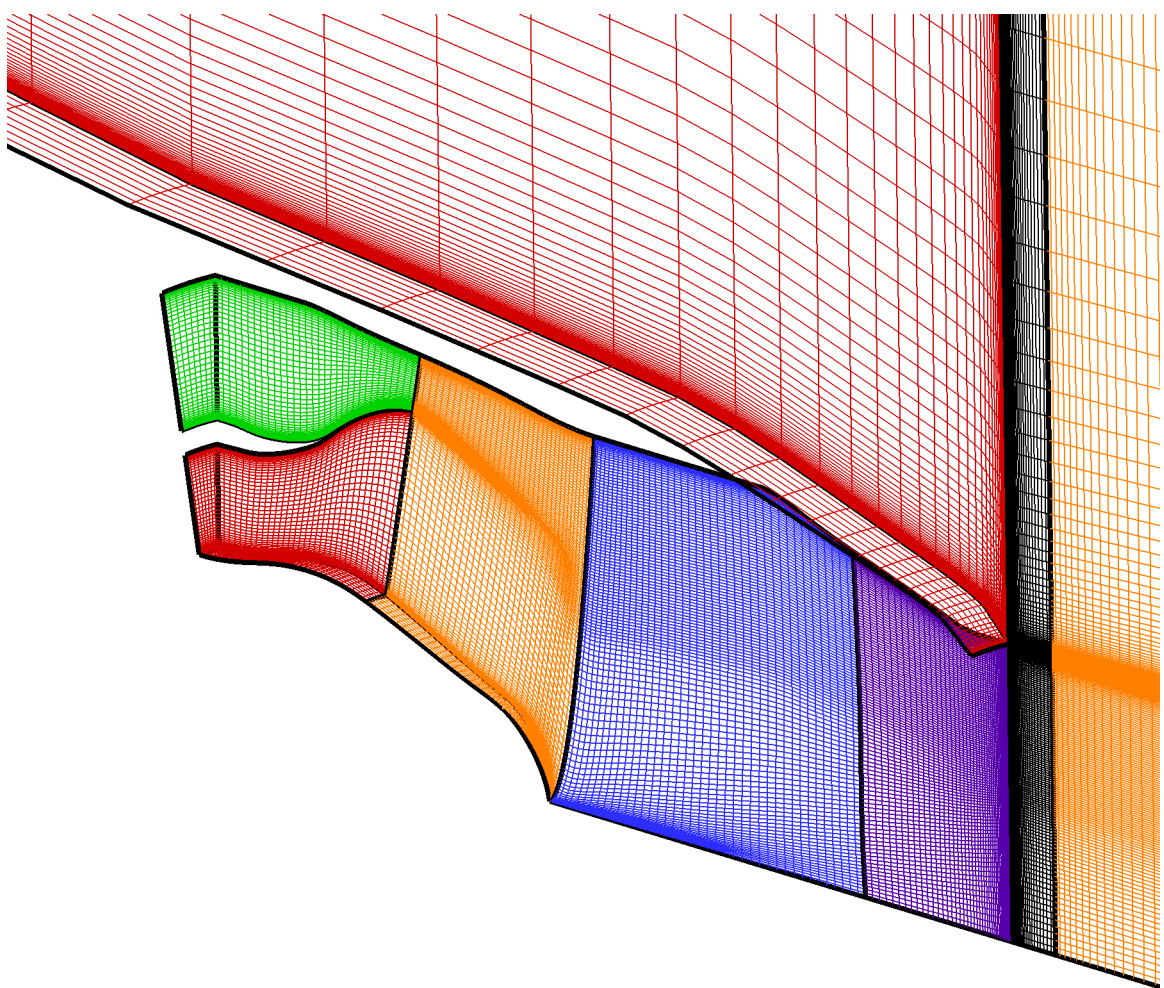


Figure 2.24. Nozzle interior region of the standard (G1) 20UH mixer grid. Every fourth azimuthal grid point is shown for clarity.

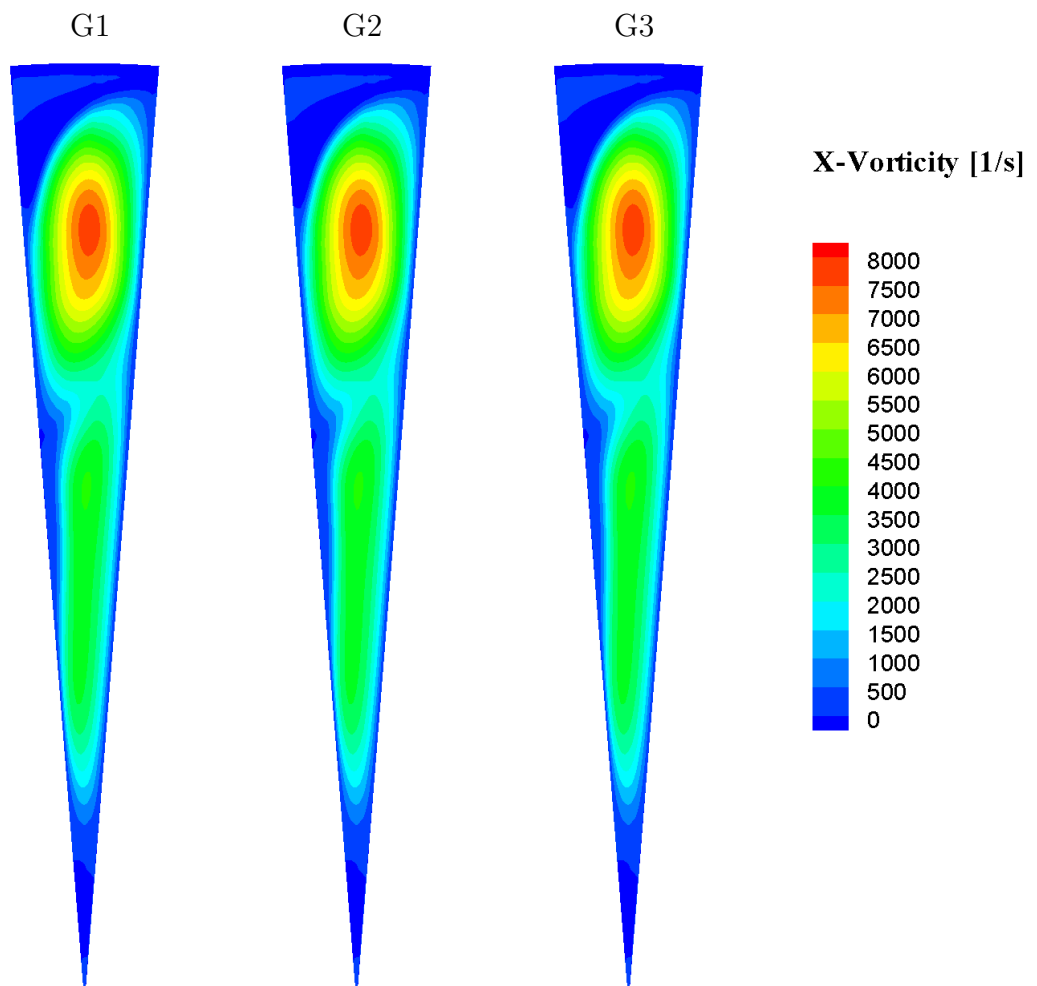


Figure 2.25. Comparison of the axial vorticity at the nozzle exit plane for the G1, G2, and G3 20UH mixer grids.

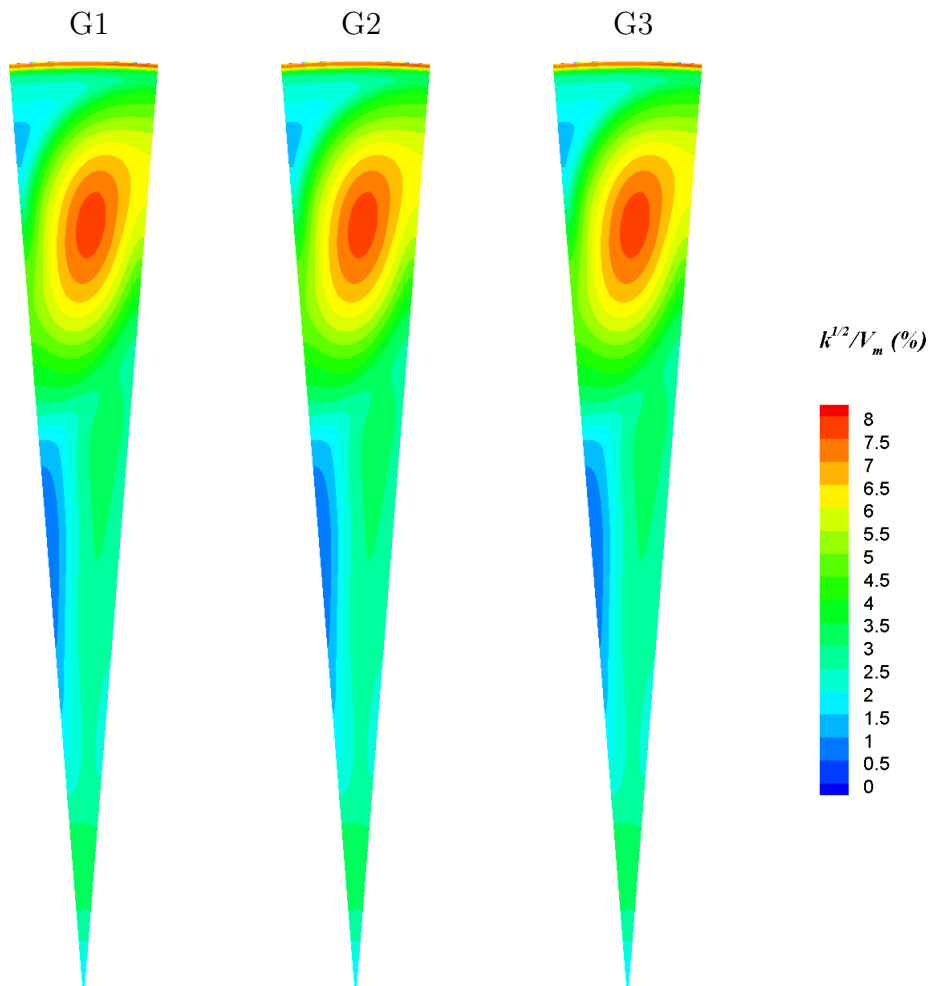


Figure 2.26. Comparison of the turbulence intensities at the nozzle exit plane for the G1, G2, and G3 20UH mixer grids.

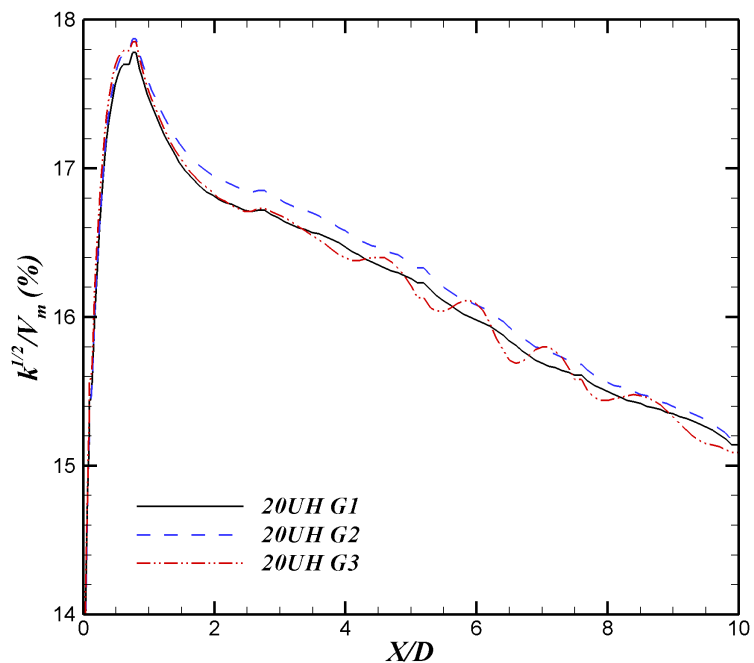


Figure 2.27. Comparison of the peak turbulence intensities in the plume for the G1, G2, and G3 20UH mixer grids.

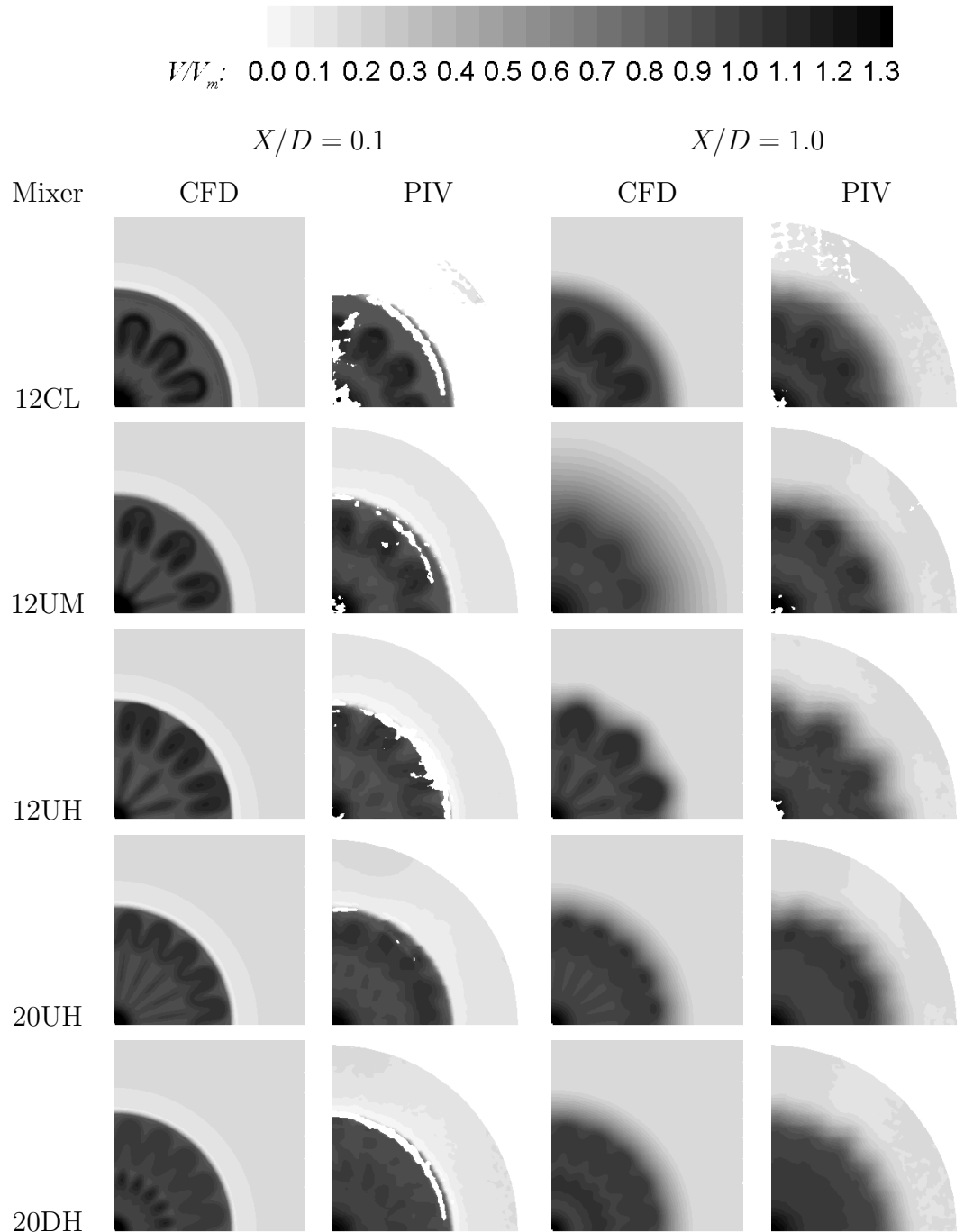


Figure 2.28. Comparison of the CFD and PIV mean streamwise velocities in the jet plume at $X/D = 0.1$ and $X/D = 1.0$.

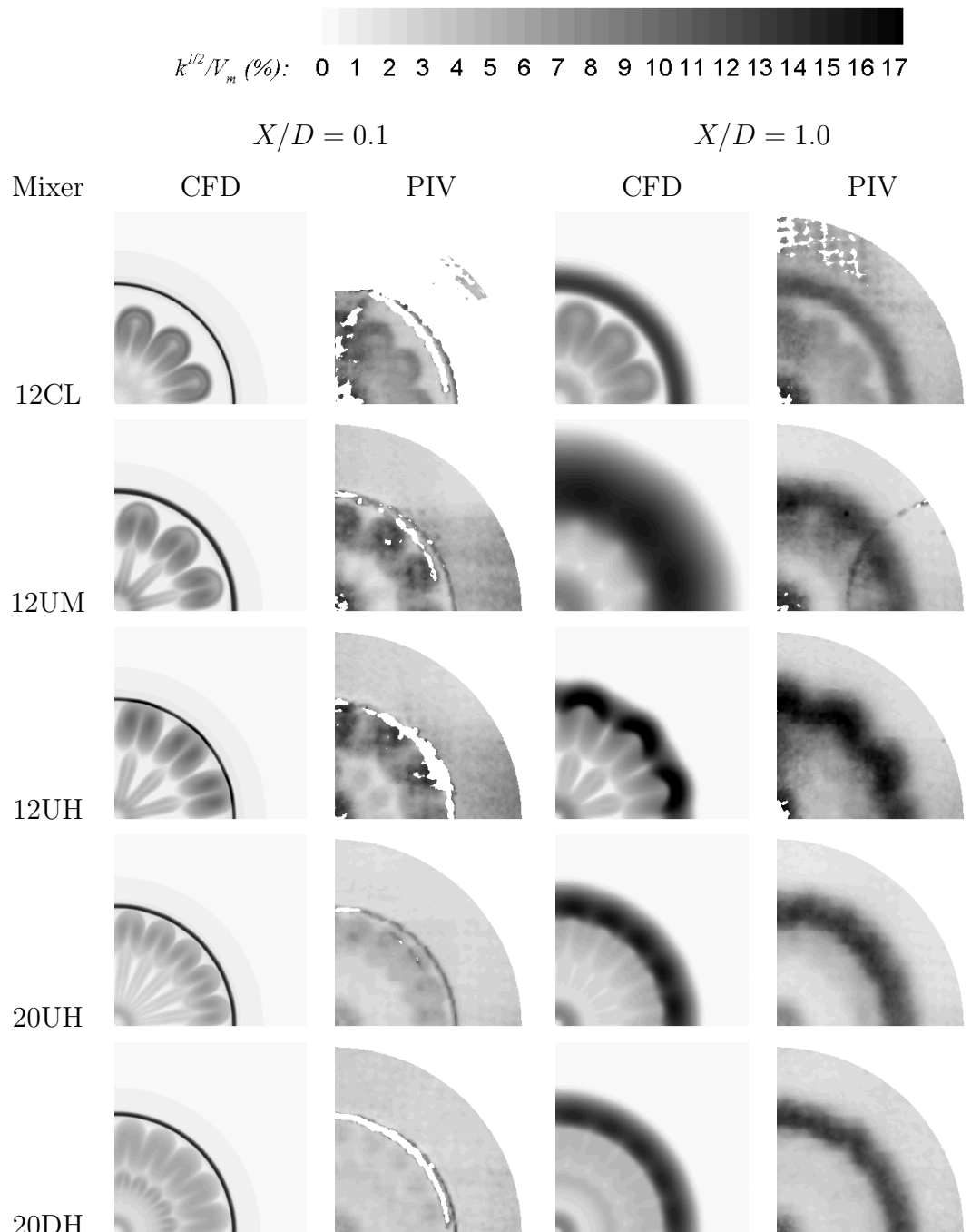


Figure 2.29. Comparison of the CFD and PIV turbulence intensities in the jet plume at $X/D = 0.1$ and $X/D = 1.0$.

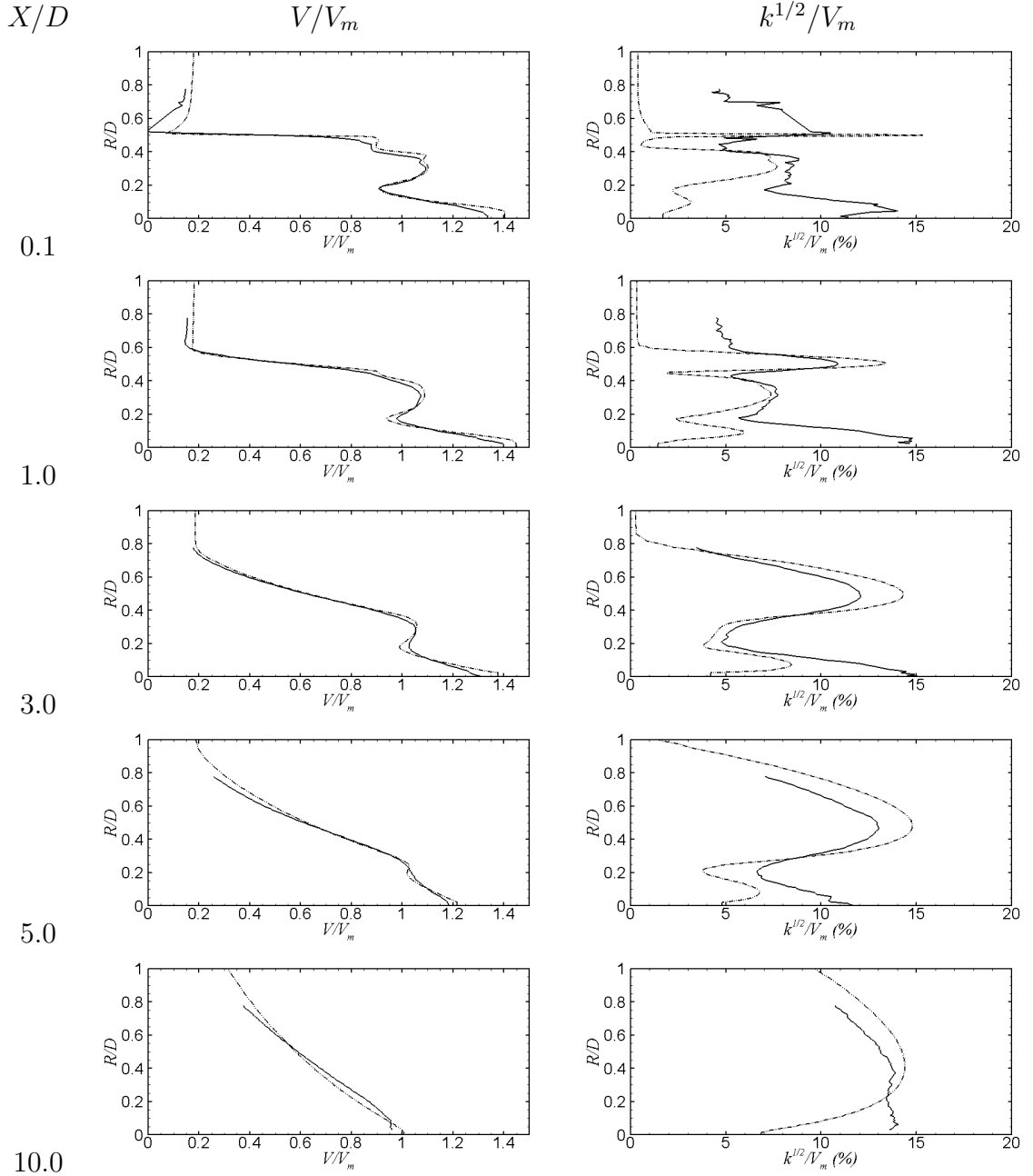


Figure 2.30. Comparison of the CFD and PIV azimuthally averaged profiles of mean streamwise velocity and turbulence intensity at various axial locations in the jet plume for the 12CL mixer; solid line, PIV data; dash-dot line, CFD data.

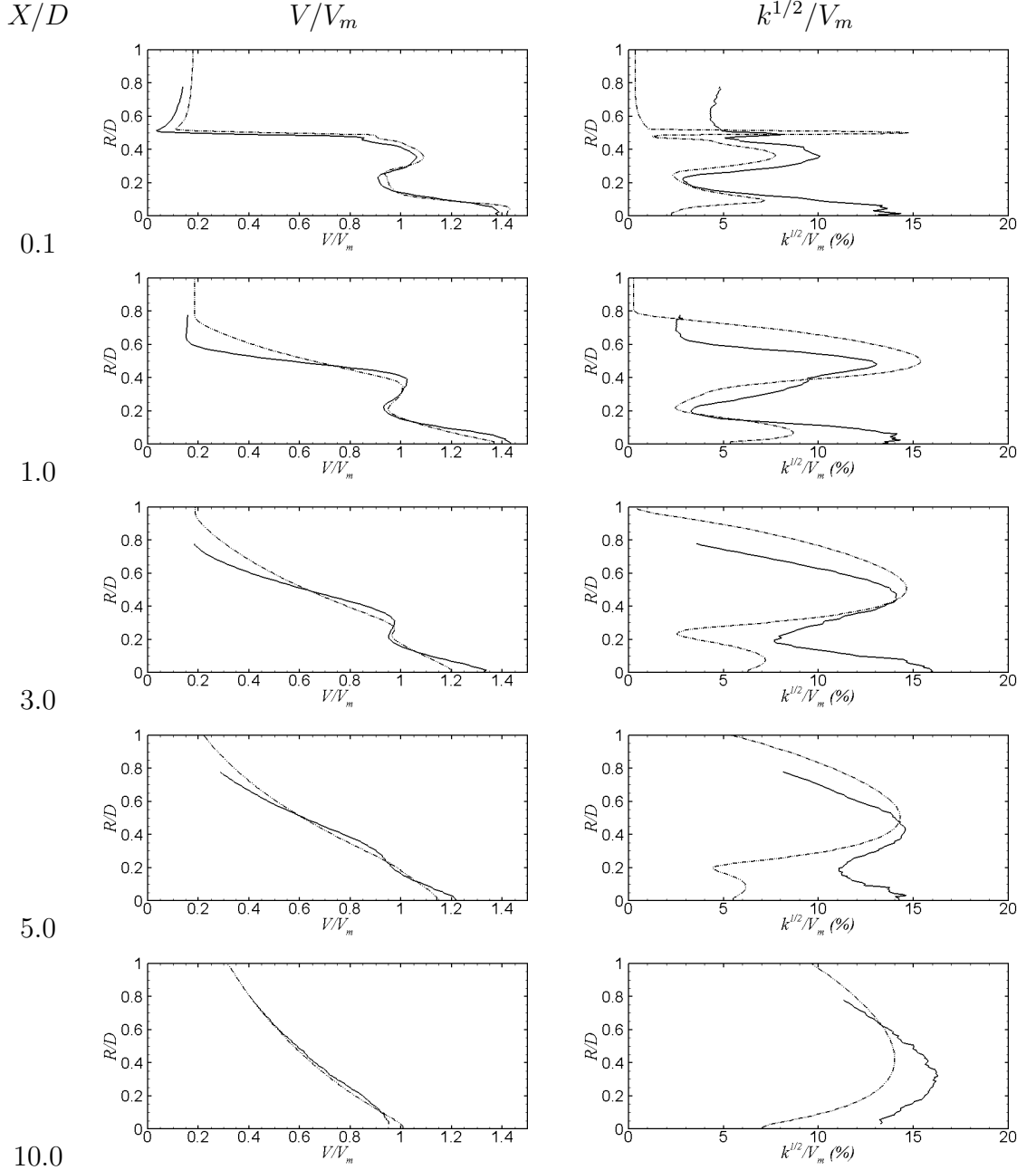


Figure 2.31. Comparison of the CFD and PIV azimuthally averaged profiles of mean streamwise velocity and turbulence intensity at various axial locations in the jet plume for the 12UM mixer; solid line, PIV data; dash-dot line, CFD data.

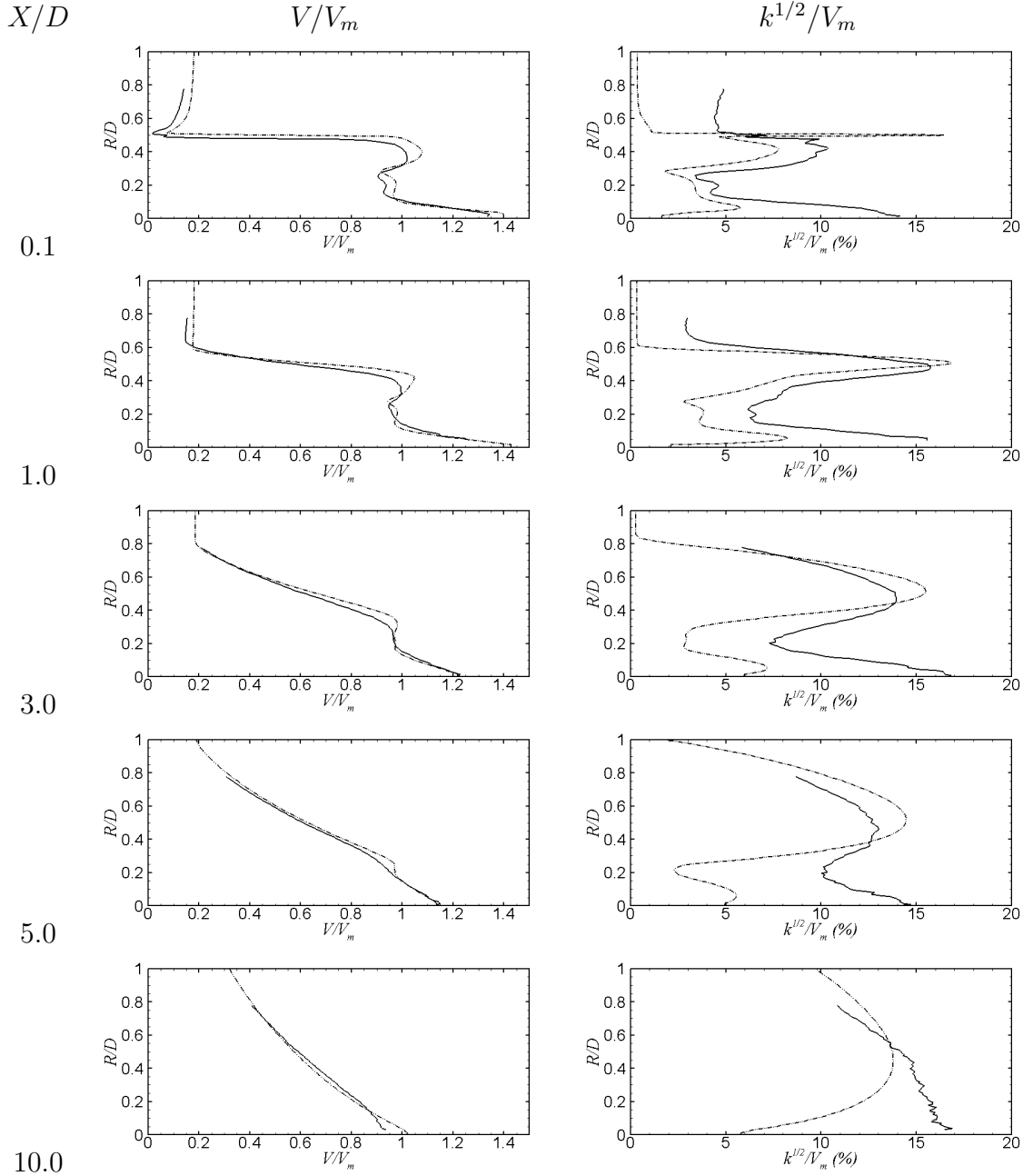


Figure 2.32. Comparison of the CFD and PIV azimuthally averaged profiles of mean streamwise velocity and turbulence intensity at various axial locations in the jet plume for the 12UH mixer; solid line, PIV data; dash-dot line, CFD data.

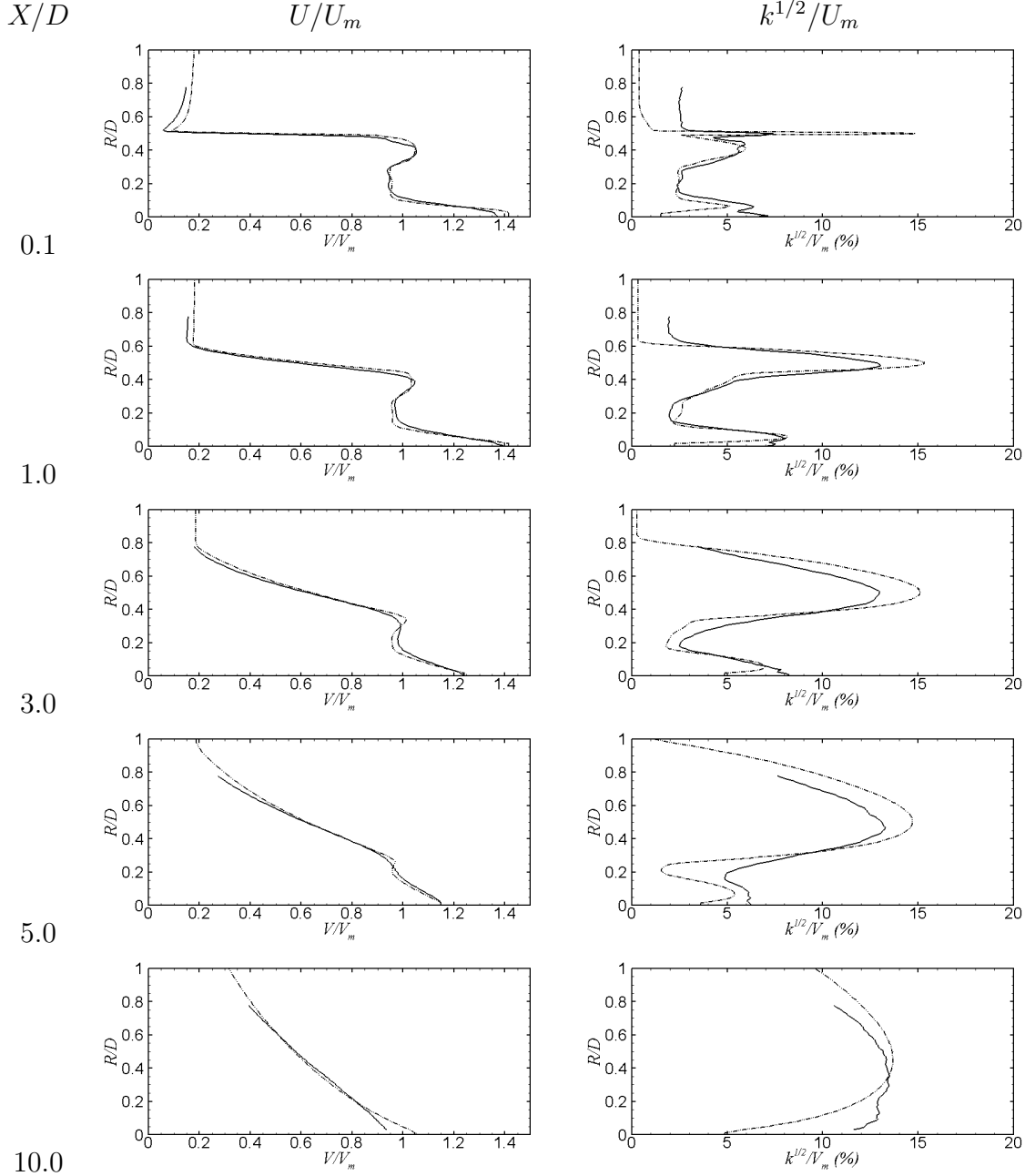


Figure 2.33. Comparison of the CFD and PIV azimuthally averaged profiles of mean streamwise velocity and turbulence intensity at various axial locations in the jet plume for the 20UH mixer; solid line, PIV data; dash-dot line, CFD data.

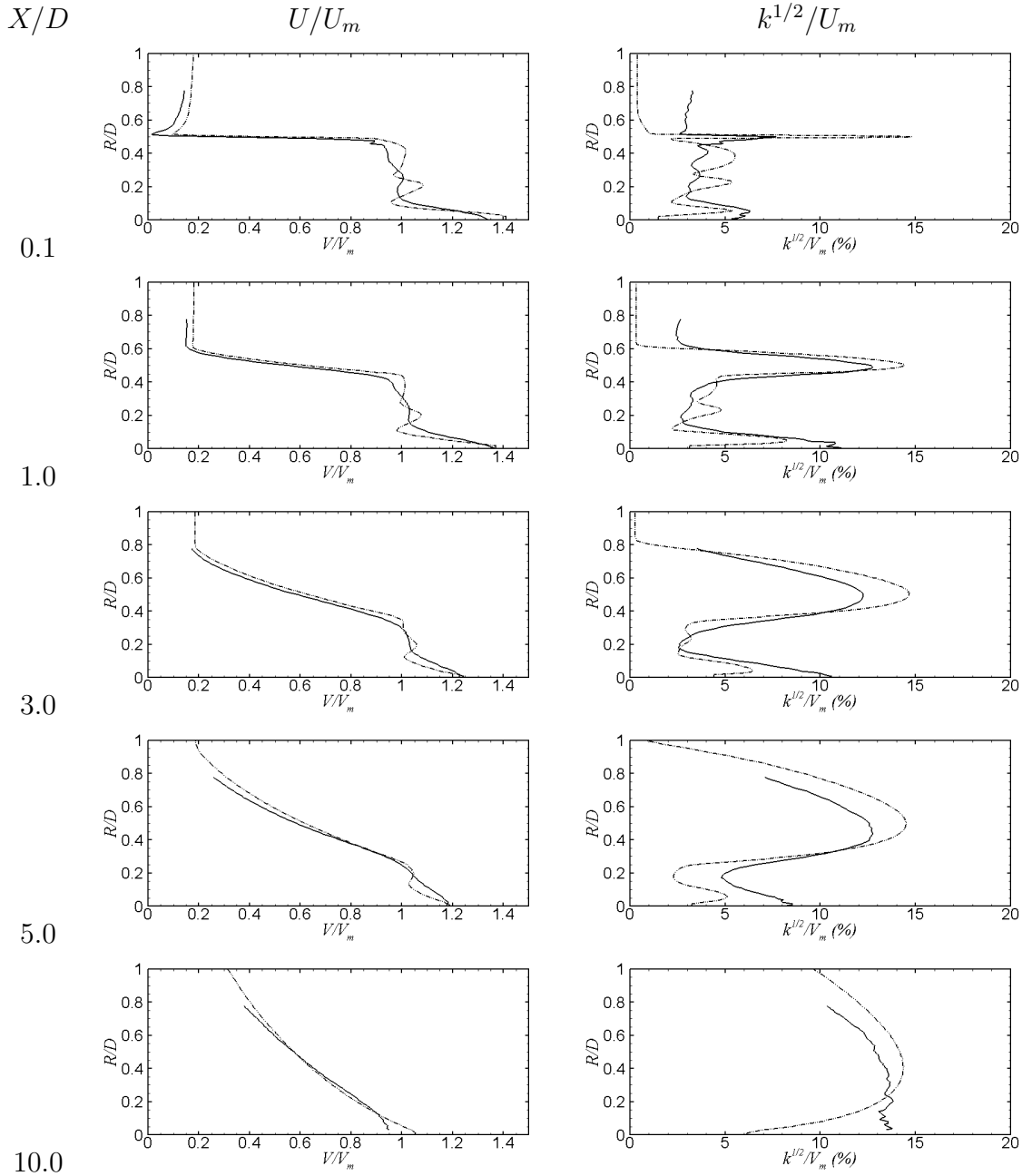


Figure 2.34. Comparison of the CFD and PIV azimuthally averaged profiles of mean streamwise velocity and turbulence intensity at various axial locations in the jet plume for the 20DH mixer; solid line, PIV data; dash-dot line, CFD data.

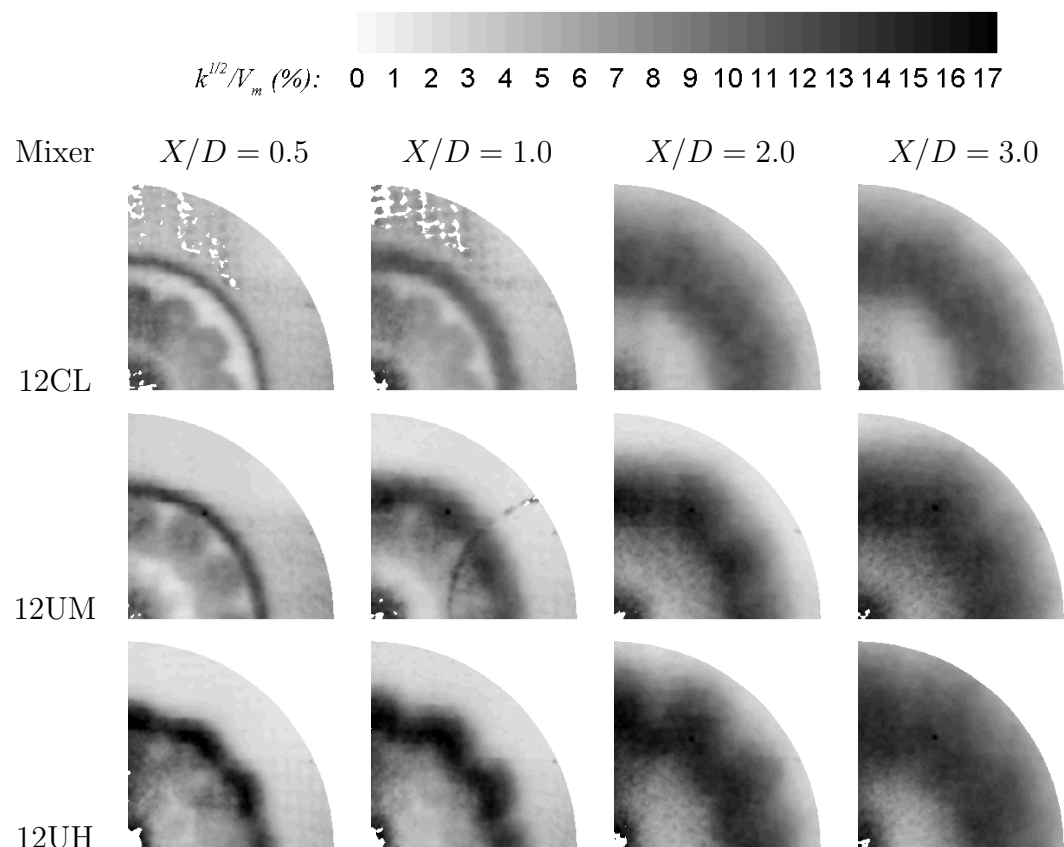


Figure 2.35. Comparison of the PIV turbulence intensities in the jet plume for the 12-lobed mixers at set point 312.

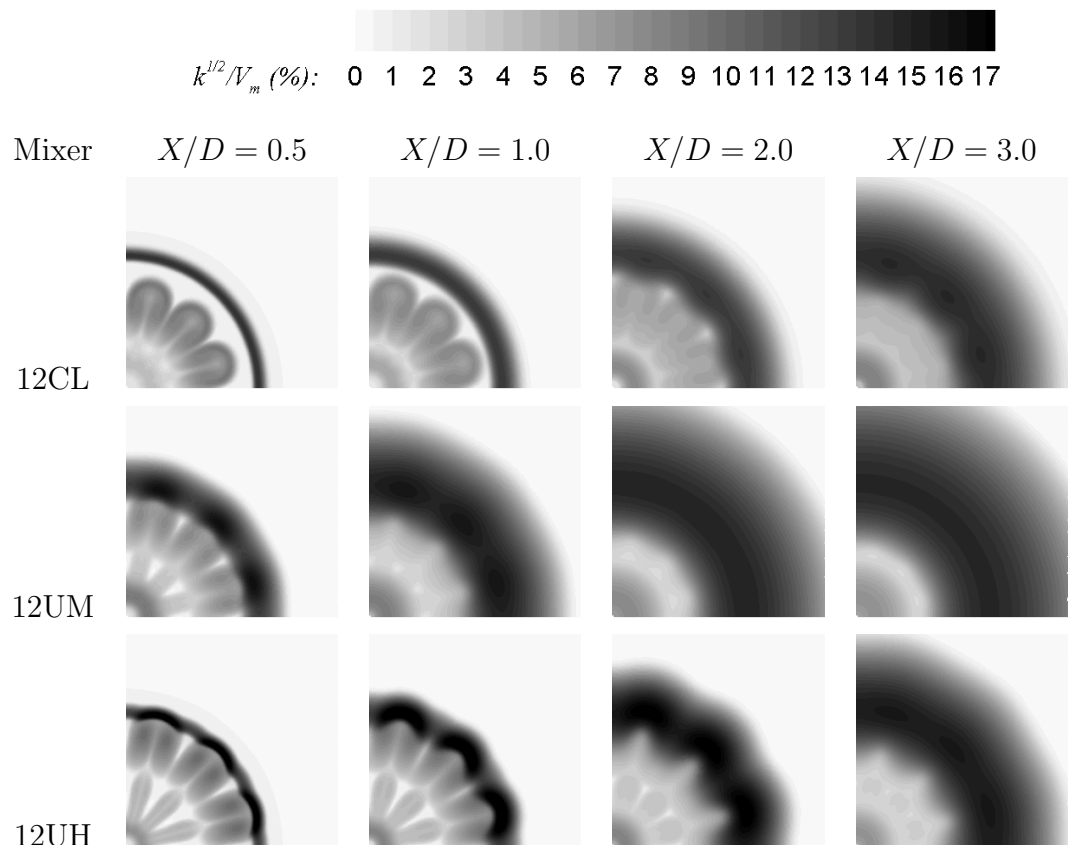


Figure 2.36. Comparison of the CFD turbulence intensities in the jet plume for the 12-lobed mixers at set point 312.

3. Two-Source Noise Model

3.1 Methodology

The initial investigation of using a two-source model for the prediction of the noise from jets with internal lobed mixers was performed as part a previous research effort [118–122]. The results from this previous research showed that the far-field Sound Pressure Level spectra of a jet with an internal forced mixer can be modeled by empirically fitting the sum of two modified single stream jet spectra. The initial motivation for this noise modeling approach was based on the success of the four-source noise model developed by Fisher *et al.* [39–41], which showed that the far-field noise from a coaxial jet could be modeled using sum of four modified single stream jet spectra.

The four-source method is based on the observation that in coaxial jets distinct regions can be identified which exhibit similarity relationships that are identical to those observed in simple single stream jets. Based on this fact, it is then proposed that the noise of a simple coaxial jet can be described as the combination of four noise producing regions each of whose contribution to the total far field noise levels is the same as that produced by a single stream jet with the appropriate characteristic velocity, temperature, and length scales. This approach allows existing experimental databases of single stream jet noise spectra to be used as a foundation for determining the noise from a coaxial jet. For coaxial jets the four noise source regions are the secondary-ambient shear layer, the primary-secondary shear layer, the interaction region where the secondary-ambient shear layer and primary-secondary shear layer merge, and finally the fully mixed flow region.

Following a similar approach as the four-source method, the previous research work on semi-empirical noise models led to the development of a two-source model

formulation for forced mixer applications [118–121]. This formulation, which was based on both observations of the changes in the forced mixer experimental noise data and the aerodynamic structure of the forced mixer jet plumes, uses the sum of two modified single stream jet noise spectra. It was observed that the velocities of the flow exiting the nozzle of a jet with an internal forced mixer were often close to the fully mixed jet velocity scale. In addition, it was observed that the forced mixers produce turbulent streamwise vortices which eventually impact the main jet shear layer causing a local enhancement of the turbulence intensity. The enhancement of the shear layer turbulence intensity increases as the lobe mixer penetration height increases. It is therefore proposed that the increase in high frequency noise that occurs in jets with forced mixers is due to the enhanced turbulence levels that are produced in the jet plume from the interaction of the main jet shear layer and the turbulent streamwise vortices. A schematic of the general structure of the turbulent region in a coaxial jet plume with an internal forced mixer is shown in Figure 3.1.

In the two-source model approach, the low frequency region of the noise spectrum is modeled using a reduced, filtered, fully mixed jet, given as

$$SPL_D(\theta, f) = SPL(V_m, T_m, D_m, \theta, f) + 10 \log_{10}(F_D(f_m, f)) + 40 \log_{10}(\Gamma_D), \quad (3.1)$$

where SPL_D refers to the noise from the downstream fully mixed jet source and SPL refers to a single jet prediction using the fully mixed jet velocity, V_m , temperature, T_m , and diameter, D_m . The low-pass filter, F_D , is applied to the spectrum to remove the high frequency portion, which corresponds to sources predominately located in the upstream portion of the fully mixed single stream jet. This low-pass filter, which is formulated by Fisher *et al.* [39] based on source location data of single stream jets, is defined as

$$F_D = \exp\left(-4\frac{f}{f_m}\right) \left[1 + \left(4\frac{f}{f_m}\right) + \frac{1}{2}\left(4\frac{f}{f_m}\right)^2 + \frac{1}{6}\left(4\frac{f}{f_m}\right)^3\right], \quad (3.2)$$

where f_m is the filter cut-off frequency. Physically, Equation 3.2 represents the amount of sound energy that is radiated from sources downstream of the potential

core. The cut-off frequency corresponds to the location where the term $10 \log_{10}(F_D)$ is equal to -3 dB. As a result, the total noise at the cut-off frequency is the sum of equal parts of both the upstream and downstream sources. The source reduction term, $40 \log_{10}(\Gamma_D)$, shifts the fully mixed jet noise spectra down. This term is a function of the ratio of turbulence intensities, Γ_D , defined as,

$$\Gamma_D = \frac{\alpha_D}{\alpha_o}, \quad (3.3)$$

where α_D is peak turbulence intensity in the downstream portion of the actual jet plume and α_o is the peak turbulence intensity in the plume of a single stream jet. In this study the turbulence intensity is defined as

$$\alpha = \frac{k^{1/2}}{V_J}, \quad (3.4)$$

where k is the turbulence kinetic energy and V_J is the characteristic jet velocity.

The downstream filter function F_D and the corresponding spectral attenuation, $10 \log_{10}(F_D)$, are plotted in Figures 3.2 and 3.3, respectively for a sample cut-off frequency of 1000 Hz. It is seen from Figure 3.2 that the downstream source filter function has a value of 1 for frequencies less than the cut-off frequency and a value of 0 for frequencies above the cut-off frequency. As a result, it is seen in Figure 3.3 that this filter eliminates the high frequency portion of the spectrum.

The high frequency portion of forced mixer noise spectrum is modeled as an enhanced, filtered, fully mixed jet, given as

$$SPL_U(\theta, f) = SPL(V_m, T_m, D_m, \theta, f) + 10 \log_{10}(F_U(f_m, f)) + 40 \log_{10}(\Gamma_U), \quad (3.5)$$

where SPL_U refers to the noise from the upstream fully mixed jet source and SPL refers to a single jet prediction using the fully mixed jet velocity, V_m , temperature, T_m , and diameter, D_m . The high-pass spectral filter, F_U , removes the low frequency part of the single jet noise prediction, which corresponds to sources that are predominately located in the downstream region of the jet plume. The form of this filter is given as,

$$F_U = 1 - F_D, \quad (3.6)$$

where F_D is the downstream filter function given in Equation 3.2. Physically, Equation 3.6 represents the amount of sound energy that is radiated from sources upstream of the potential core. The upstream filter function, F_U , and the corresponding spectral attenuation are plotted in Figures 3.2 and 3.3, respectively for a sample cut-off frequency of 1000 Hz. The source augmentation term, $40 \log_{10}(\Gamma_U)$, shifts the fully mixed jet noise spectra up. This term is a function of the ratio of peak turbulence intensities, Γ_U , defined as,

$$\Gamma_U = \frac{\alpha_U}{\alpha_o}, \quad (3.7)$$

where α_U is the peak turbulence intensity in the upstream portion of the actual jet plume.

For simplicity, it is assumed that the cut-off Strouhal numbers of the upstream and downstream sources are equal. In practice, the cut-off frequency is replaced by a cut-off Strouhal number, which is defined as

$$St_m = f_m \frac{D_m}{V_m}, \quad (3.8)$$

where V_m is the fully mixed jet velocity and D_m is the fully mixed jet diameter.

The fully mixed jet properties are calculated using the ideal primary and secondary flow velocities, temperatures, and areas along with conservation of mass, momentum, and energy. Specifically, the fully mixed velocity, temperature and diameter are calculated as,

$$V_m = V_p \left(\frac{1 + \lambda^2 \beta \delta}{1 + \lambda \beta \delta} \right) \quad (3.9)$$

$$T_m = T_p \frac{1 + \lambda \beta}{(1 + \lambda \beta \delta)} \quad (3.10)$$

$$D_m = D_p \left(\frac{(1 + \lambda \beta)(1 + \lambda \beta \delta)}{1 + \lambda^2 \beta \delta} \right)^{\frac{1}{2}} \quad (3.11)$$

where V_p and T_p are the ideal primary flow fully expanded velocity and temperature, D_p is the primary flow diameter and λ , β , and δ are the secondary to primary flow ratios of velocity, area, and density, respectively. The ideal fully expanded flow properties are determined using the assumption that the flow in each stream isentropically expands from the total pressure to the ambient pressure.

In the present two-source model formulation there are three model parameters: the cut-off Strouhal number used to define the spectral filters (St_m), and the two single jet source strength values (Γ_U and Γ_D). In the previous research effort these three parameters were empirically determined by fitting the model to the experimental acoustic data. As part of the previous work the fully mixed jet conditions were used in the downstream single stream jet prediction, and both secondary jet and fully mixed jet conditions were tested for the upstream single jet prediction. Based on further review of the experimental PIV data and the CFD results from the current research effort, it is seen that the fully mixed jet conditions are more consistent with the flow field in the upstream region of the jet plume for most of the lobe mixer configurations. As a result, only the previous two-source model analysis using mixed jet conditions for the upstream region will be considered here.

As part of the previous research effort [118], the two-source model parameters were empirically determined by minimizing the error between the model predictions and the experimental data. This process was performed numerically using a non-linear least squares optimization routine which minimized the weighted error in the far field Sound Pressure Level spectra between the model prediction and the experimental data at all observer angles. The results from the two-source model optimization process using the ARP876C single jet database are given in Table 3.1 for the various mixer geometries. In addition, similar results using the ESDU single jet database are given in Table 3.2.

In the present work, the empirically derived noise model parameters are replaced with CFD-based parameters. Details concerning the process used to determine the CFD-based noise model parameters along with a summary of the CFD-based two-source noise model performance is discussed in the following sections.

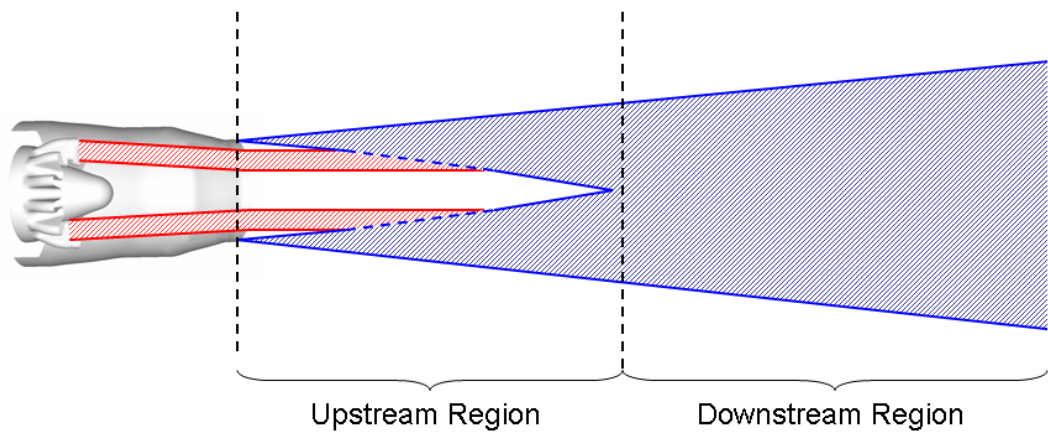


Figure 3.1. Structure of a jet plume with an internal forced mixer.

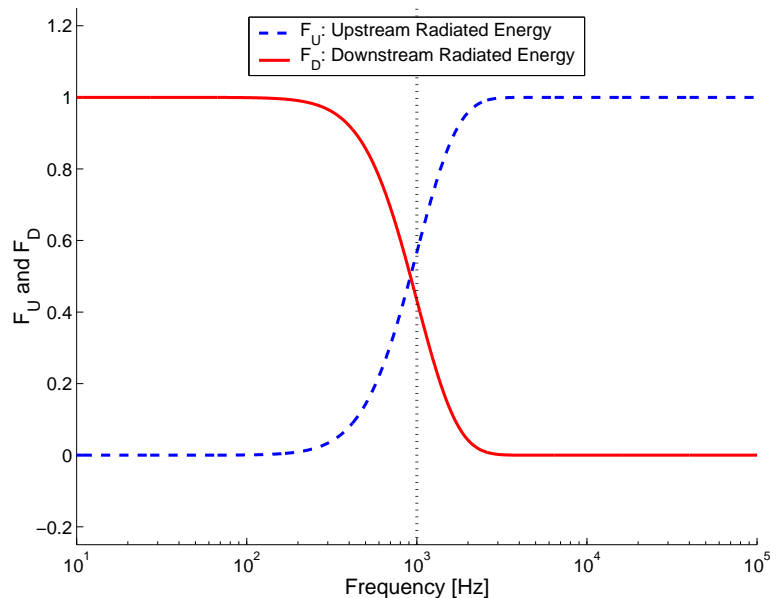


Figure 3.2. F_U and F_D functions for $f_c = 1000$ Hz

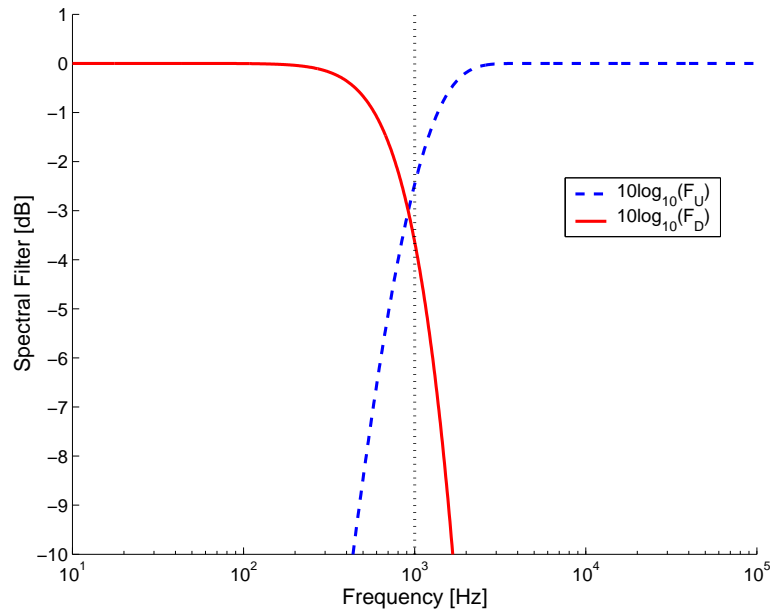


Figure 3.3. Spectral filter functions for $f_c = 1000$ Hz

Table 3.1 Two-source model empirically derived parameters using the ARP876C single jet prediction method for set point 110.

Mixer	St_m	Γ_U	Γ_D
12CL	3.46	1.16	0.99
12UM	2.70	1.33	0.95
12UH	3.47	1.45	0.88
20UH	3.42	1.31	0.94
20DH	5.41	1.25	0.94

Table 3.2 Two-source model empirically derived parameters using the ESDU single jet prediction method for set point 110.

Mixer	St_m	Γ_U	Γ_D
12CL	3.46	1.10	1.04
12UM	2.70	1.33	0.99
12UH	2.75	1.39	0.92
20UH	3.42	1.28	0.99
20DH	5.41	1.19	0.99

3.2 CFD-Based Noise Model Parameters

Based on the analysis of the empirically derived two-source noise model parameters given in Table 3.1 and 3.2 it is seen that the variation in the downstream source strength parameter is relatively small. As a result, as a first approximation it is assumed that the downstream source strength term, Γ_D , has a value of 1.0. This approximation essentially assumes that the turbulence in the downstream region of the forced mixer jet plume is identically to that of a standard single stream jet. In addition, it is seen that the variation in the cut-off Strouhal is relatively small compared to the full range of Strouhal numbers in the noise spectrum, which span from 0.1 to 50. Consequently, this parameter is held to a constant value of 3.5 for all of the mixer geometries. The only remaining noise model parameter is the upstream enhancement level, Γ_U . This final model parameter is related to the peak turbulence levels in the upstream portion of the jet plume, following the assumption that the excess high frequency noise is caused by enhanced turbulence levels in the jet plume. Specifically the upstream source strength is calculated with Equation 3.7 using the peak turbulence intensities from a CFD prediction of the plume flow field. The axial variation of the peak turbulence intensities in plumes of all five forced mixers at set point 110 is shown in Figure 3.4. In addition, in Figure 3.4 turbulence intensities from a single stream jet are also plotted. For each mixer, the upstream enhancement level, Γ_U , is calculated using the peak values of the turbulence intensities shown in Figure 3.4. The upstream source enhancement levels are calculated using the CFD predicted single stream jet turbulence intensity of 16.4%. The resulting CFD-based noise model parameters are given in Table 3.3.

It is seen from the values in Table 3.3 that the CFD-based upstream source enhancement levels are less than the empirically derived enhancement levels. At first appearance this result is a bit perplexing considering the fact that the CFD analysis generally over-predicts the peak turbulence intensities in the jet plume. There are a number of possible reasons for this discrepancy. First, it is important

to note that the CFD-based upstream enhancement levels are calculated using the CFD predicted single jet peak turbulence intensity. After further analysis of the CFD and PIV data it appears that even though the WIND analysis over-predicts the nominal turbulence levels in the main jet shear layers, it is under-predicting the enhancement levels that result from the interaction of the turbulence in the main jet shear layer and the turbulence in the streamwise vortices. Quantifying the under-prediction of the enhanced turbulence levels is complicated by the fact that experimental PIV data was only acquired at set point 312, the high power set point with a Mach 0.2 flight stream. It has been observed by Tester and Fisher [122] that the empirically-derived upstream enhancement levels are effected by the presence of a flight stream. Moreover, additional high frequency noise sources related to shock-turbulence interactions are present at the high power set point [99]. Consequently, a direct comparison of the PIV data of the turbulence levels in the jet and the two-source noise model parameters can not be made.

Despite the previously mentioned difficulties, an attempt has been made to assess the amount of under-prediction of the enhanced turbulence levels in the CFD analysis. In particular, the ratio is taken of the peak turbulence intensities in the PIV data of the lobed mixer cases to the peak turbulence intensity in the PIV data of a simulated single stream jet (confluent mixer, set point 5000). This ratio represents the how the turbulence levels in the lobed mixers cases are enhanced as a result of the interaction of the turbulent streamwise vortices. For the PIV data the peak turbulence intensity in the simulated single jet had a value of 15.5%. A similar calculation is performed using the CFD data. In this calculation, the peak turbulence intensities in the CFD data of the lobed mixer cases are normalized by the peak turbulence intensities in the CFD data of a simulated single stream jet (confluent mixer, set point 5000). For the CFD data the peak turbulence intensity of the single stream jet case had a value of 16.4%. The results of these calculations using azimuthally averaged data is shown in Figure 3.5 for the 12UM and 12UH mixers. In this figure it is seen that the CFD analysis at set point 312 does in fact

under-predict the interaction of the turbulence in the main jet shear layer and the turbulent streamwise vortices. It is noted that the evaluation of peak turbulence levels in the PIV data is a bit perilous since it is quite possible that the peak value could be an erroneous data point. In this analysis it is hoped that this occurrence was avoided by only selecting points with a quality parameter that is greater than 0.9.

A second possible reason for the discrepancy in the CFD-based and empirically derived enhancement levels could result from inconsistencies in the two-source model assumptions. In particular, it is assumed in the two-source model formulation that the fully mixed jet velocity is the representative velocity scale driving the main jet shear layer over the entire upstream region. It is observed in the CFD and PIV data that this assumption is not strictly true for all mixer configurations. In particular, for the 12CL mixer the flow is not completely mixed at the nozzle exit, where flow velocities range from the bypass velocity scale up to the core velocity scale. This issue is addressed in the formulation of the multi-source model, which discussed in the following Chapter.

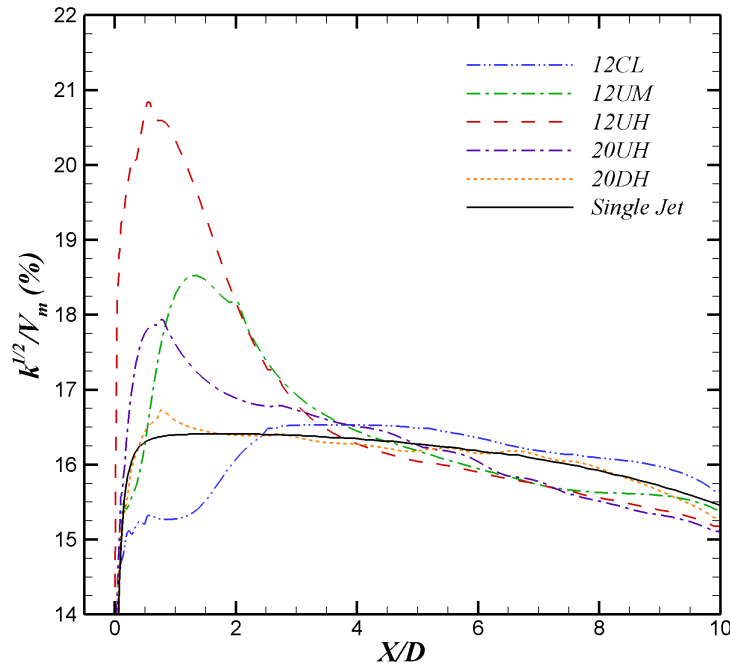


Figure 3.4. Axial variation of the peak turbulence intensities in the jet plume.

Table 3.3 CFD-based two-source model parameters for set point 110.

Mixer	St_m	Γ_U	Γ_D
12CL	3.50	1.04	1.00
12UM	3.50	1.13	1.00
12UH	3.50	1.27	1.00
20UH	3.50	1.09	1.00
20DH	3.50	1.02	1.00

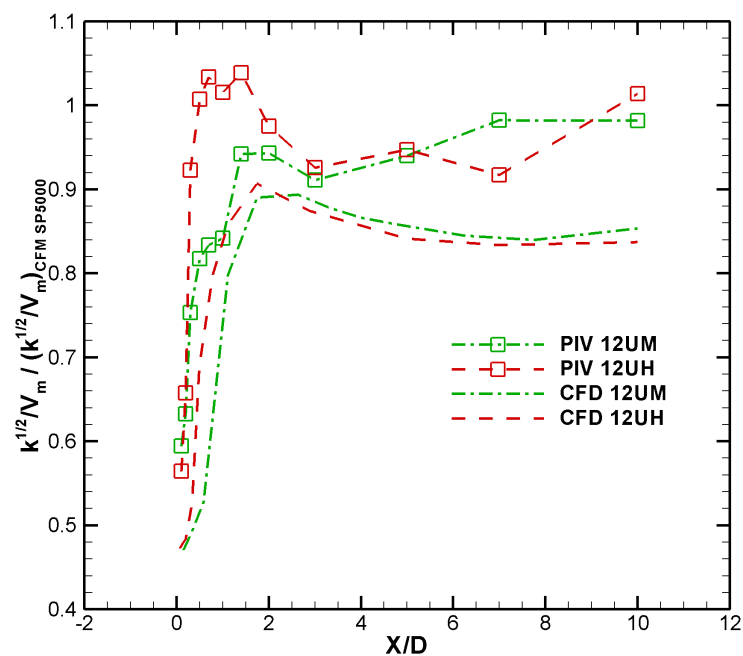


Figure 3.5. CFD and PIV estimated usptream turbulence enhancement for set point 312.

3.3 Model Performance

In Figures 3.6 to 3.10 two-source model noise predictions for various mixer designs are compared to the experimental acoustic data. In these figures the CFD-based two-source model predictions are plotted along with the contributions from each of the two sources. In addition, for reference the two-source model results using the optimized empirical model parameters are also shown.

The performance of the CFD-based two-source model for the 12CL mixer at set point 110 is compared to both the experimental acoustic data and a two-source model prediction using the empirical model parameters in Figure 3.6. It is seen in this figure that the CFD-based two-source noise prediction is in good agreement with the experimental data at all three far field observer angles.

The performance of the CFD-based two-source model for the 12UM mixer at set point 110 is compared to both the experimental acoustic data and a two-source model prediction using the empirical model parameters in Figure 3.7. In this figure the under-prediction of the CFD-based enhancement levels are clearly seen by the differences in the high frequency portion of the spectra at all three observer angles. The under-prediction of the CFD-based enhancement levels result in an under-prediction of the high frequency noise by approximately 2.8 dB.

The performance of the CFD-based two-source model for the 12UH mixer at set point 110 is compared to both the experimental acoustic data and a two-source model prediction using the empirical model parameters in Figure 3.8. Here it is seen that the CFD-based two-source model parameters result in an under-prediction in the high frequency region of approximately 1.5 dB. Furthermore, the effects of using a downstream enhancement level of 1.0 are most readily apparent in the noise predictions of the 12UH mixer, which show a 1.5 dB over-prediction in the low frequency portion of the spectrum.

The performance of the CFD-based two-source model for the 20UH mixer at set point 110 is compared to both the experimental acoustic data and a two-source

model prediction using the empirical model parameters in Figure 3.9. In this figure it is observed that the CFD-based two-source model predictions result in an under-prediction in the high frequencies by approximately 2.8 dB.

The performance of the CFD-based two-source model for the 20DH mixer at set point 110 is compared to both the experimental acoustic data and a two-source model prediction using the empirical model parameters in Figure 3.10. Here it is again seen that the CFD-based two-source model predictions result in an under-prediction of the high frequencies by approximately 2.7 dB.

In all of the CFD-based two-source model predictions the high frequency region is slightly under-predicted. However, it is noted that the trends in the enhancement levels for the various mixer geometries is well predicted by the CFD analysis, with the exception of the scalloped mixer (20DH). For this configuration the CFD-based upstream enhancement level was slightly lower than the 12CL mixer. The empirical model parameters suggest that the 20DH enhancement level should fall between the values for the 12CL and 20UH mixers. At this point it is worth noting that the scalloped mixer (20DH) was also the only configuration that did not exhibit excellent agreement in the CFD predicted mean velocities in the jet plume.

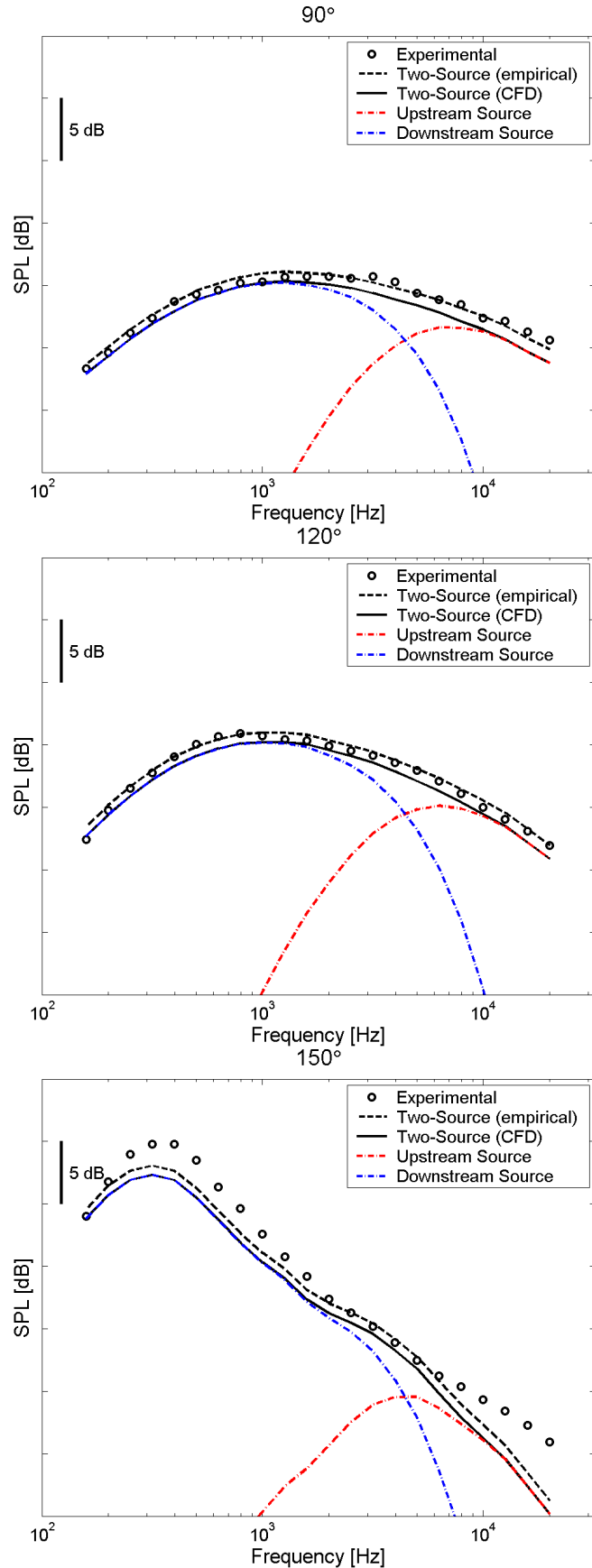


Figure 3.6. Two-source model noise predictions for the 12CL mixer at set point 110.

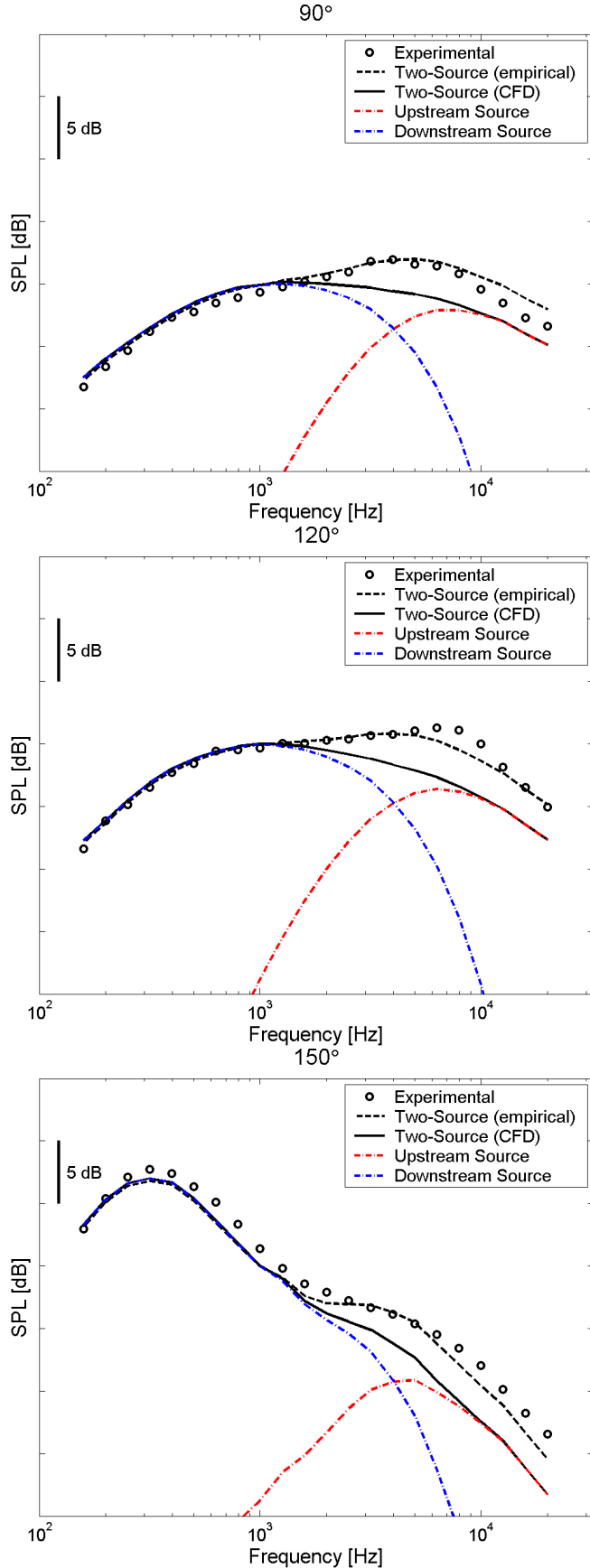


Figure 3.7. Two-source model noise predictions for the 12UM mixer at set point 110.

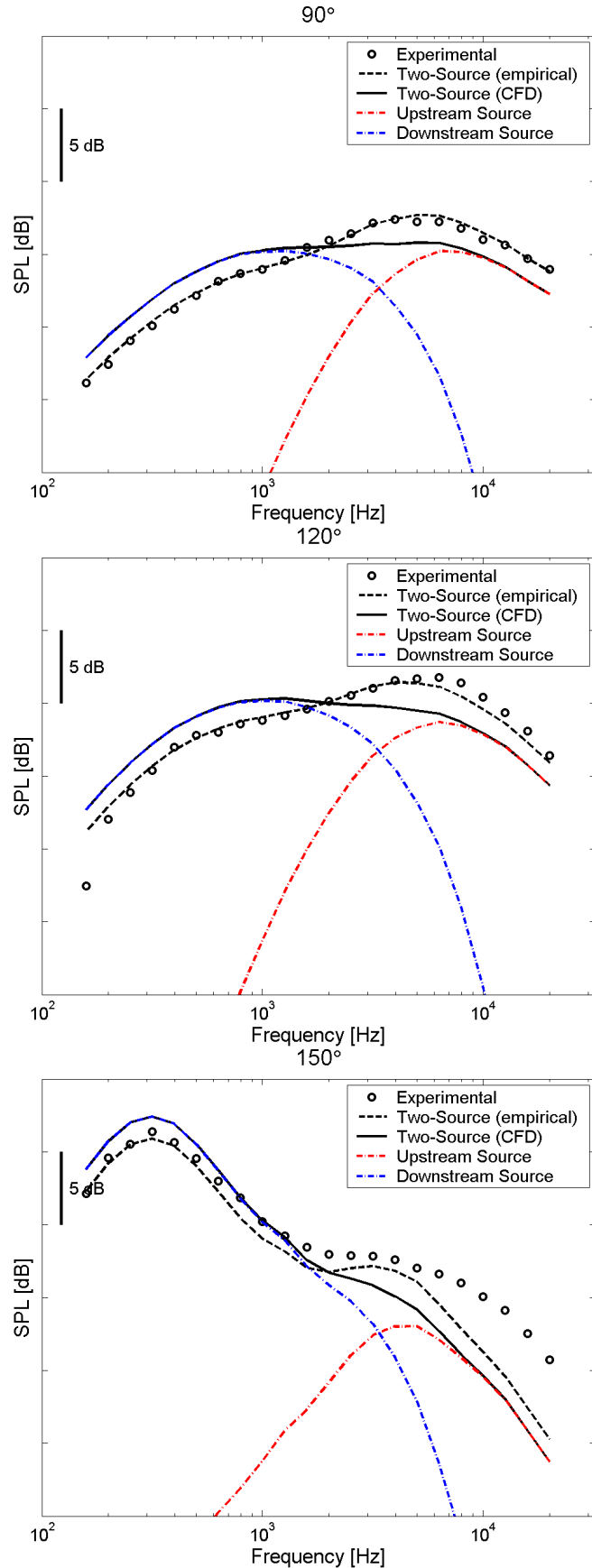


Figure 3.8. Two-source model noise predictions for the 12UH mixer at set point 110.

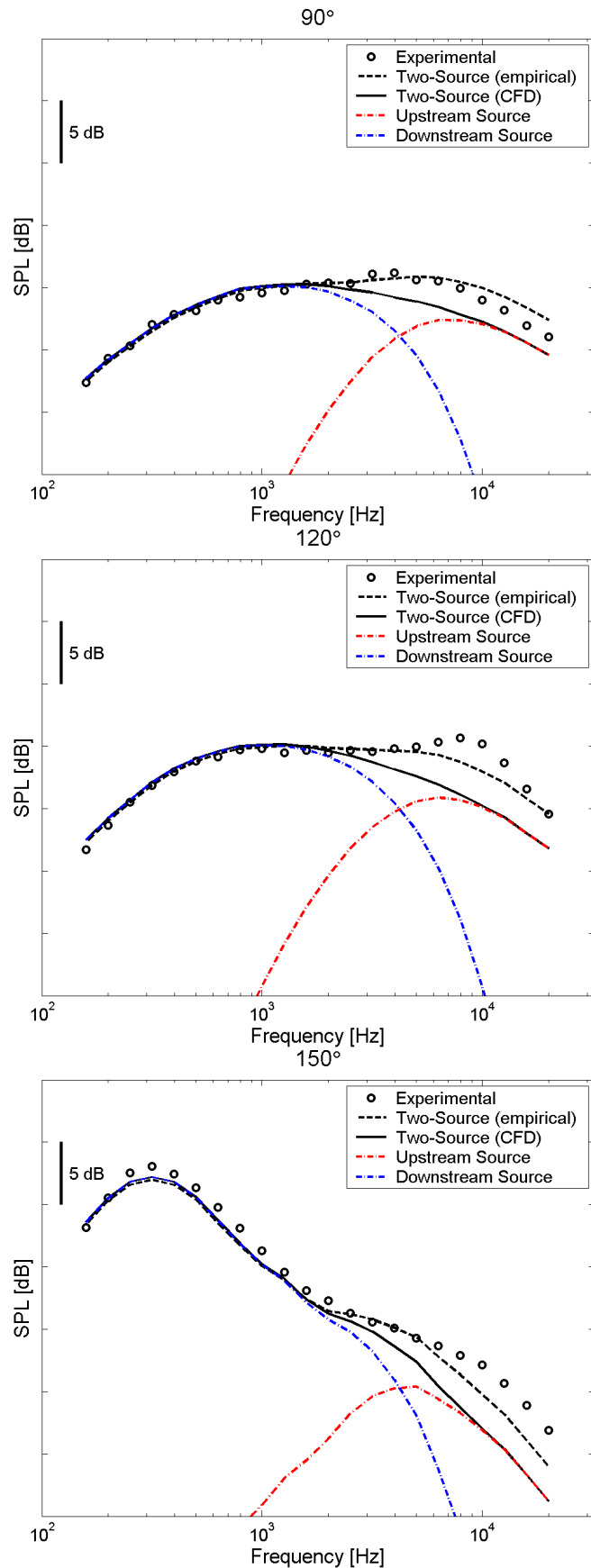


Figure 3.9. Two-source model noise predictions for the 20UH mixer at set point 110.

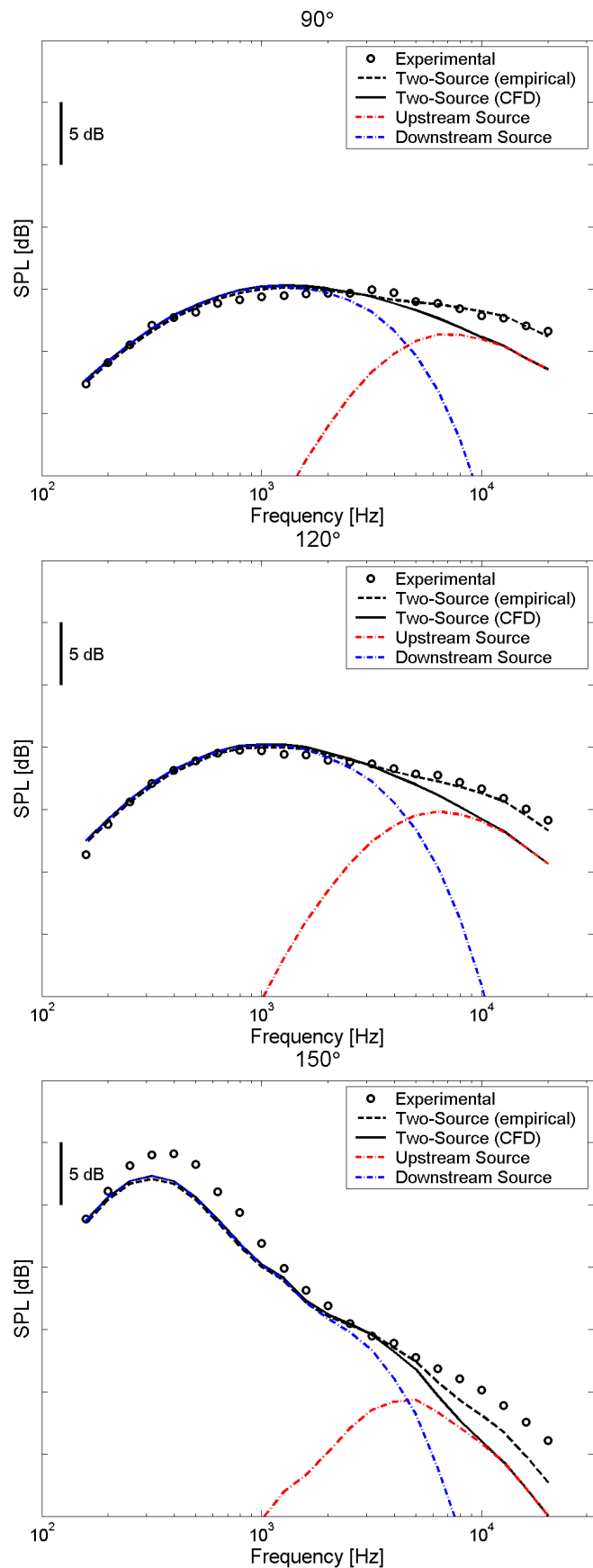


Figure 3.10. Two-source model noise predictions for the 20DH mixer at set point 110.

4. Multi-Source Noise Model

4.1 Methodology

The basic formulation of the multi-source noise model is similar to the two-source model. However, the multi-source model has two primary differences. First, the characteristic jet velocity and temperature for the upstream sections are determined directly from a RANS calculation. Second, the upstream portion of the jet plume is divided into a small number of additional sections, as shown in Figure 4.1. The impact of these two modifications are tested independently in sections 4.3 and 4.4.

In the multi-source model formulation the noise from the downstream region is modeled in the same fashion as the two-source model using Equation 3.1. However, in the multi-source model the noise from each of the upstream sections, SPL_i , is modeled as

$$SPL_i(\theta, f) = SPL(V_i, T_i, D, \theta, f) + 10 \log_{10} F_i(X_1, X_2, f) + 40 \log 10 (\Gamma_i), \quad (4.1)$$

where V_i , and T_i are the characteristic jet properties in a given section, Γ_i is the single jet enhancement level based on the peak turbulence intensities in a given section, and F_i is the filter function for a given section of the jet plume between the axial locations X_1 and X_2 .

The filter functions for the upstream sections are defined based on the source distribution work of Fisher *et al.* [123] and Tester and Fisher [124]. This source distribution information was used by Fisher *et al.* [39] in the development of the original Four-Source model spectral filters. The results of the source distribution work show that the source strength per unit length along a jet ($S(X)$) may be described as

$$S(X) = X^{m-1} \exp\left(\frac{-mX}{X_c}\right), \quad (4.2)$$

where m is the shape parameter and X_c is the centroid of the distribution, which is a function of frequency. A value of 4 is typically used for the shape parameter. To determine the exact dependence of the centroid location, X_c , with frequency it is assumed that for a given Strouhal number the centroid location scales as

$$X_c \sim \frac{1}{St}. \quad (4.3)$$

In addition, it is assumed that a Strouhal number of one is associated with the location of the end of the potential core, X_{PC} . These assumptions are supported by recent phased array source location experiments performed at the NASA Glenn Research Center by Lee *et al.* [125, 126]. Typical source distributions are shown in Figure 4.2 for a range of sample Strouhal numbers.

The fraction of the energy radiated from a specified region of the jet between positions X_1 and X_2 is given as

$$F_i = \frac{\int_{X_1}^{X_2} S(X) dX}{\int_0^{\infty} S(X) dX}. \quad (4.4)$$

Equation 4.4 is used to calculate the spectral contributions from each section of the jet plume. In this process each 1/3 octave band center frequency is converted to a Strouhal number using the fully mixed jet velocity and diameter. Using these Strouhal numbers, the source distribution centroid location for each frequency is then calculated as

$$X_c = \frac{X_{PC}}{St}, \quad (4.5)$$

which then defines the shape of the source distribution. For each frequency, the corresponding source distribution is integrated over each section of the jet plume to determine the total contributions from each section for a given frequency.

Formulating the spectral filters in the fashion ensures that the filters are conservative so that for a given 1/3 octave band the sum of the filter function values from all of the plume sections equals one. Examples of the filter function values for a sample case with 4 equally spaced upstream sections between the nozzle exit ($X/D = 0$)

and $X/D = 5$ are shown in Figures 4.3 and 4.4. For these sample plots the 1/3 octave band center frequencies are converted to Strouhal numbers based on a jet velocity of 280 m/s and a diameter of 0.2 m. These jet properties are representative of the set point 110 fully mixed jet conditions.

In the development of the multi-source model two modifications are applied to a standard two-source model formulation. First, the characteristic jet velocity and temperature for the upstream sections are determined directly from a RANS calculation. Second, the upstream portion of the jet plume is divided into a small number of additional sections. The effects of these modifications are tested independently. In section 4.3 the impact of using characteristic jet velocity and temperature scales determined from a RANS solution is investigated by using just one section in the upstream region. These noise predictions are compared to predictions using a standard two-source model, which uses the fully mixed velocity and temperature scales for the upstream region. In section 4.4 the results using the multi-source model formulation are presented where four sections are used to define the upstream region.

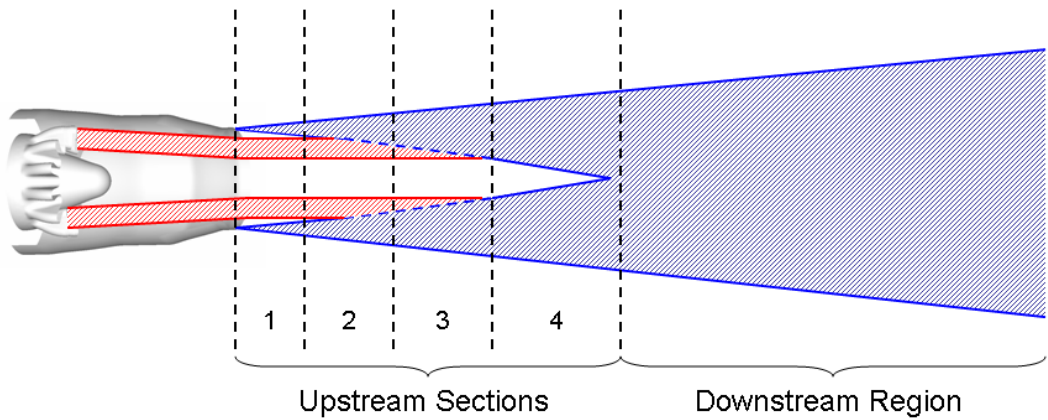


Figure 4.1. Structure of a jet plume with an internal forced mixer.

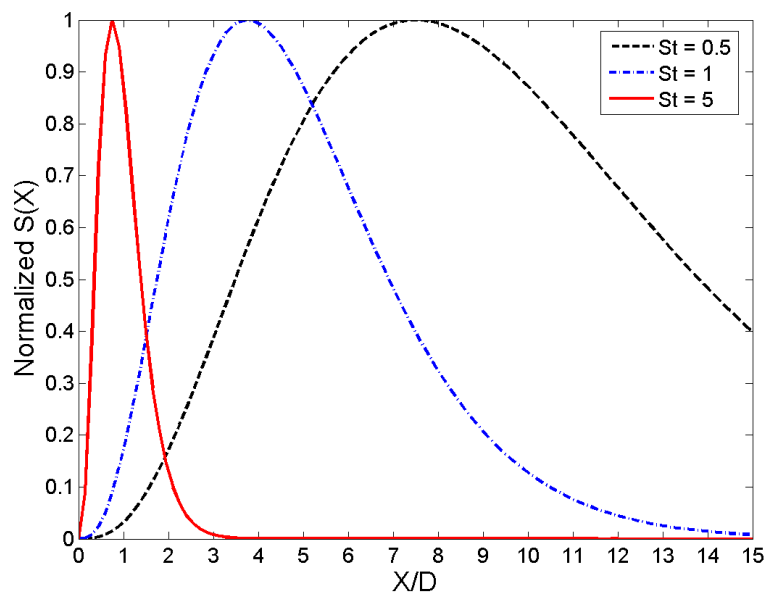


Figure 4.2. Sample source distribution functions for Strouhal numbers 0.5, 1, and 5.

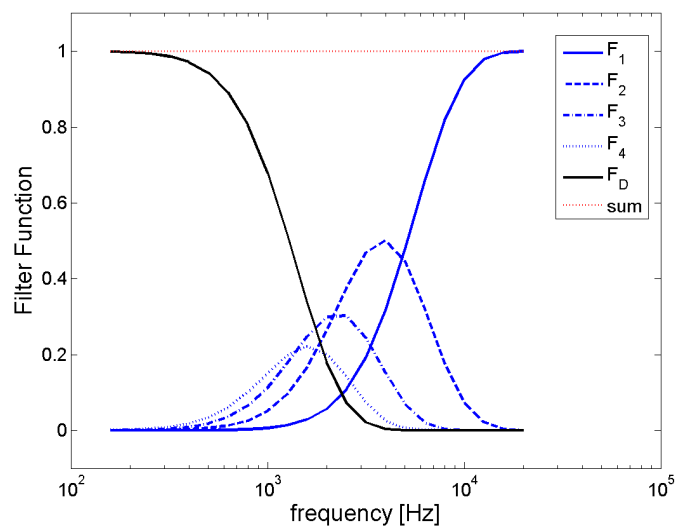


Figure 4.3. Sample spectral filter functions for the multi-source noise model.

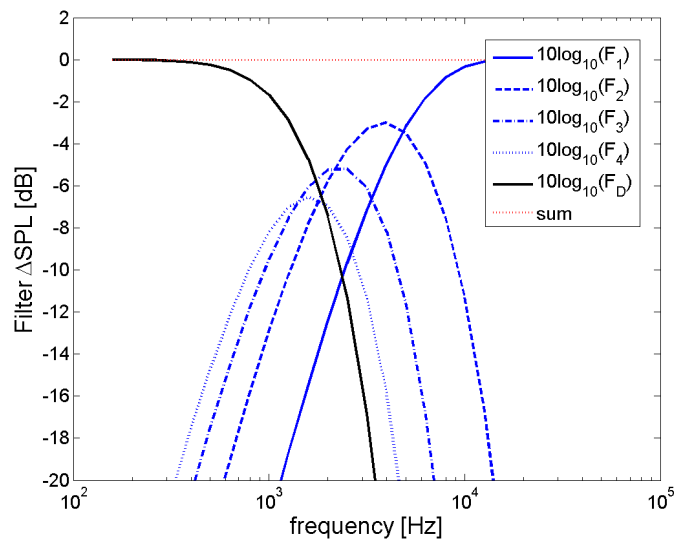


Figure 4.4. Sample spectral filter function attenuations for the multi-source noise model.

4.2 Model Parameters

In the multi-source model the CFD-based single stream jet characteristic properties in each section are determined by analyzing the mean velocity profiles in a RANS solution. In this process each radial grid line at a given axial location in the jet plume is analyzed to find the location of the inside edge of the main jet shear layer. In this study this location is numerically defined by finding the first radial point in the jet plume between the lip-line and the centerline where the mean velocity gradient ($\delta V_x / \delta R$) drops below a specified fraction of the velocity gradient at the lip-line ($R/D = 0.5$). This process is shown graphically in Figure 4.5 for an example threshold fraction of 0.25. Once the shear layer edge location is identified, the velocity and temperature values at this location are stored. In Figure 4.6 sample velocity profiles are shown for the 12CL mixer at four downstream locations. In this figure the locations of the inside edge of the shear layer are marked with a circle.

The axial variation of the shear layer inside edge location is shown in Figure 4.7 for the five lobed mixers and a reference single stream jet. Also plotted in Figure 4.7 is the line corresponding to a constant η value of -0.05. Here it is observed that for all of the cases the WIND analysis predicts a shear shear layer inside edge location that is generally consistent with an η value of -0.05. This result also shows the under-prediction of the mixing in the CFD analysis in the region upstream of the potential core, since experimental evidence typically shows this shear layer edge location to occur at approximately $\eta = -0.10$. The drop in the shear layer edge location for the 12CL mixer at approximately $X/D = 1.0$ represents the location where the streamwise vortices first interact with the shear layer. A similar drop occurs for the 12UM mixer at approximately $X/D = 0.25$. No such drop is observed for the 12UH mixer due to the fact that at the nozzle exit the vortex structure extends all the way to the nozzle wall. A second drop occurs in the shear layer edge location for all of the mixers further downstream at approximately $X/D = 6$. This drop represents the location where the numerical algorithm used to determine the

edge location begins to identify the centerline as the shear layer inside edge. This transition generally occurs shortly after the location of the end of the potential core of the unmixed primary flow. Downstream of this point the flow field begins to resemble that of a fully mixed flow, no longer showing any radial variations in the velocity field that were produced by the lobed mixers.

The axial variations of the shear layer inside edge velocity for the five lobed mixers are shown in Figure 4.8. In the multi-source model the upstream region of the jet is divided into a small number of sections based on the axial variation of these characteristic velocities. In this process spatial divisions are placed at locations where relatively sharp changes occur in the variation of the shear layer edge velocity.

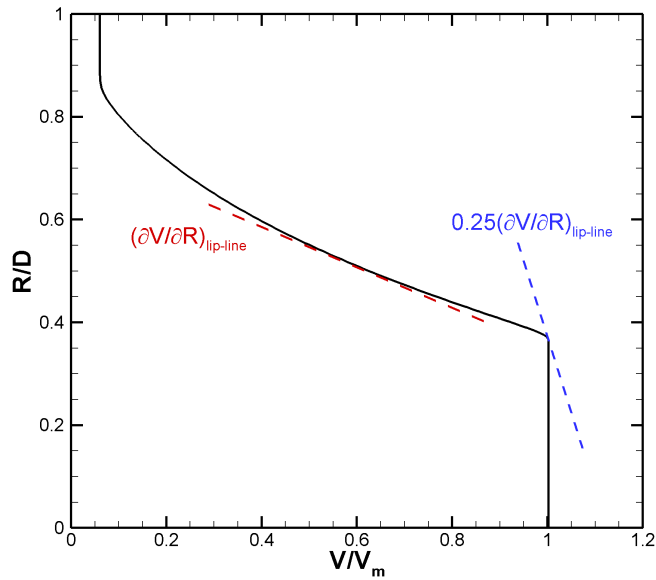


Figure 4.5. Schematic of the numerical estimation of the main jet shear layer inside edge location.

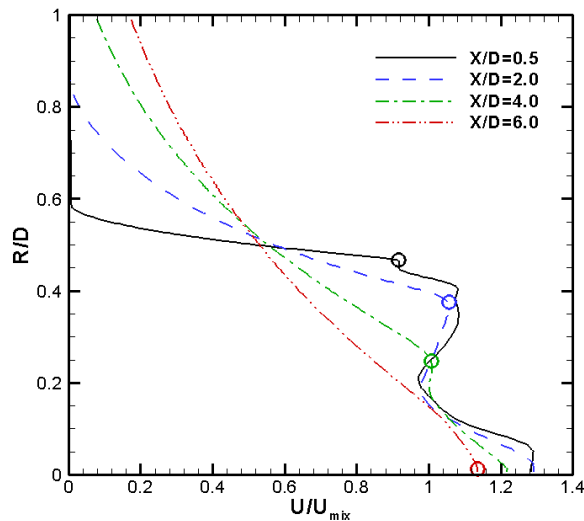


Figure 4.6. Sample velocity profiles for 12CL mixer; shear layer inside edge locations are marked with a circle.

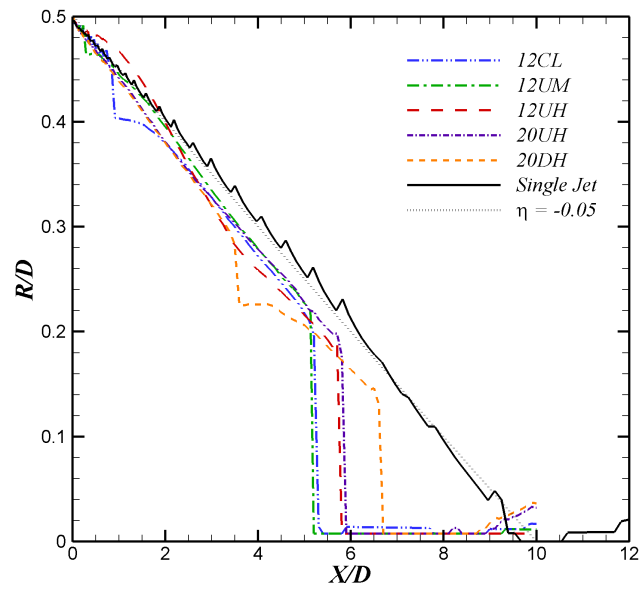


Figure 4.7. Axial variation of the main jet shear layer inside edge location.

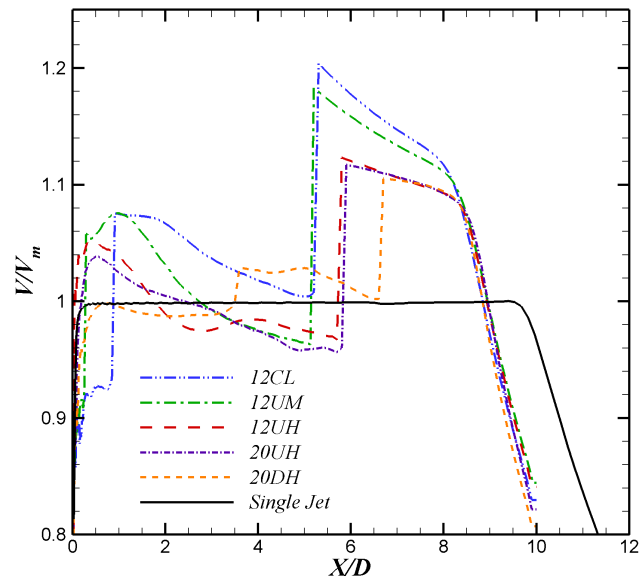


Figure 4.8. Axial variation of the characteristic jet velocity scale.

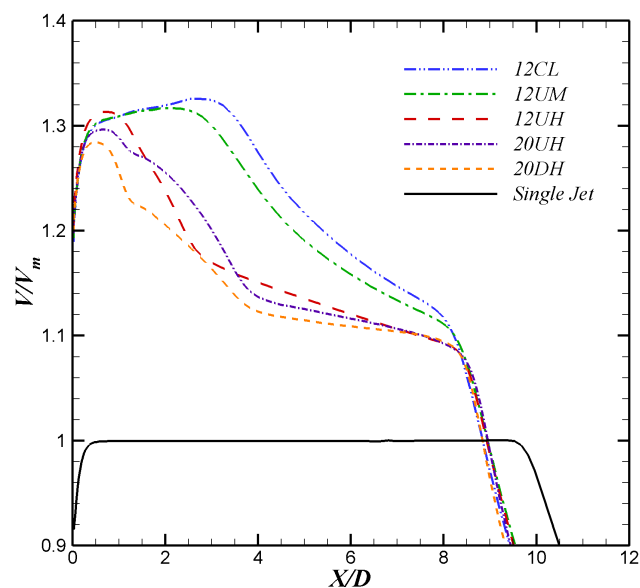


Figure 4.9. Axial variation of the centerline velocity.

4.3 Single Section Multi-Source Model Predictions

The impact of using characteristic jet velocity and temperature scales from the RANS analysis is first determined by applying the present formulation with just one section in the upstream region. The upstream region characteristic jet properties are determined by averaging the shear layer edge values between the nozzle exit and approximately 5 diameters downstream. The results from this process for each lobe mixer design are given in Table 4.1.

In Figures 4.10 to 4.14 the two-source noise predictions using the CFD-based characteristic jet properties for the upstream region are compared to the standard two-source model predictions, which use the fully mixed velocity and temperature for the upstream region. In both of these predictions the maximum turbulence intensity in the plume is used to calculate the upstream source enhancement level. It is seen in Figures 4.10 to 4.14 that the two-source model noise predictions using the CFD-based velocity and temperature scales are almost identical to the standard two-source model predictions. This result is expected since the CFD-based characteristic jet velocities for the upstream region are within 5% of the fully mixed velocity for all of the lobed mixer designs, as shown in Table 4.1.

Table 4.1 CFD-based upstream region characteristic jet properties.

Mixer	V/V_m	T/T_m
12CL	1.05	1.12
12UM	1.02	1.07
12UH	1.01	1.10
20UH	1.00	1.03
20DH	1.00	1.03

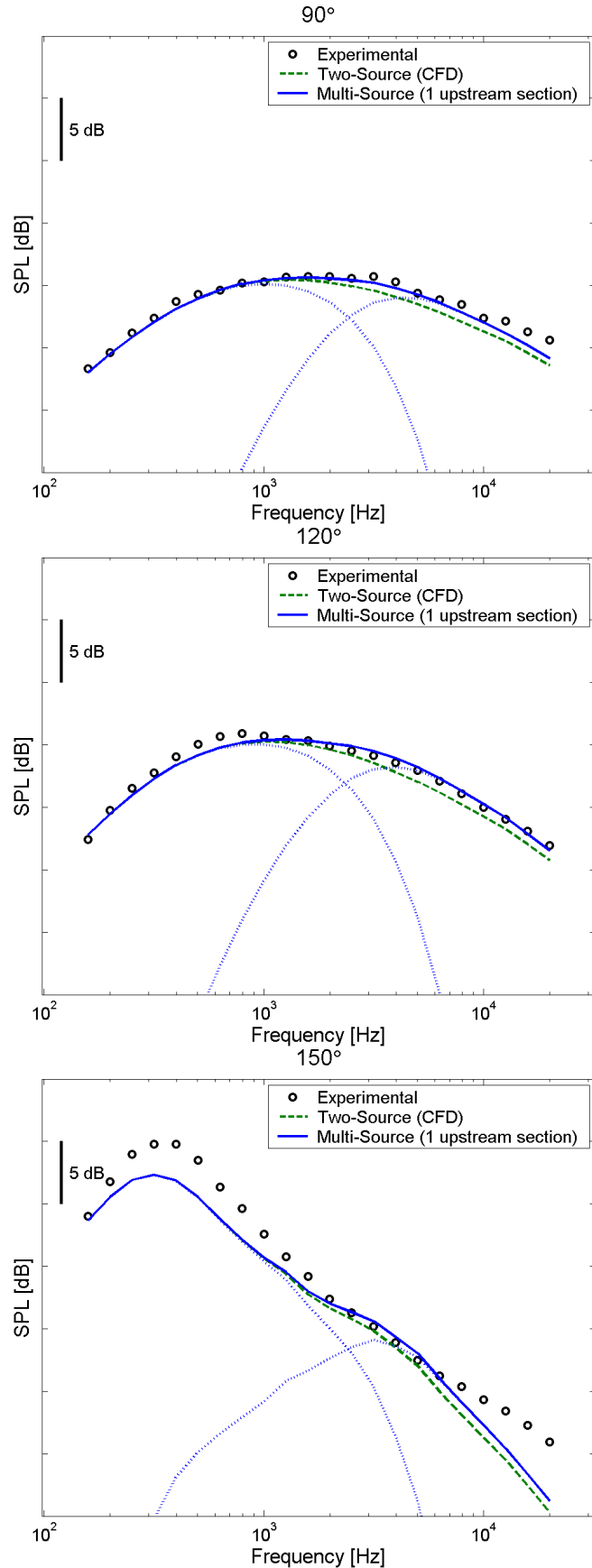


Figure 4.10. Two-source model noise predictions for the 12CL mixer at set point 110 using CFD-based velocity and temperature scales.

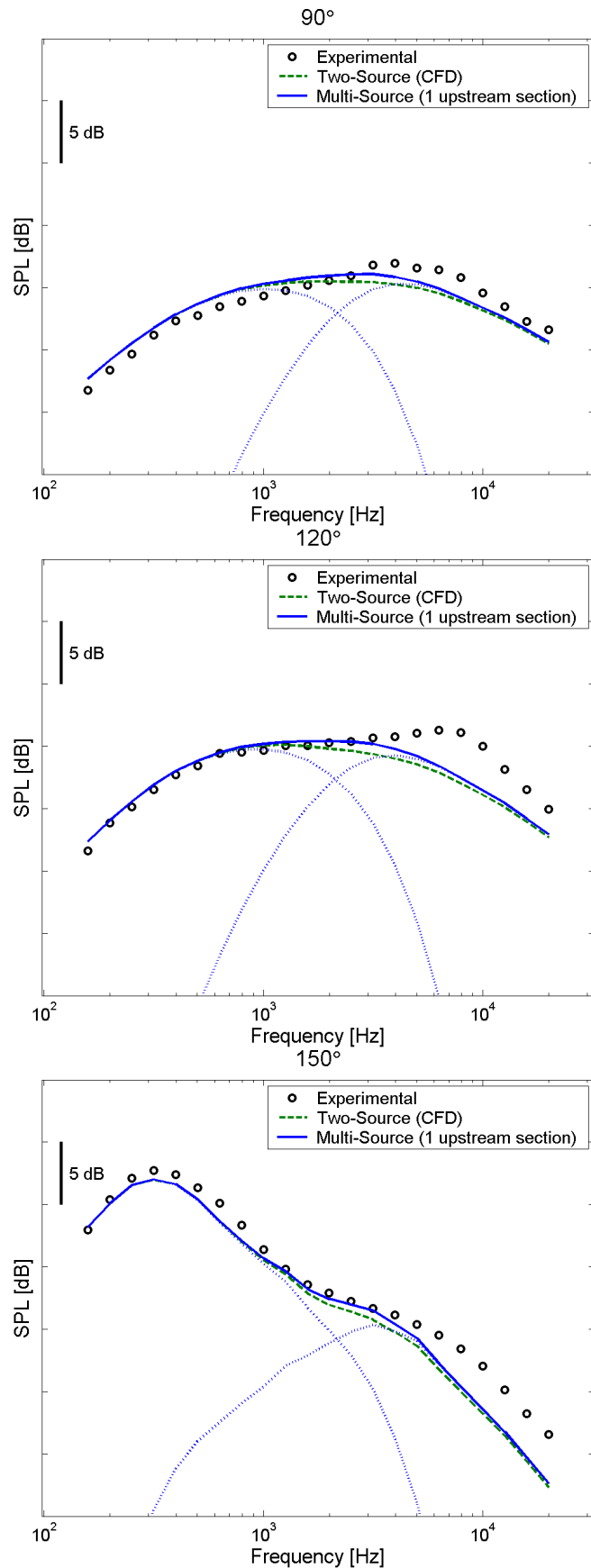


Figure 4.11. Two-source model noise predictions for the 12UM mixer at set point 110 using CFD-based velocity and temperature scales.

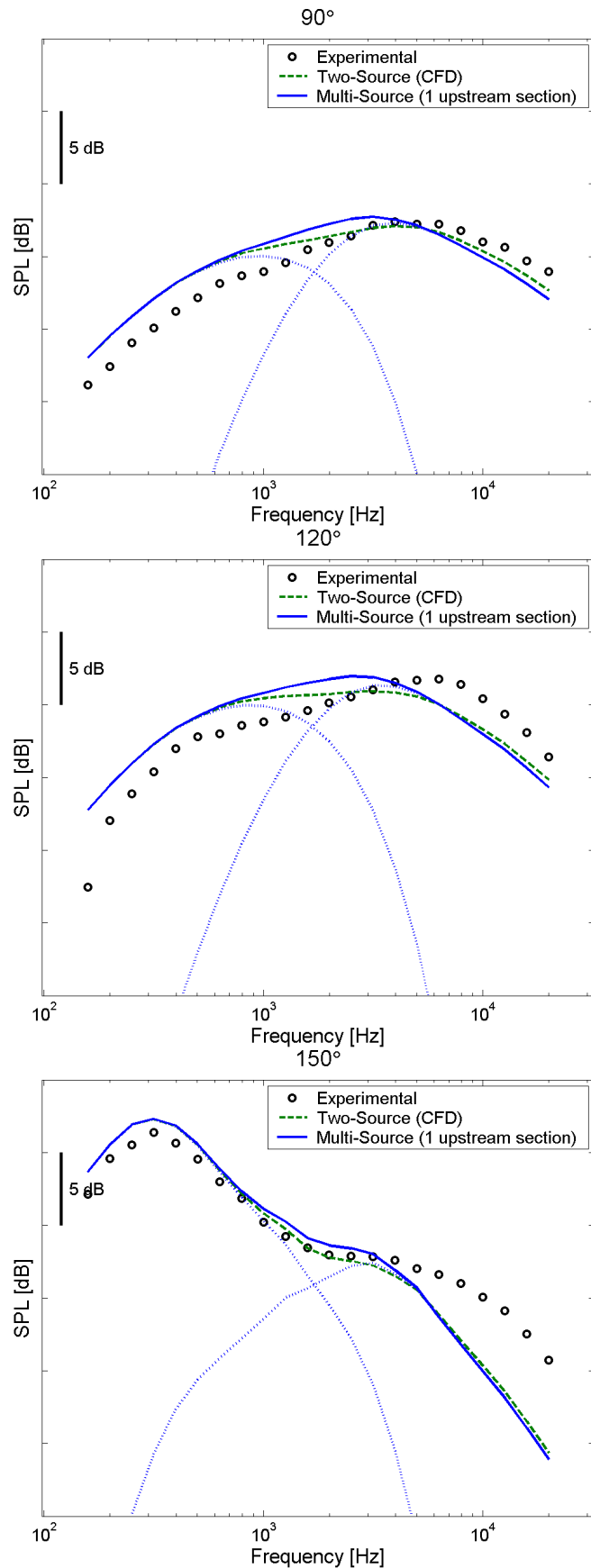


Figure 4.12. Two-source model noise predictions for the 12UH mixer at set point 110 using CFD-based velocity and temperature scales.

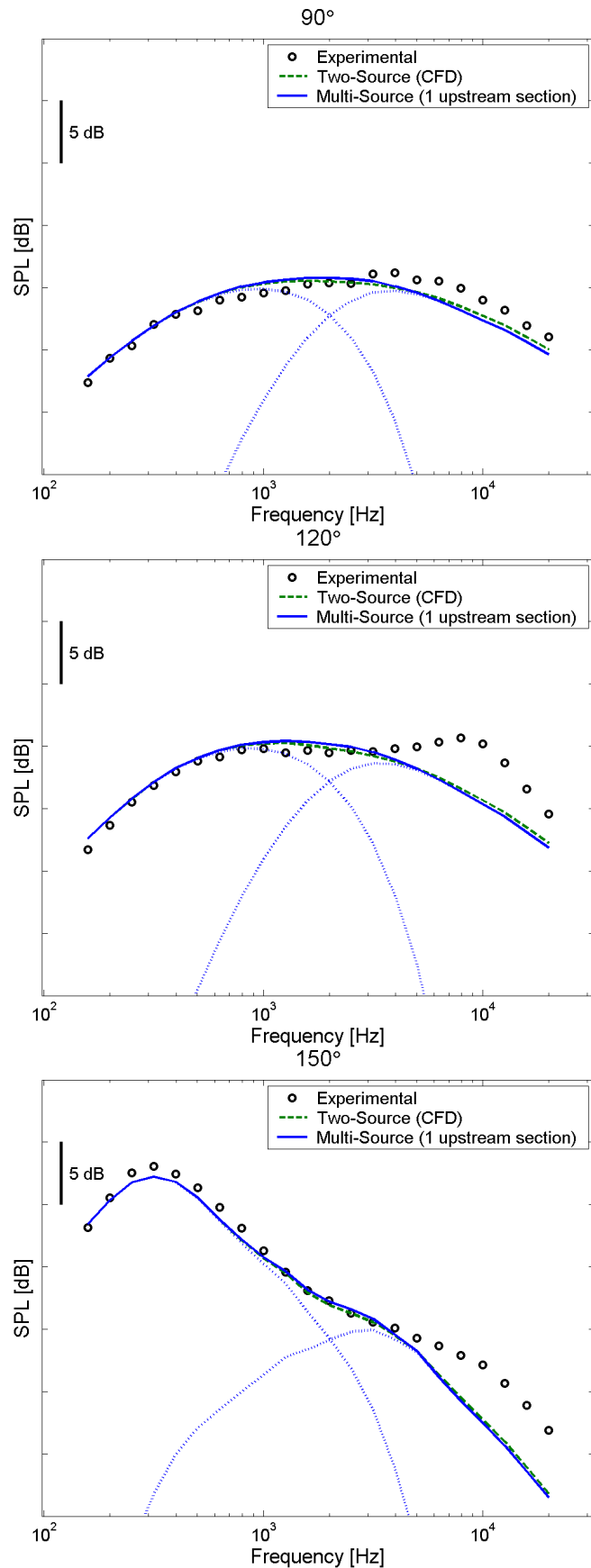


Figure 4.13. Two-source model noise predictions for the 20UH mixer at set point 110 using CFD-based velocity and temperature scales.

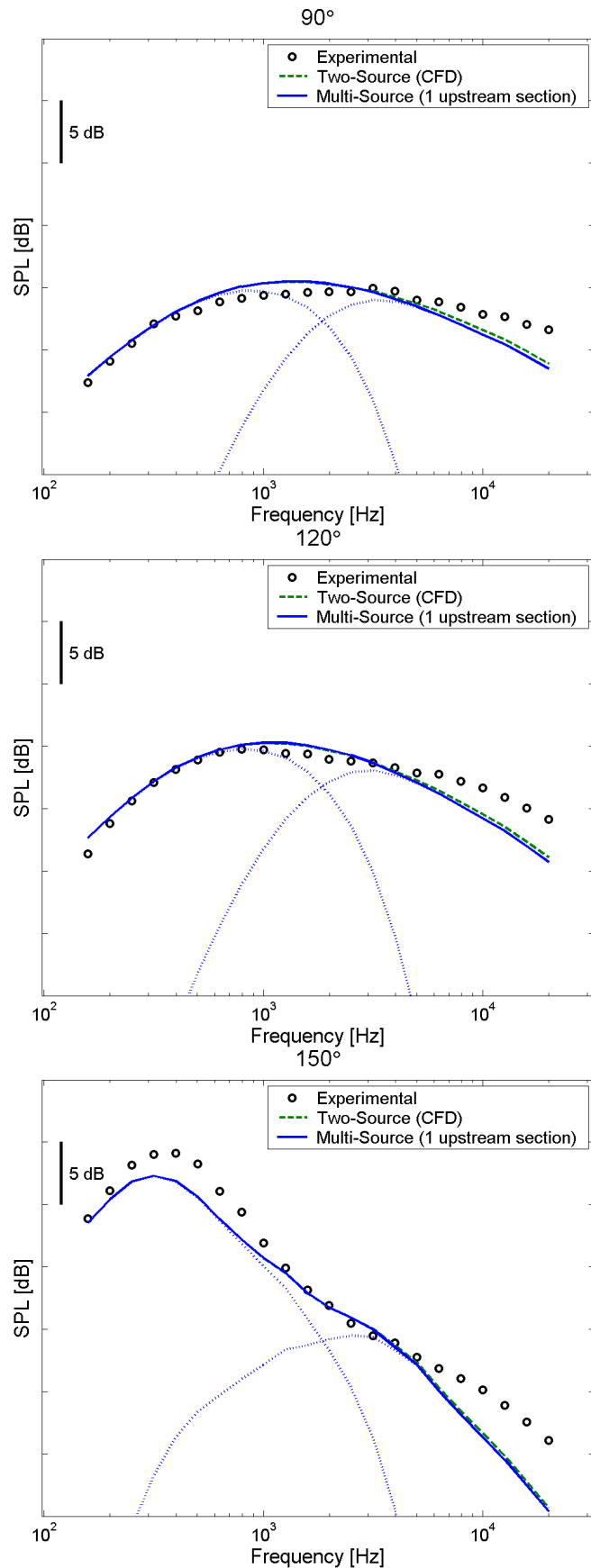


Figure 4.14. Two-source model noise predictions for the 20DH mixer at set point 110 using CFD-based velocity and temperature scales.

4.4 Four Section Multi-Source Model Predictions

In the previous section the process of extracting the upstream velocity and temperature scales directly from a RANS calculation was validated. In this section multi-source model predictions are made using four sections in the upstream region. The characteristic jet properties for each section are found by averaging the shear layer inside edge velocity and temperature values in a given section. In addition, the enhancement levels are determined by using the maximum turbulence intensity in each upstream section. The resulting upstream section characteristic jet properties and enhancement levels for the five lobed mixer designs are shown in Figure 4.15. Multi-source noise model predictions using these values are shown in Figures 4.16 to 4.20 for various mixers.

It is seen in Figure 4.16 that the multi-source model noise predictions show better agreement with the experimental data than the two-source model for the 12CL mixer. A similar trend is seen for 12UM mixer multi-source model predictions shown in Figure 4.17. However, it is noted that the multi-source noise model predictions for the 12UH mixer are slightly under-predicted for the 2 kHz to 6 kHz frequency range, as shown in Figure 4.18. It is believed that this under-prediction is due to the deficiencies in the CFD calculation of the enhanced turbulence intensities in the jet plume for this mixer. It is seen in Figures 4.19 and 4.20 that the multi-source model predictions for the 20UH and 20DH mixers are very close to the two-source model predictions.

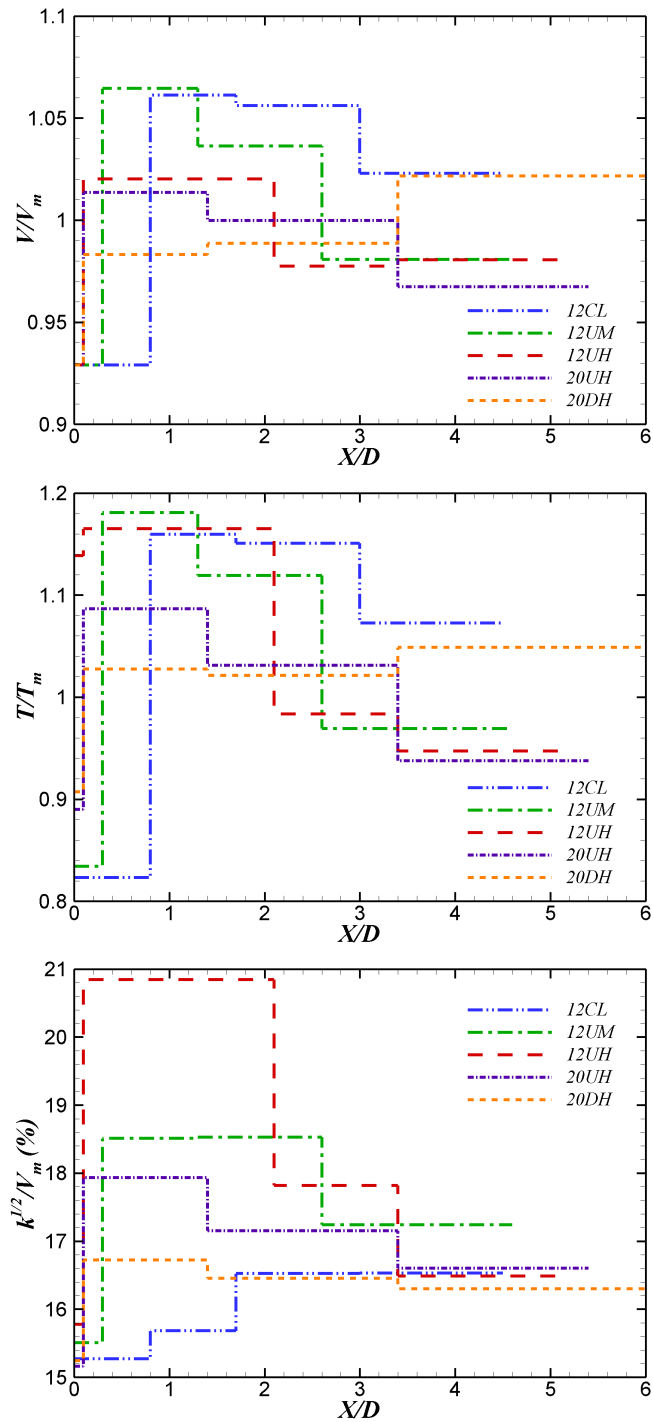


Figure 4.15. Characteristic jet properties for the multi-source model predictions with four upstream sections.

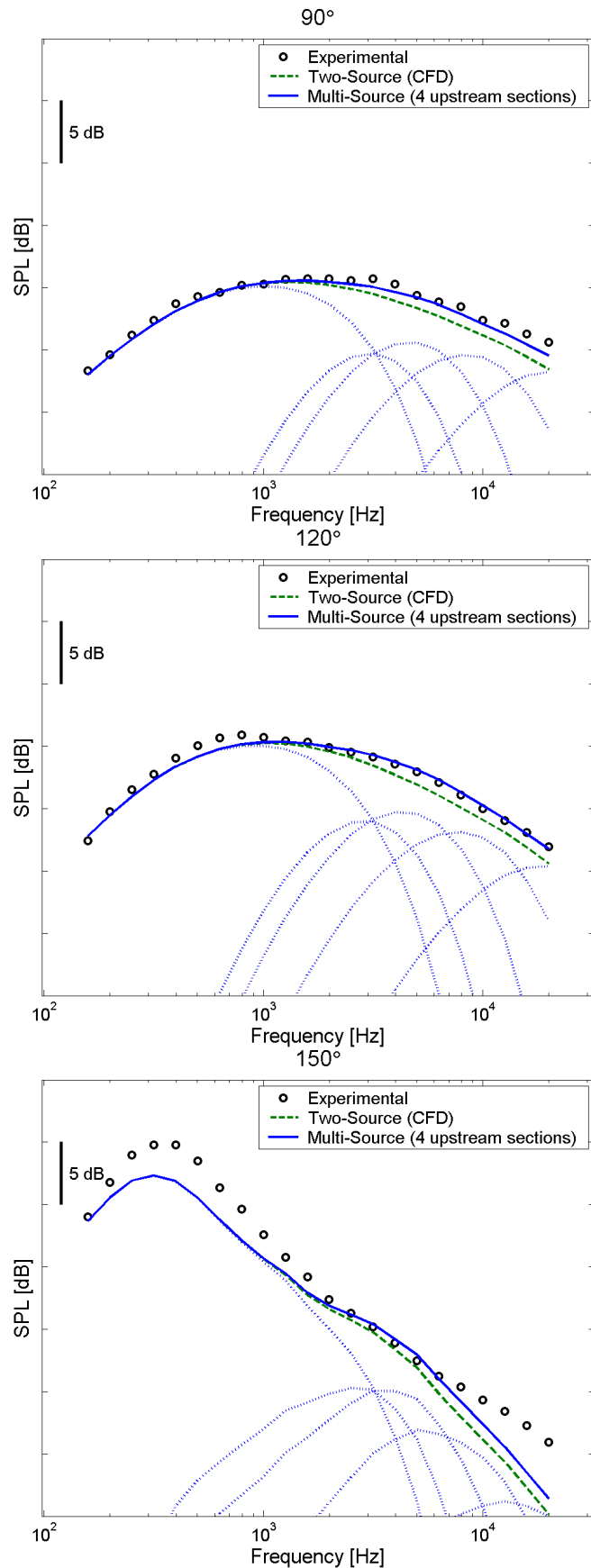


Figure 4.16. Multi-source model noise predictions for the 12CL mixer at set point 110.

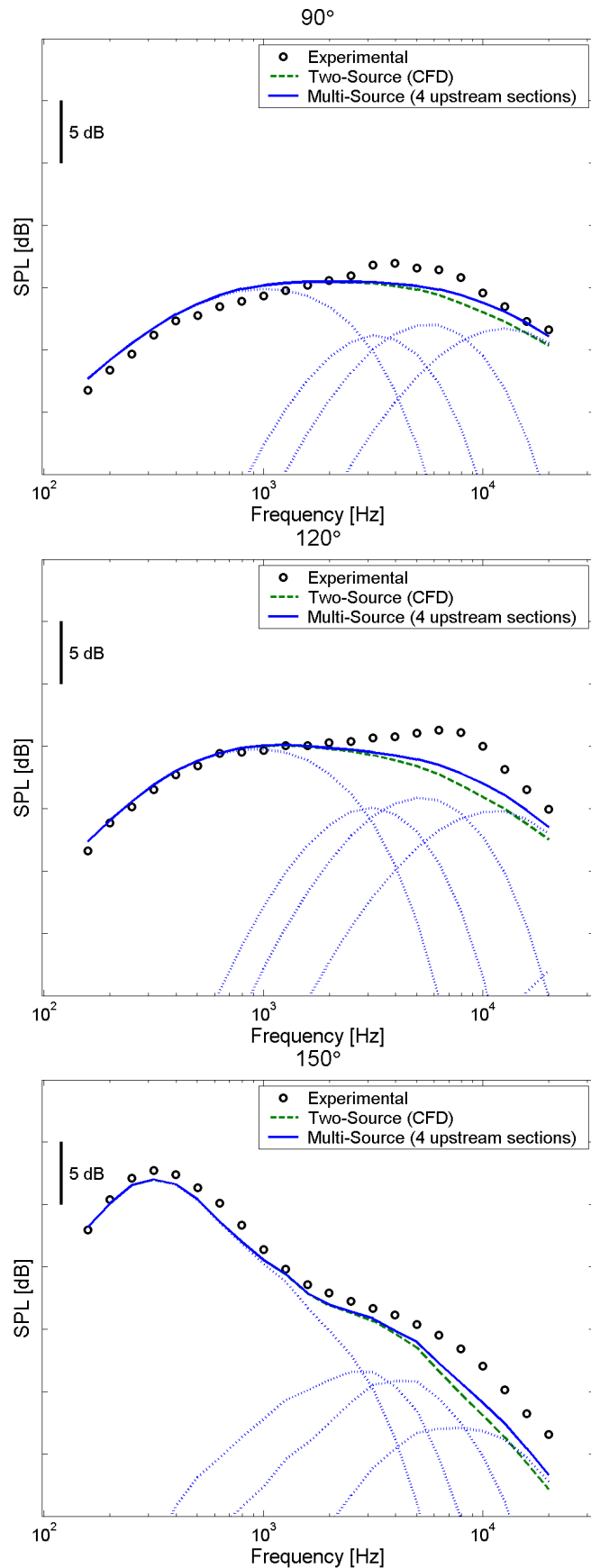


Figure 4.17. Multi-source model noise predictions for the 12UM mixer at set point 110.

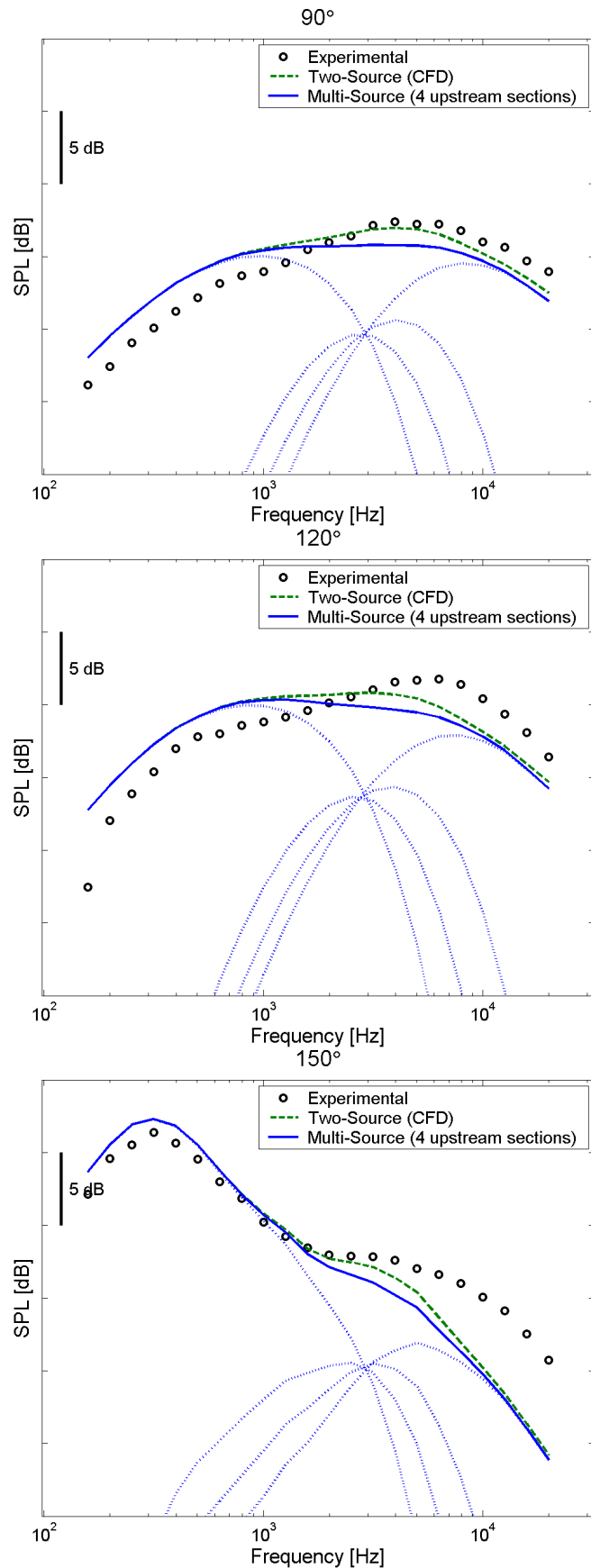


Figure 4.18. Multi-source model noise predictions for the 12UH mixer at set point 110.

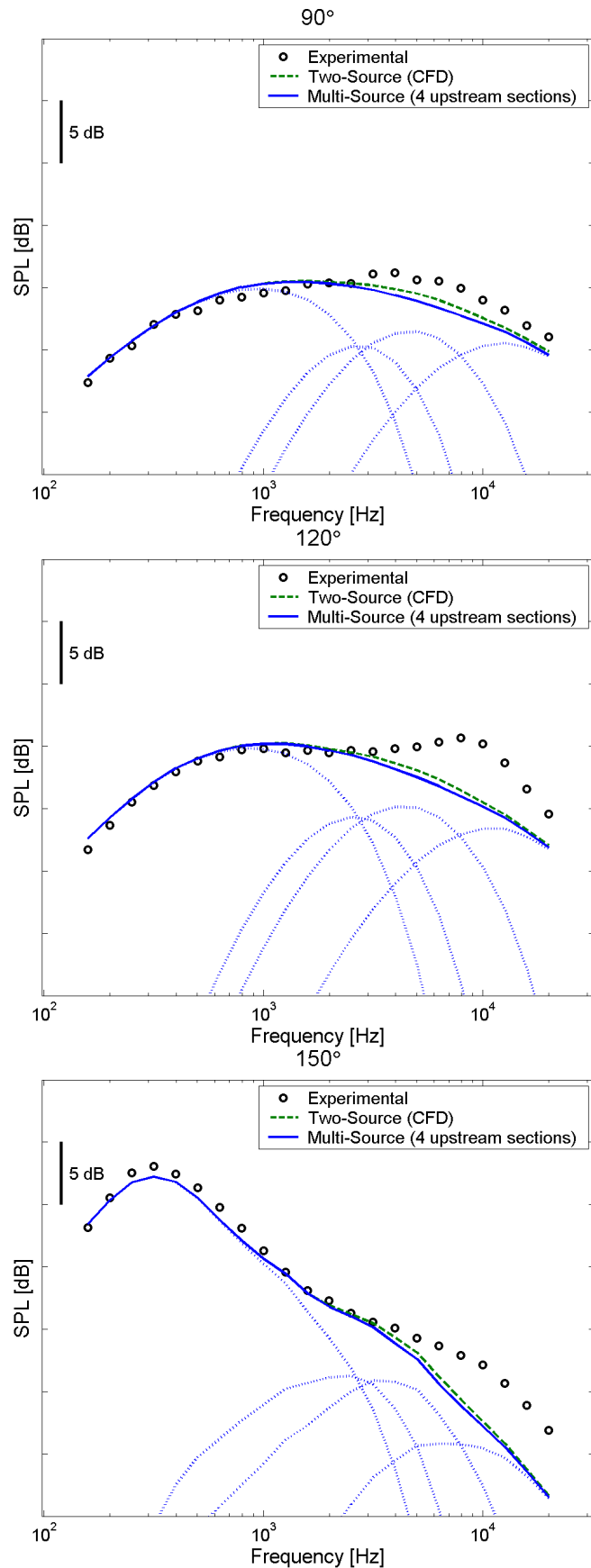


Figure 4.19. Multi-source model noise predictions for the 20UH mixer at set point 110.

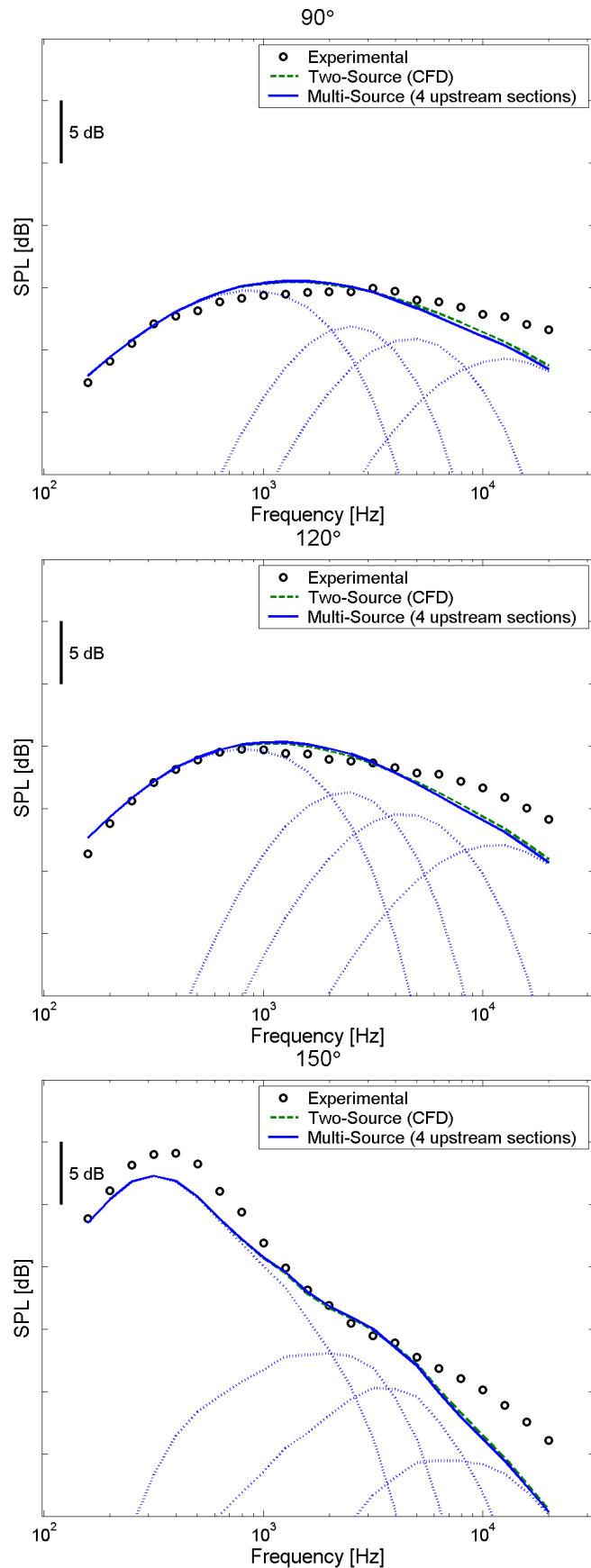


Figure 4.20. Multi-source model noise predictions for the 20DH mixer at set point 110.

5. High Mach Number Lift Noise Source

In a preliminary appraisal of the lobed mixer experimental acoustic data performed by Tester and Fisher [127] an additional noise source was identified in the jet noise spectra at the high power set points (310 and 312). This additional phenomenon, referred to as the high Mach number lift (HML), is seen in the high frequency region of the noise spectra, as shown in Figure 5.1. Additional analysis of the acoustic data by Tester and Fisher [122] has shown that this source does not exhibit a flight reduction that would be consistent with a shear layer based noise source. As a result, it is currently believed that this noise source is nozzle-based. A more intriguing result observed in the acoustic data is that the HML noise source is only present in the L0 and L2 nozzles, but not the L1 nozzle, and it is not present for the confluent mixer geometry. Nozzle length effects for these mixer configurations were also previously identified by Mengle [81, 82] for an earlier set of acoustic data. It has been shown by previous CFD work performed by Wright [84] that for the baseline L0 nozzle geometry at the high power set point a small region of supersonic flow occurs near the nozzle exit close to the nozzle wall, terminating in a normal shock. It has therefore been hypothesized that the HML noise source could be caused by turbulence from the streamwise vortices generated by the forced mixer passing through a normal shock at the nozzle exit.

Supersonic flow could occur in a convergent nozzle at sub-critical pressure ratios as a result of flow turning effects. The axial variation of the angle between the interior nozzle wall and the jet axis, which illustrates the flow turning effects of the various nozzles, is shown in Figure 5.2 for the L0, L1, and L2 nozzles. It is seen in Figure 5.2 that the L0 and L2 nozzles have a relatively rapid transition from the convergent section of the nozzle to the parallel section at the nozzle exit. In contrast, the L1 nozzle has a more gradual transition. The CFD results in the lobe

peak azimuthal plane of the 12UM mixer at set point 312 with the L0, L1, and L2 nozzles are shown in Figure 5.3. From these results it is seen that both the L0 and L2 nozzle geometries produce a normal shock at the final nozzle exit. However, a shock is not present at the nozzle exit for the L1 nozzle geometry. These findings are consistent with the flow turning effects shown in Figure 5.2. In addition, the Mach number profiles along lines offset from the nozzle wall are shown in Figures 5.4 and 5.5 for the L0 and L1 nozzles, respectively.

The turbulence kinetic energy just upstream of the normal shock for the 12-lobed mixers with the L0 nozzle is shown in Figure 5.6 for set point 312. In this figure the bold contour lines correspond to the supersonic region and the thin contour lines correspond to the subsonic flow region. An initial attempt to quantify the strength of HML noise source resulting from the turbulence-shock interaction is made by applying the CFD data to the theoretical work of Ribner [128–130]. The non-dimensional HML source strength is estimated as

$$HML \propto \int_A \frac{k}{U_m^2} \left(\frac{p_2 - p_1}{p_2} \right)^{0.323} e^{-3.5 \frac{p_2 - p_1}{p_2}} dA$$

where $p_2 - p_1$ is the difference in static pressure across the shock and the area of integration is the shock surface. The HML source strength is proportional to the turbulence kinetic energy, as suggested by Ribner. The functional dependence of the HML source strength with the shock strength (static pressure rise) was determined based on a curve fit to the Ribner theory. The calculated HML source strength values are plotted on the shock surface for the three 12-lobed mixers in Figure 5.7. The total integrated HML source strength for the 12UM mixer is 1.99 times stronger than the total HML source strength for the 12CL mixer, which is consistent with the 3 dB difference seen in the experimental data shown in Figure 5.1.

In addition to the source strength, the HML noise source peak frequencies are estimated using the Ribner theory [130]. The peak frequency is estimated as

$$f = \frac{K_1 U_A}{2\pi \tilde{a} L_{11}}$$

where U_A is the velocity upstream of the shock, \tilde{a} is a constant (1.339), L_{11} is the longitudinal turbulence length scale, and K_1 is the peak wave number of the far-field noise one-dimensional power spectra, which is estimated as 0.75 from the Ribner results. The upstream velocity and longitudinal turbulence length scales are calculated using the CFD data. The turbulence length scale, L , is calculated as

$$L = \frac{k^{3/2}}{\epsilon}, \quad (5.1)$$

where k is the turbulence kinetic energy and ϵ is the turbulence dissipation rate. The longitudinal turbulence length scale, L_{11} is then calculated from turbulence length scale, L , at every point in the flow field using Pope's model energy spectrum [131].

The HML noise source peak frequencies for the 12CL mixer with the L0 nozzle at set point 310 are shown in Figure 5.8. It is seen that these estimated peak frequencies are consistent with the frequency range of the HML noise source as seen in Figure 5.1. In Figure 5.1 it is seen that the high frequency lift in noise spectra occurs at frequencies greater than 5 kHz, and peaks at approximately 10 kHz. From the CFD-based predictions of the peak frequency from the shock-turbulence interaction it is observed that the peak frequencies range from 8 kHz to 30 kHz. In particular, in the region of flow with the high turbulence levels the CFD predicted peak frequencies appear to vary from approximately 10 kHz to 20 kHz.

The far-field directivity of the HML noise source has also been estimated by combining the Ribner theory for the refracted noise emission angle along with a geometric acoustics shear layer refraction correction. The results of this analysis are compared to the difference between Sound Pressure Level spectra of the L0 nozzle and L1 nozzle cases at 20 kHz for the 12CL mixer with the L0 nozzle at set point 310 in Figure 5.9. In Figure 5.9 the far field angle is referenced from the jet axis. It is seen in Figure 5.9 that the estimates of the far-field directivity of the HML noise source are in agreement with the experimental acoustic data.

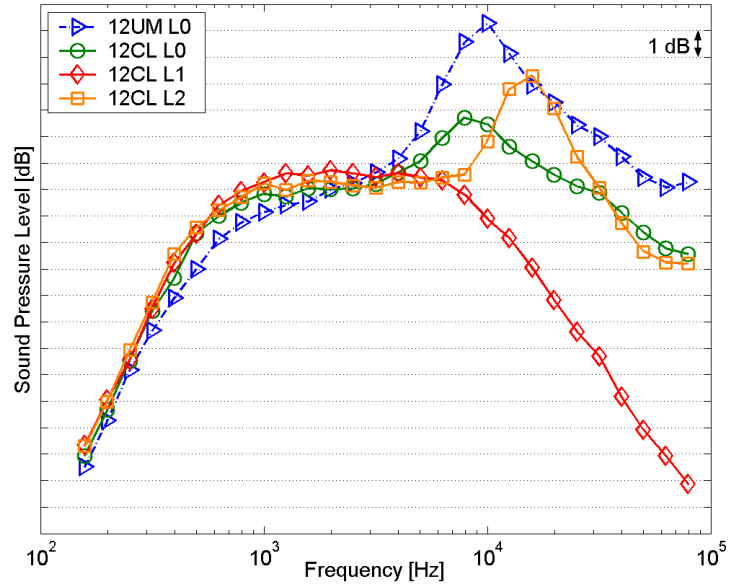


Figure 5.1. Far-field Sound Pressure Level spectra at 70° for the 12UM mixer with the L0 nozzle and the 12CL mixer with the L0, L1, and L2 nozzles at set point 310.

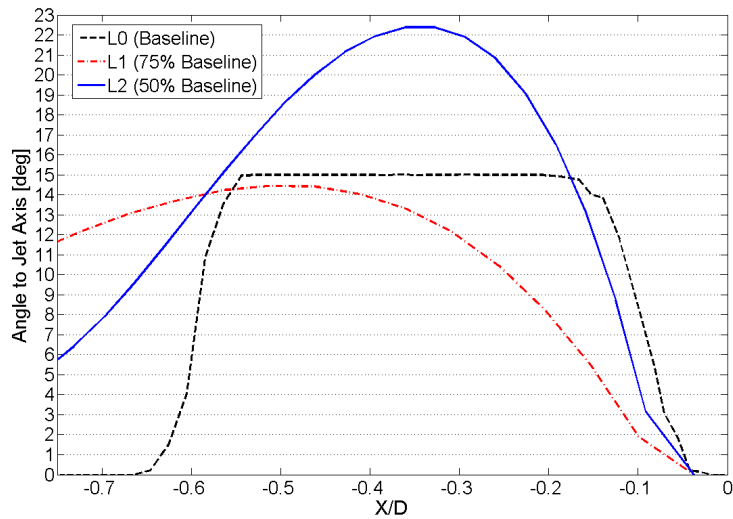


Figure 5.2. Axial variation of the angle between the interior nozzle wall and the jet axis for the L0, L1, and L2 nozzles.

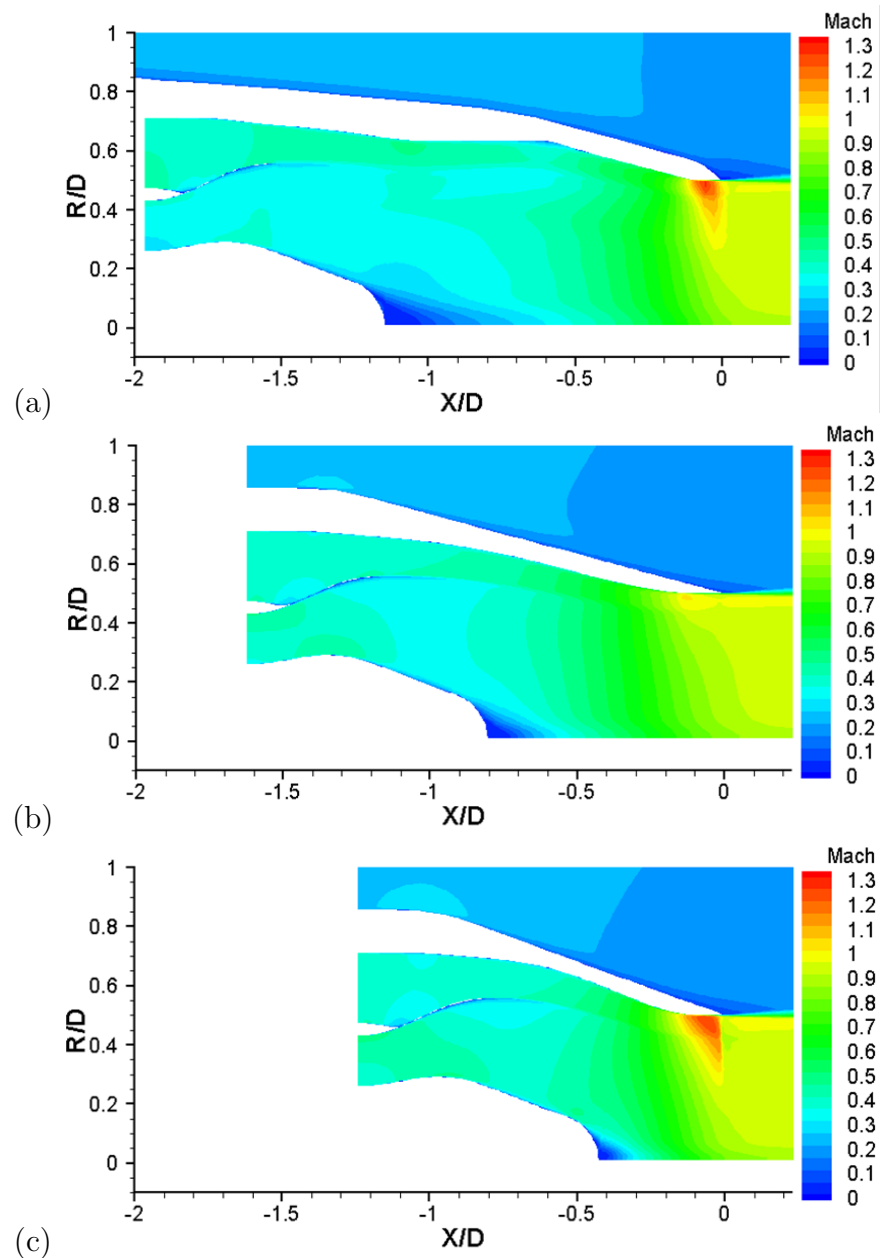


Figure 5.3. CFD Mach number contours for the 12UM mixer in the lobe peak azimuthal plane at set point 312 with the (a) L0 nozzle, (b) L1 nozzle, and (c) L2 nozzle.

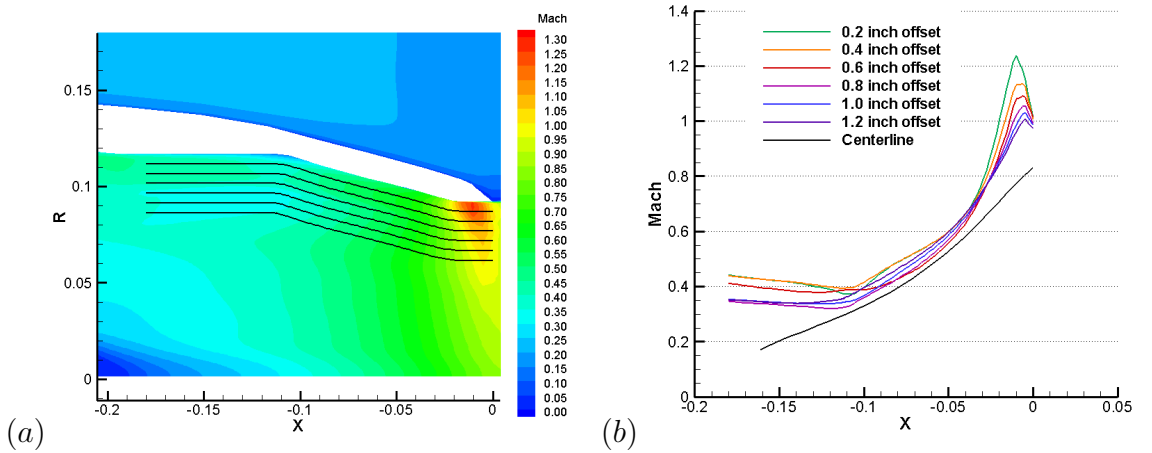


Figure 5.4. Axial Mach number variation in lobe peak azimuthal plane of the 12UM mixer with the L0 nozzle at set point 312 (a) Mach number contours and profile locations (b) Mach number profiles (along lines offset from the nozzle wall).

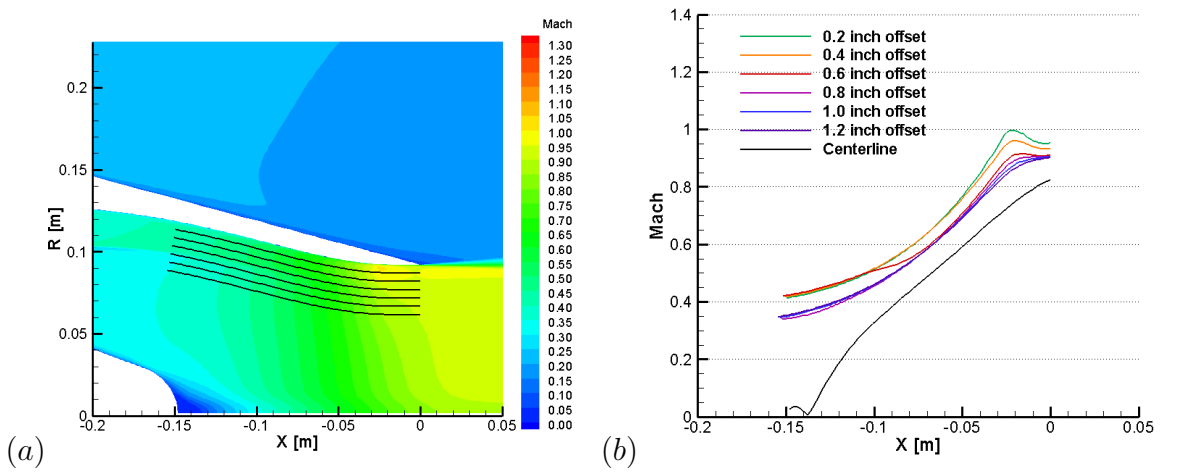


Figure 5.5. Axial Mach number variation in lobe peak azimuthal plane of the 12UM mixer with the L1 nozzle at set point 312 (a) Mach number contours and profile locations (b) Mach number profiles (along lines offset from the nozzle wall).

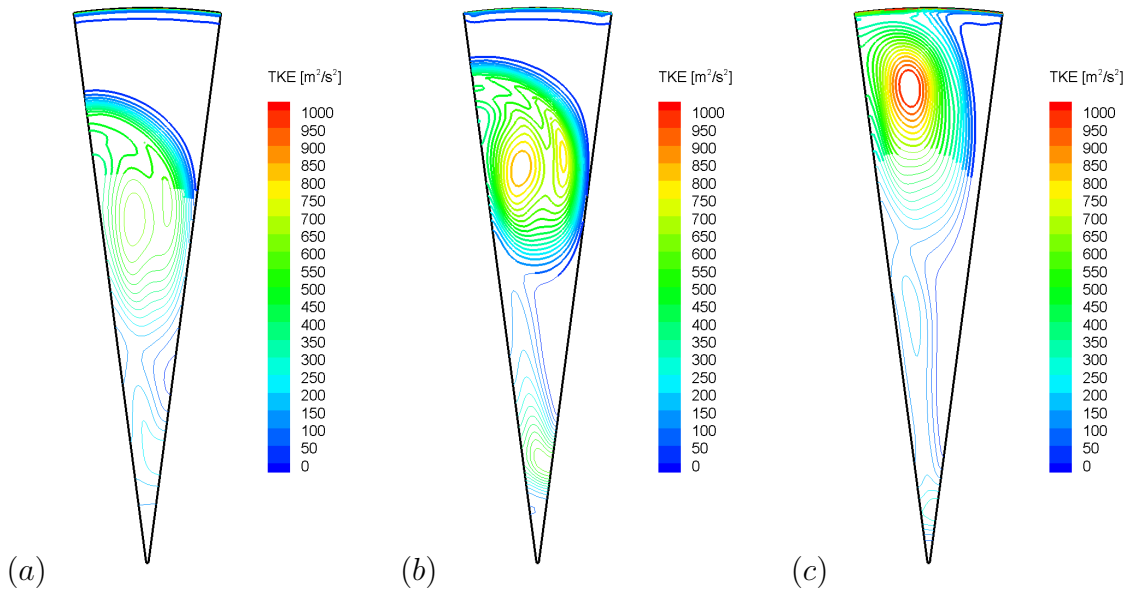


Figure 5.6. CFD turbulence kinetic energy upstream of the normal shock for the L0 nozzle with the (a) 12CL mixer, (b) 12UM mixer, and (c) 12UH mixer at set point 310; bold contours, supersonic region; thin contours, subsonic region.

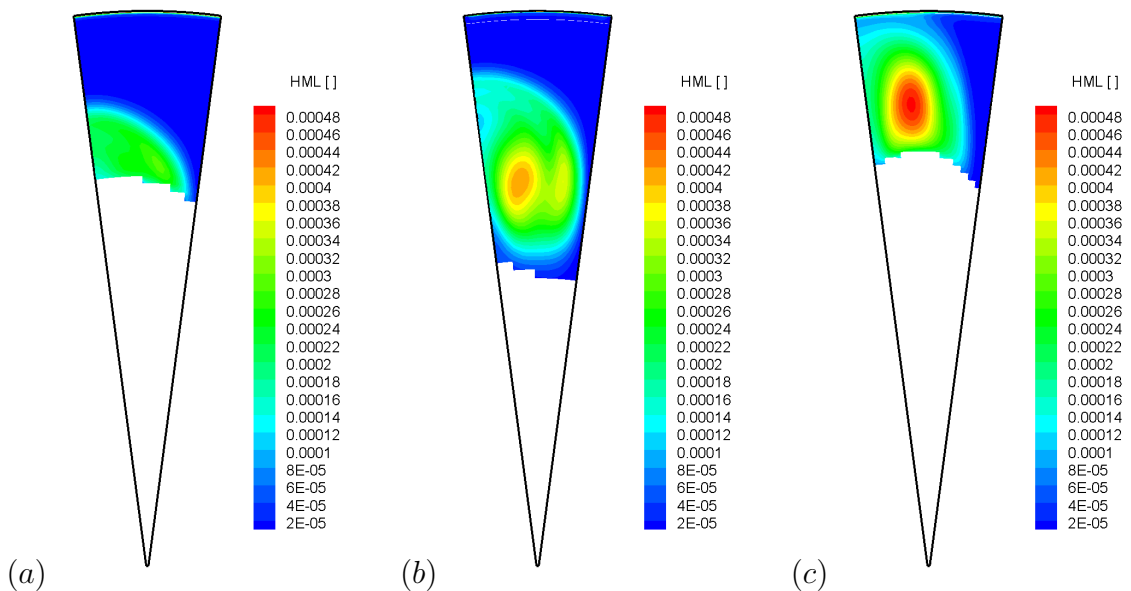


Figure 5.7. Estimated HML noise source strength on the shock surface for the L0 nozzle with the (a) 12CL mixer, (b) 12UM mixer, and (c) 12UH mixer at set point 310.

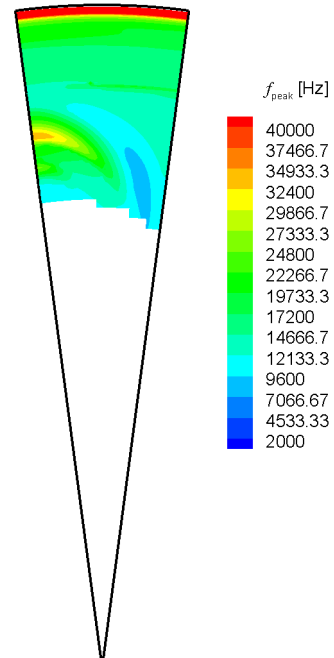


Figure 5.8. Estimated HML noise source peak frequencies for the 12CL mixer with the L0 nozzle at set point 310.

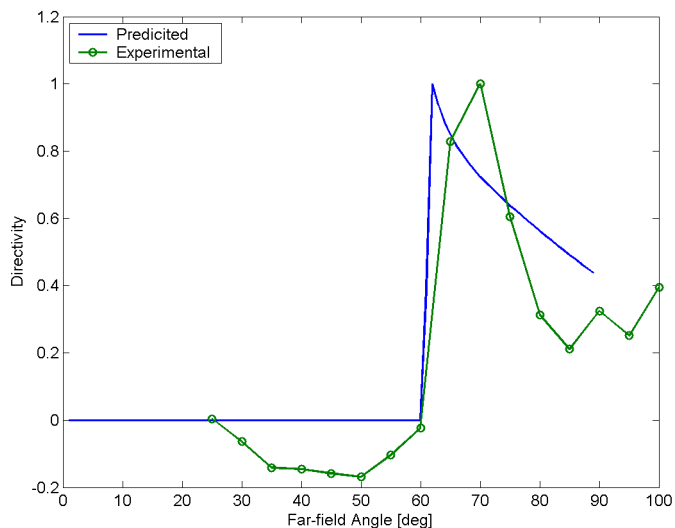


Figure 5.9. Estimated HML noise source directivity at for the 12CL mixer with the L0 nozzle at set point 310.

6. Conclusions and Recommendations for Future Work

6.1 Conclusions

The goal of the current research project is to advance the development of a new CFD-based jet noise prediction methodology for complex jet configurations that include internal forced mixers. The current methodology involves first determining the turbulent properties in the jet plume using RANS CFD and then supplying those properties to a noise prediction method that is based on single stream jet components. The new aspects of this work include the coupling of the turbulence data from a RANS CFD calculation with a two-source noise model, and the development of a more general multi-source noise model for general complex jet configurations. In addition, the characterization of the High Mach Number (HML) lift noise source using CFD analysis is a new contribution. The development and advancement of the noise prediction tools investigated in this study will help industry in designing quieter aircraft engines, which will ultimately result in the improvement of the environmental quality in communities surrounding airports.

As part of the current research effort CFD analysis of internally mixed jets with six different mixer geometries have been completed. A turbulence model sensitivity study was performed for the axisymmetric confluent mixer case using a range of turbulence models with both the WIND and FLUENT flow solvers. This analysis showed that the WIND SST turbulence model and FLUENT SST and $k - \epsilon$ turbulence models yielded the best agreement with experimental PIV data. In this study all of the lobed mixer calculations were performed using the WIND flow solver with the two-equation Menter SST turbulence model. The CFD flow fields were compared to experimental PIV data at several axial planes in the jet plume. Excellent agreement was observed for the mean velocity field for all of the mixer configura-

tions, with the exception of the scalloped mixer (20DH). For this geometry some noticeable differences were observed in the structure of the mean velocities in the jet plume. In particular, it was observed that the PIV data for this configuration showed a more uniform velocity distribution just downstream of the nozzle exit, suggesting that the CFD analysis for this mixer is under-predicting the mixing of the primary and secondary flows.

Several shortcomings were observed in the CFD predicted turbulence levels in the plume for all of the mixer configurations. In particular, it is noted that the CFD analysis generally over-predicts the turbulence intensities in the initial portion of the main jet shear layer. However, it was found that the ratio of the peak turbulence levels in the plume of the lobed mixer cases to those in a single stream jet are actually under-predicted by the CFD analysis. This ratio is the key CFD quantity that is used in the noise models described below. Fortunately though, it was observed that the CFD analysis predicts the correct trends in the enhancement of the turbulence levels for various mixer designs.

In the current study two-source noise predictions were made using model parameters that were determined from the RANS CFD flow fields. These predictions showed that the CFD-based upstream enhancement level was under-predicted when compared to the empirically derived model parameters. It is believed that this under-prediction is the result of an under-prediction of the WIND SST calculations of the enhanced turbulence intensities in the main jet shear layer. However, it was observed that for the unscalloped mixers the trends in the CFD-based two-source model upstream enhancement parameter are consistent with the empirically derived model parameters. In particular, the CFD-based model parameters correctly predict the trend that the upstream enhancement level increases with increasing lobe penetration height. In addition, the CFD-based upstream enhancement for the 20UH mixer correctly falls between the 12CL and 12UM mixers.

The multi-source model noise predictions for the 12CL and 12UM mixers showed a slight improvement over the two-source model predictions. This improvement is

due to the use of increased velocity scales in the single jet predictions for the upstream regions. However, the multi-source model noise predictions for the 12UH mixer show an even greater under-prediction of the high frequency noise compared to two-source model predictions. This behavior is due to deficiencies in the CFD predictions of the turbulence intensities for the more aggressive high penetration mixer. In particular, the under-prediction of the enhancement of the plume turbulence levels are more pronounced for the 12UH mixer. These discrepancies in the plume turbulence levels are directly reflected in the noise predictions.

Finally, the results from the CFD analysis at the high power set points (310 and 312) with various nozzle geometries supports the present theory that the origin of the high Mach number lift noise source is due to the interaction of turbulence with a normal shock at the nozzle exit. It is seen that the strength of this noise source estimated by using the Ribner theory is consistent with the experimental acoustic data. In addition, the estimated noise source frequency and far field directivity are also in agreement with experimental data.

6.2 Recommendations for Future Work

CFD Analysis Improvements

It is believed that the weakest link in the current jet noise prediction methodology lies in deficiencies in the CFD prediction of the turbulence levels in the jet plume. It was noted that the CFD predictions of the peak turbulence intensities in a simple jet shear layer (16.4%) are over-predicted compared to experimental data (15%). However, even if the CFD-based two-source model upstream enhancement levels (Γ_U) were calculated using a reference single jet value 15% the resulting Γ_U values for the forced mixer cases would still be under-predicted. This result clearly shows that in order for the CFD-based Γ_U values to be consistent with the two-source model empirical values, greater turbulence levels are needed in the upstream region where the streamwise vortices interact with the main jet shear layer.

In the current work it was seen that the multi-source model provided noise predictions that were at best only marginally better when compared to two-source model predictions, despite the inclusion of a more general representation of the flow field properties in the jet plume. It is believed that the deficiencies of the multi-source model predictions are primarily due to inaccurate CFD predictions of the turbulence intensities. It is important to note that the multi-source model takes into account the axial variations of the turbulence kinetic energy in the jet plume, where the two-source model only considers the peak value. As a result, accurate multi-source model predictions are strongly dependent on the CFD predictions of the turbulence in the entire upstream region of the jet plume. The turbulence levels in this part of the plume are generated by both the mean velocity gradient in the main jet shear layer and by the interaction of the shear layer turbulence and the turbulent streamwise vortices. It is, therefore, important that the CFD be able to accurately predict the turbulence levels for both cases. Currently, it is seen that the **WIND SST calculations over-predict the turbulence levels that are generated by the mean velocity gradient in the shear layer; however, they under-predict the interaction of the shear layer turbulence and the turbulent streamwise vortices.**

Based on the preceding analysis it is suggested that improvements to the turbulence model have the greatest potential to improve the current stand-alone noise prediction methodology. These improvements could take the form of corrections to existing two-equation turbulence models, such as the variable diffusion correction recently investigated by Engblom *et al.* [66]. Alternatively, more advanced Reynold stress turbulence models could be applied. In either case, it is important to note that for the current application it will be necessary to validate the turbulence intensities in jet plumes that are generated by the two distinct sources that were previously mentioned, namely mean velocity gradients and turbulence-turbulence interactions.

In addition to RANS CFD analysis, it may be possible to improve the quality of the CFD predictions of the turbulence kinetic energy by using more advanced hybrid methods, such as detached eddy simulations (DES). Although this approach

may currently be too computationally expensive to be practical for industry design studies, it would certainly be a useful tool in validating the current CFD-based noise prediction methodologies.

Additional improvements in the RANS CFD analysis could also be attained through the use of overlapping grids. In particular, overlapping, or chimera, boundary conditions could be used in the plume zones to eliminate the slight discontinuity that is often seen in the turbulence kinetic energy at abutting zone interfaces. In addition, overlapping grids could be applied near the lobed mixer surface to improve the quality of the grid cells in these highly skewed regions.

Noise Modeling Improvements

The focus of the current noise modeling work was to produce a CFD-based noise prediction tool that can predict the far field Sound Pressure Levels of a jet with an internal forced mixer. When considering noise reduction devices for aircraft applications it is also important to consider the impact on performance. It is most relevant to compare jet noise on an equal thrust basis, therefore; in the design of new mixers it is important to be able to estimate the aerodynamic performance in addition to the acoustic performance. In light of this fact, future implementations of the currently developed noise models will also require accurate CFD predictions of the thrust penalties of a given mixer design.

In the current two-source model formulation the CFD-based enhancement level is calculated using the peak turbulence intensity in the jet plume. An improved method for calculating this model parameter using RANS CFD data could involve the use of the Lighthill acoustic analogy to determine the enhancement of the high frequency noise sources. In this approach, the far field Sound Pressure Level spectrum at 90° would be calculated by applying a form of the Lighthill acoustic analogy. In particular, a full three-dimensional integration of the Lighthill sources would be performed over the upstream region of the jet plume. This process would be performed

for the lobed mixer flow field and for a reference single stream jet flow field. The two-source model upstream enhancement level would then be found by determining the relative increase in the high frequency portion of the 90° spectrum. Using this type of approach would help to include both axial and azimuthal variations in the turbulence levels in the upstream region for two-source model predictions. A similar approach could also be applied to the multi-source model formulation to determine the enhancement levels for each upstream section.

The current noise prediction methodologies assume that a negligible amount of sound is generated by primary-secondary mixing layer. For the forced mixer geometries this mixing layer is effectively replaced by the turbulent streamwise vortices. For the high velocity ratio cases that are considered in this study, the turbulence levels in the primary-secondary flow mixing region are relatively small compared to those in the main jet shear layer. As a result, neglecting the noise from this region appears to be a reasonable assumption. However, it is possible that under certain circumstances (lower velocity ratio flows) this noise source could produce a significant contribution to the total jet noise levels. As a result, for these cases it would be necessary to add an additional source to the noise model.

In the current research effort it was shown that the characteristics of the high Mach number lift (HML) noise source are consistent with the noise generated by the interaction the turbulent streamwise vortices with a normal shock at the nozzle exit. In particular the amplitude, directivity, and frequency content of the HML noise was estimated using Ribner's theory for shock-turbulence interaction noise. This work could be extended to form a complete model of the HML noise source by representing the shock-turbulence interaction noise as a distribution of point sources at the nozzle exit. The far-field Sound Pressure Levels could then be determined using a model to account for the refraction of the sound through the jet shear layer.

LIST OF REFERENCES

LIST OF REFERENCES

- [1] J. B. Freund, S. K. Lele, and P. Moin. Direct numerical simulation of a Mach 1.92 turbulent jet and its sound field. *AIAA Journal*, 38(11):2023–2031, 2000.
- [2] J. B. Freund. Noise sources in a low-Reynolds number turbulent jet at Mach 0.9. *Journal of Fluid Mechanics*, 438:277–305, 2001.
- [3] A. Uzun. *3-D Large Eddy Simulation for Jet Aeroacoustics*. PhD thesis, School of Aeronautics and Astronautics, Purdue University, West Lafayette, IN, December 2003.
- [4] M. J. Lighthill. On the sound generated aerodynamically: I, General theory. *Proc. Royal Soc. London A*, 211:564–587, 1952.
- [5] M. J. Lighthill. On the sound generated aerodynamically: II, Turbulence as a source of sound. *Proc. Royal Soc. London A*, 222:1–32, 1954.
- [6] G. M. Lilley. The generation and radiation of supersonic jet noise. Part IV: Theory of turbulence generated jet noise, noise radiation from upstream sources and combustion noise. AFAPL-TR-72-53 Volume IV, 1972.
- [7] R. Mani. The influence of jet flow on jet noise. *Journal of Fluid Mechanics*, 73(4):753–793, 1976.
- [8] T. E. Balsa. The acoustic field of sources in shear flow with application to jet noise: Convective amplification. *Journal of Fluid Mechanics*, 79(1):33–47, 1977.
- [9] T. F. Balsa and P. R. Grieve. Aerodynamics and noise of coaxial jets. *AIAA Journal*, 15(11):1550–1558, 1977.
- [10] P. R. Grieve and T. F. Balsa. Aeroacoustics of axisymmetric single- and dual-flow exhaust nozzles. *Journal of Aircraft*, 15(11):743–749, 1978.
- [11] A. Khavaran, E. A. Krejsa, and C. M. Kim. Computation of supersonic jet mixing noise for an axisymmetric convergent divergent nozzle. *Journal of Aircraft*, 31(3):603–609, 1994.
- [12] A. Khavaran. Role of anisotropy in turbulent mixing noise. *AIAA Journal*, 37(7):832–841, 1999.
- [13] A. Khavaran and N. Georgiadis. Aeroacoustics of supersonic elliptic jets. AIAA Paper No. 1996-0641, 1996.
- [14] A. Hamed, A. Khavaran, and S. Lee. The flow and acoustic predictions for a high bypass ratio exhaust nozzle. AIAA Paper No. 1998-3257, 1998.

- [15] T. J. Barber, L. M. Chiappetta, and S. H. Zysman. An assessment of jet noise analysis codes for multistream axisymmetric and forced mixer nozzles. AIAA Paper No. 1996-0750, 1996.
- [16] T. J. Barber, A. Nedungadi, and A. Khavaran. Predicting the jet noise from high speed jets. AIAA Paper No. 2001-0819, 2001.
- [17] L. D. Koch, J. Bridges, and A. Khavaran. Flowfield comparisons from three Navier-Stokes solvers for an axisymmetric separate flow jet. NASA TM-2002-211350, February 2002. Also published as AIAA Paper No. 2002-0672.
- [18] L. D. Koch, J. Bridges, C. Brown, and A. Khavaran. Numerical and experimental determination of the geometric far field for round jets. NASA TM-2003-212379, May 2003.
- [19] L. D. Koch, J. Bridges, and A. Khavaran. Mean flow and noise prediction for a separate flow jet with chevron mixers. NASA TM-2004-212906, February 2004. Also published as AIAA Paper No. 2004-0189.
- [20] W. A. Engblom, A. Khavaran, and J. Bridges. Numerical predictions of chevron nozzle noise reduction using WIND-MGBK methodology. AIAA Paper No. 2004-2979, May 2004.
- [21] A. Khavaran, J. Bridges, and N. Georgiadis. Prediction of turbulence-generated noise in unheated jets: Part 1, JeNo technical manual (version 1.0). NASA TM-2005-213827, July 2005.
- [22] A. Khavaran and J. Bridges. Modelling of fine-scale turbulence mixing noise. *Journal of Sound and Vibration*, 279:1131–1154, 2005.
- [23] A. Khavaran and J. Bridges. A parametric study of fine-scale turbulence mixing noise. NASA TM-2002-211696, July 2002. Also published as AIAA Paper No. 2002-2419.
- [24] M. E. Goldstein and A. Khavaran. Acoustic source modeling for high speed air jets. NASA TM-2005-213416, January 2005. Also published as AIAA Paper No. 2005-0415.
- [25] R. H. Self. Jet noise prediction using the Lighthill acoustic analogy. *Journal of Sound and Vibration*, 275:757–768, 2004.
- [26] P. J. Morris and F. Farassat. Acoustic analogy and alternative theories for jet noise prediction. *AIAA Journal*, 40(4):671–680, 2002.
- [27] S. L. Woodruff, J. M. Seiner, M. Y. Hussaini, and G. Erlebacher. Implementation of new turbulence spectra in the Lighthill analogy source terms. *Journal of Sound and Vibration*, 242(2):197–214, 2001.
- [28] M. Harper-Bourne. Jet noise turbulence measurements. AIAA Paper No. 2003-3214, May 2003.
- [29] J. Bridges and M. P. Wernet. Measurements of the aeroacoustic sound source in hot jets. AIAA Paper No. 2003-3130, May 2003.
- [30] R. Self and A. Bassetti. A RANS based jet noise prediction scheme. AIAA Paper No. 2003-3325, May 2003.

- [31] G. J. Page, J. J. McGuirk, M. Hossain, R. H. Self, and A. Bassetti. A CFD coupled acoustics approach for coaxial jet noise. AIAA Paper No. 2003-3286, May 2003.
- [32] C. Hunter and R. Thomas. Development of a jet noise prediction scheme for installed jet configurations. AIAA Paper No. 2003-3169, May 2003.
- [33] F. Farassat, M. J. Doty, and C. R. Hunter. The acoustic analogy - a powerful tool in aeroacoustics with emphasis on jet noise prediction. AIAA Paper No. 2004-2872, May 2004.
- [34] C. K. W. Tam and L. Auriault. Jet mixing noise from fine-scale turbulence. *AIAA Journal*, 37(2):145–153, 1999.
- [35] Society of Automotive Engineers Inc. *ARP876C: Gas Turbine Jet Exhaust Noise Prediction*, November 1985.
- [36] Engineering Science Data Unit. *ESDU-98019: Computer-Based Estimation Procedure for Single-Stream Jet Noise: Including Far-Field, Static Jet Mixing Noise Database for Circular Nozzles*, 2003.
- [37] Society of Automotive Engineers Inc. *AIR1905: Gas Turbine Coaxial Exhaust Flow Noise Prediction*, December 1985.
- [38] Engineering Science Data Unit. *ESDU-01004: Computer-Based Estimation Procedure for Coaxial Jet Noise: Including Far-Field Subsonic Jet Mixing Noise Database for Stationary, Coplanar Conical Nozzles*, 2003.
- [39] M. J. Fisher, G. A. Preston, and W. D. Bryce. A modelling of the noise from simple coaxial jets Part I: With unheated primary flow. *Journal of Sound and Vibration*, 209(3):385–403, 1998.
- [40] M. J. Fisher, G. A. Preston, and C. J. Mead. A modelling of the noise from simple coaxial jets Part II: With heated primary flow. *Journal of Sound and Vibration*, 209(3):405–417, 1998.
- [41] G. A. Preston. *Modelling of Sound Source Regions for the Prediction of Coaxial Jet Noise*. PhD thesis, Institute of Sound and Vibration, University of Southampton, 1996.
- [42] N. J. Georgiadis, D. A. Yoder, and J. R. DeBonis. A comparison of three Navier-Stokes solvers for exhaust nozzle flowfields. NASA TM-1999-209184, May 1999. Also published as AIAA Paper No. 99-0748.
- [43] T. DalBello. WIND validation cases: Computational study of thermally-perfect gases. NASA CR-2002-212015, December 2002. Also published as AIAA Paper No. 2003-0546.
- [44] M. A. Dembowski and N. J. Georgiadis. An evaluation of parameters influencing jet mixing using the WIND Navier-Stokes code. NASA TM-2002-211727, August 2002.
- [45] N. J. Georgiadis, C. L. Rumsey, D. A. Yoder, and K. B. M. Q. Zaman. Effects of RANS turbulence modeling of calculation of lobed nozzle flowfields. AIAA Paper No. 2003-1271, January 2003.

- [46] K. J. Franko and N. J. Georgiadis. Computational investigation of heated high-speed coaxial jets. AIAA Paper No. 2004-2980, May 2004.
- [47] N. J. Georgiadis and D. Papamoschou. Computations of dual-stream jets with eccentric and coaxial bypass streams. AIAA Paper No. 2004-2981, May 2004.
- [48] T. DalBello, N. J. Georgiadis, D. A. Yoder, and T. G. Keith. Computational study of axisymmetric off-design nozzle flows. AIAA Paper No. 2004-0530, January 2004.
- [49] J. R. Debonis, N. J. Georgiadis, and C. F. Smith. Validation of the NPARC code for nozzle afterbody flows at transonic speeds. AIAA Paper No. 1995-2614, July 1995.
- [50] N. J. Georgiadis and D. A. Yoder. Use of Navier-Stokes methods for the calculation of high-speed nozzle flow fields. AIAA Paper No. 1994-3212, June 1994.
- [51] N. J. Georgiadis, J. C. Dudek, and T. P. Tierney. Grid resolution and turbulent inflow boundary condition recommendations for NPARC calculations. AIAA Paper No. 1995-2613, July 1995.
- [52] T. J. Barber, L. M. Chiappetta, J. R. Debonis, N. J. Georgiadis, and D. A. Yoder. Assessment of parameters influencing the prediction of shear-layer mixing. *Journal of Propulsion and Power*, 15(1):45–53, 1999.
- [53] H. Salman. *Numerical Simulation of Streamwise Vorticity Enhanced Mixing*. PhD thesis, Loughborough University, January 2001.
- [54] H. Salman, J. J. McGuirk, and G. J. Page. A numerical study of vortex interactions in lobed mixer flow fields. AIAA Paper No. 1999-3409, 1999.
- [55] J. E. Bardina, P. G. Huang, and T. J. Coakley. Turbulence modeling validation, testing, and development. NASA TM-1997-110446, April 1997.
- [56] S. L. Woodruff, J. M. Seiner, M. Y. Hussaini, and G. Erlebacher. Evaluation of turbulence model performance in jet flows. *AIAA Journal*, 39(12):2402–2404, 2001.
- [57] M. Mani, J. A. Ladd, A. B. Cain, and R. H. Bush. An assessment of one- and two-equation turbulence models for internal and external flows. AIAA Paper No. 1997-2010, June 1997.
- [58] A. B. Lebedev, A. D. Lyubimov, V. P. Maslov, B. I. Mineev, A. N. Secundov, and S. F. Birch. The prediction of three-dimensional jet flows for noise applications. AIAA Paper No. 2002-2422, May 2002.
- [59] S. B. Pope. An explanation of the turbulent round-jet/plane-jet anomaly. *AIAA Journal*, 16:279–281, 1978.
- [60] S. F. Birch, D. A. Lyubimov, A. N. Secundov, and K. Yakubovsky. Numerical modeling requirements for coaxial and chevron nozzle flows. AIAA Paper No. 2003-3287, May 2003.

- [61] S. F. Birch, D. A. Lyubimov, A. N. Secundov, and K. Yakubovsky. Accuracy requirements of flow inputs for jet noise prediction codes. AIAA Paper No. 2004-2934, May 2004.
- [62] A. T. Thies and C. K. W. Tam. Computation of turbulent axisymmetric and nonaxisymmetric jet flows using the $k-\epsilon$ model. *AIAA Journal*, 34(2):309–316, 1996.
- [63] C. K. W. Tam and A. Ganesan. Modified $k-\epsilon$ turbulence model for calculating hot jet mean flows and noise. *AIAA Journal*, 42(1):26–34, 2004.
- [64] N. J. Georgiadis, D. A. Yoder, and W. A. Engblom. Evaluation of modified two-equation turbulence models for jet flow predictions. AIAA Paper No. 2006-0490, January 2006.
- [65] K. S. Abdol-Hamid, S. P. Pao, S. J. Massey, and A. Elmiligui. Temperature corrected turbulence model for high temperature jet flow. AIAA Paper No. 2003-4070, June 2003.
- [66] W. A. Engblom, N. J. Georgiadis, and A. Khavaran. Investigation of variable-diffusion turbulence model correction for round jets. AIAA Paper No. 2005-3085, May 2005.
- [67] D. C. Kenzakowski, J. Shipman, S. M. Dash, J. Bridges, and N. Saiyed. Study of three-stream laboratory jets with passive mixing enhancements for noise reduction. AIAA Paper No. 2000-0219, January 2000.
- [68] D. C. Kenzakowski, J. Papp, and S. M. Dash. Evaluation of advanced turbulence models and variable Prandtl/Schmidt number methodology for propulsive flows. AIAA Paper No. 2000-0885, January 2000.
- [69] D. C. Kenzakowski, J. L. Papp, and S. M. Dash. Modeling turbulence anisotropy for jet noise prediction. AIAA Paper No. 2002-0076, January 2002.
- [70] J. L. Papp, D. C. Kenzakowski, and S. M. Dash. Calibration and validation of EASM turbulence model for jet flowfields. AIAA Paper No. 2002-0855, January 2002.
- [71] D. C. Kenzakowski, C. Kannepalli, and K. W. Brinckman. Computational studies supporting concepts for supersonic jet noise reduction. AIAA Paper No. 2004-0518, January 2004.
- [72] D. C. Kenzakowski. Turbulence modeling improvements for jet noise prediction using PIV datasets. AIAA Paper No. 2004-2978, May 2004.
- [73] D. C. Kenzakowski and J. L. Papp. EASM/J extensions and evaluation for jet noise prediction. AIAA Paper No. 2005-0419, January 2005.
- [74] K. W. Brinckman, D. C. Kenzakowski, and S. M. Dash. Progress in practical scalar fluctuation modeling for high-speed aeropropulsive flows. AIAA Paper No. 2005-0508, January 2005.
- [75] D. C. Kenzakowski and C. Kannepalli. Jet simulation for noise prediction using advanced turbulence modeling. AIAA Paper No. 2005-3086, May 2005.

- [76] V. G. Mengle and W. N. Dalton. Lobed mixer design for noise suppression: Volume 1. NASA CR-2002-210823/VOL1, July 2002.
- [77] V. G. Mengle, V. D. Baker, and W. N. Dalton. Lobed mixer design for noise suppression: Volume 2. NASA CR-2002-210823/VOL2, July 2002.
- [78] V. Mengle, W. Dalton, J. Bridges, and K. Boyd. Noise reduction with lobed mixers: Nozzle length and free-jet speed effects. AIAA Paper No. 1997-1682, May 1997.
- [79] V. Mengle. Jet noise reduction by lobed mixers with boomerang scallops. AIAA Paper No. 1999-1923, May 1999.
- [80] V. Mengle. Finding excess noise in internally-mixed jets by varying free-jet speed. AIAA Paper No. 1999-1967, May 1999.
- [81] V. Mengle. Anomalous effect of nozzle length reduction on jet noise of forced mixers. AIAA Paper No. 1999-1968, May 1999.
- [82] V. Mengle. Optimization of lobe mixer geometry and nozzle length for minimum jet noise. AIAA Paper No. 2000-1963, June 2000.
- [83] C. W. Wright, G. A. Blaisdell, and A. S. Lyrintzis. Using RANS to predict the performance of mixers in reducing jet noise. AIAA Paper No. 2004-1274, January 2004.
- [84] C. W. Wright. Investigating correlations between Reynolds averaged flow fields and noise for forced mixed jets. Master's thesis, School of Aeronautics and Astronautics, Purdue University, West Lafayette, IN, May 2004.
- [85] C. W. Wright, G. A. Blaisdell, and A. S. Lyrintzis. The effects of various mixer shapes on jet noise. AIAA Paper No. 2003-3251, May 2003.
- [86] M. Salikuddin, S. Martens, H. Shin, and R. K. Majjigi. Acoustic and laser doppler anemometer results for confluent, 22-lobed, and unique-lobed mixer exhaust systems for subsonic jet noise reduction. NASA CR-2002-211598, September 2002.
- [87] R. Pinker and P. Strange. The noise benefits of forced mixing. AIAA Paper No. 1998-2256, May 1998.
- [88] S. C. M. Yu and X. G. Xu. Flow characteristics of a confined co-axial nozzle with a central lobed mixer at different velocity ratios. AIAA Paper No. 1997-1811, 1997.
- [89] S. C. M. Yu, T. H. Yip, and C. Y. Liu. Mixing characteristics of forced mixers with scalloped lobes. *Journal of Propulsion and Power*, 13(2):305–311, 1997.
- [90] N. H. Saiyed, J. E. Bridges, and E. A. Krejsa. Core and fan streams' mixing noise outside the nozzle for subsonic jet engines with internal forced mixers. NASA TM-1996-107237, July 1996. Also published as AIAA Paper No. 1996-1667.
- [91] H.-W. Shin and R. R. Babbitt. Experimental study of exhaust system mixers for a subsonic jet noise reduction. AIAA Paper No. 1996-2650, 1996.

- [92] J. P. Meade. Acoustic evaluation of a forced mixer on a high bypass ratio engine. AIAA Paper No. 1994-2954, June 1994.
- [93] J. K. Elliott, T. A. Manning, Y. J. Qiu, E. M. Greitzer, C. S. Tan, and T. G. Tillman. Computational and experimental studies of flow in multi-lobed forced mixers. AIAA Paper No. 1992-3568, July 1992.
- [94] M. J. Werle, R. W. Paterson, and W. M. Presz. Flow structure in a periodic axial vortex array. AIAA Paper No. 1987-0610, January 1987.
- [95] S. M. Birch, G. C. Paynter, D. B. Splading, and D. G. Tatchell. Numerical modeling of three-dimensional flows in turbofan engine exhaust nozzles. *Journal of Aircraft*, 15(8):489–496, 1978.
- [96] M. Soteriou, R. Reba, and T. Maeder. Numerical study of the impact of streamwise vorticity on noise generation by jet flows. AIAA Paper No. 2002-2480, June 2002.
- [97] K. B. M. Q. Zaman and C. K. W. Tam. Flow and noise field of subsonic jets from asymmetric nozzles. AIAA Paper No. 1999-3583, 1999.
- [98] K. B. M. Q. Zaman, F. Y. Wang, and N. J. Georgiadis. Noise, turbulence, and thrust of subsonic freejets from lobed nozzles. *AIAA Journal*, 41(3):398–406, 2003.
- [99] L. A. Garrison, A. S. Lyrintzis, G. A. Blaisdell, and W. N. Dalton. Computational fluid dynamics analysis of jets with internal forced mixers. AIAA Paper No. 2005-2887, May 2005.
- [100] L. A. Garrison, A. S. Lyrintzis, and G. A. Blaisdell. RANS-based noise predictions of jets with internal forced mixers. AIAA Paper No. 2006-2599, May 2006.
- [101] B. J. Tester, M. J. Fisher, L. A. Garrison, A. S. Lyrintzis, and G. A. Blaisdell. Understanding and prediction of lobed mixer jet noise. Aeroacoustics Research Consortium Final Report, July 2005.
- [102] B. J. Tester, M. J. Fisher, L. A. Garrison, A. S. Lyrintzis, and G. A. Blaisdell. Understanding and prediction of lobed mixer jet noise: Phase II. Aeroacoustics Research Consortium, Final Report, November 2006.
- [103] J. Bridges and M. P. Wernet. Cross-stream PIV measurements of jets with internal lobed mixers. AIAA Paper No. 2004-2896, May 2004.
- [104] NPARC Alliance. WIND v5.0 user's guide. NASA Glenn Research Center and USAF Arnold Engineering Development Center, May 2004.
- [105] R.H. Bush, G. D. Power, and C. E. Towne. WIND: The production flow solver of the NPARC alliance. AIAA Paper No. 1998-0935, January 1998.
- [106] P. R. Spalart and S. R. Allmaras. A one-equation turbulence model for aerodynamic flows. AIAA Paper No. 1992-0439, January 1992.
- [107] F. Menter. Two-equation eddy-viscosity turbulence models for engineering applications. *AIAA Journal*, 32(8):1598–1605, 1994.

- [108] K. Y. Chien. Predictions of channel and boundary layer flows with a low-Reynolds number turbulence model. *AIAA Journal*, 20(1):33–38, 1982.
- [109] C. Rumsey, T. Gatski, and J. Morrison. Turbulence model predictions of strongly curved flow in a u-duct. *AIAA Journal*, 38(8):1394–1402, 2000.
- [110] C. Rumsey and T. Gatski. Recent turbulence model advances applied to multi-element airfoil computations. *Journal of Aircraft*, 38(5):904–910, 2001.
- [111] D. A. Yoder. Initial evaluation of an algebraic Reynolds stress model for compressible turbulent shear flows. AIAA Paper No. 2003-0548, January 2003.
- [112] P. A. O. Davies, M. J. Fisher, and M. J. Barratt. The characteristics of the turbulence in the mixing region of a round jet. *Journal of Fluid Mechanics*, 15:337–367, 1963.
- [113] P. Bradshaw, D. H. Ferriss, and R. F. Johnson. Turbulence in the noise-producing region of a circular jet. *Journal of Fluid Mechanics*, 19:591–624, 1964.
- [114] N. W. M. Ko and P. A. O. Davies. The near field within the potential cone of subsonic cold jets. *Journal of Fluid Mechanics*, 50:49–78, 1971.
- [115] J. C. Lau, P. J. Morris, and M. J. Fisher. Measurements in subsonic and supersonic free jets using a laser velocimeter. *Journal of Fluid Mechanics*, 93:1–27, 1979.
- [116] K. B. Q. Zaman. Flow field and near and far sound field of a subsonic jet. *Journal of Sound and Vibration*, 106(1):1–16, 1986.
- [117] N. W. M. Ko and A. S. H. Kwan. The initial region of subsonic coaxial jets. *Journal of Fluid Mechanics*, 73:305–332, 1976.
- [118] L. A. Garrison. Jet noise models for forced mixer noise predictions. Master’s thesis, School of Aeronautics and Astronautics, Purdue University, West Lafayette, IN, December 2003.
- [119] L. A. Garrison, W. N. Dalton, A. S. Lyrintzis, and G. A. Blaisdell. An investigation of the extension of the four-source method for predicting the noise from jets with internal forced mixers. AIAA Paper No. 2003-3165, May 2003.
- [120] L. A. Garrison, W. N. Dalton, A. S. Lyrintzis, and G. A. Blaisdell. Semi-empirical noise models for predicting the noise from jets with forced mixers. AIAA Paper No. 2004-2898, May 2004.
- [121] B. J. Tester, M. J. Fisher, and W. N. Dalton. A contribution to the understanding and prediction of jet noise generation in forced mixers. AIAA Paper No. 2004-2897, May 2004.
- [122] B. J. Tester and M. J. Fisher. A contribution to the understanding and prediction of jet noise generation in forced mixers: Part II flight effects. AIAA Paper No. 2005-3094, May 2005.
- [123] M. J. Fisher, M. Harper-Bourne, and S. A. L. Glegg. Jet noise source location: The polar correlation technique. *Journal of Sound and Vibration*, 51(1):23–54, 1977.

- [124] B. J. Tester and M. J. Fisher. Engine noise source breakdown: Theory, and simulation results. AIAA Paper No. 1981-2040, 1981.
- [125] S. S. Lee and J. Bridges. Phased-array measurements of single flow hot jets. AIAA Paper No. 2005-2842, May 2005.
- [126] S. S. Lee. Phased-array study of jets with various internal mixers and nozzles. NASA CR-2005-213870, September 2005.
- [127] B. J. Tester and M. J. Fisher. 21stCentury jet noise test data appraisal. ISVR Consultancy Ref:6920-Final Report, November 2003.
- [128] H. S. Ribner. Convection of a pattern of vorticity through a shock wave. NACA TR-1164, 1954.
- [129] H. S. Ribner. Shock-turbulence interaction and the generation of noise. NACA TR-1233, 1955.
- [130] H. S. Ribner. Spectra of noise and amplified turbulence emanating from shock-turbulence interaction. *AIAA Journal*, 25(3):436–442, 1986.
- [131] S. B. Pope. *Turbulent Flows*. Cambridge University Press, 2000.

APPENDICES

A. PIV Data Processing

As part of the 2003 NASA Glenn / Rolls-Royce Corporation lobed mixer experimental test program Particle Image Velocimetry (PIV) data was acquired for six mixers (confluent, 12CL, 12UM, 12UH, 20UH, 20DH) with the baseline L0 nozzle at set point 312. Additional PIV data was also taken for the confluent mixer at set point 5000, and for the 12CL mixer at set points 112 and 310. The PIV data was acquired using a dual camera stereoscopic PIV apparatus arranged to record data in planes perpendicular to the jet axis. Using this procedure, all three components of the mean and RMS velocities were measured. For each data point, twelve planes of PIV data were acquired downstream of the final nozzle exit at X/D locations of 0.1, 0.2, 0.3, 0.5, 0.7, 1, 1.4, 2, 3, 5, 7, and 10. The PIV data planes were centered to capture approximately one quadrant of the jet cross-section and supplied on a Cartesian grid (137×103).

Preliminary analysis of the PIV data issued by the NASA Glenn Research center revealed that the jet centerline axis was misaligned with the origin of the PIV data reference frame. The effects of this misalignment are most obvious at the farthest downstream plane ($X/D = 10$) as shown in Figure A.1, where it appears that for many cases the PIV data does not even capture the jet centerline. To resolve this issue a procedure was developed to numerically determine the location of the jet centerline in each plane of PIV data by evaluating the mean axial velocity field. First, 50 velocity bands are defined ranging from a value of $V_o + 1/2(V_s - V_o)$ to $V_o + 7/8(V_s - V_o)$. These velocities will correspond to velocities seen in the middle of the ambient-bypass shear layer. Next, all points in a given plane of the PIV data that fall within a given band are determined. The coordinates of these points are supplied to an optimization function that determines the virtual origin that yields the smallest variance in the calculated radii for all of the selected points. This process

is repeated for each velocity band, resulting in 50 estimates for the jet centerline. These values are then averaged to yield the final jet centerline location for a given plane of PIV data. This centerline location process was repeated for each plane of PIV data.

An example of the results of the centerline location process are shown for the PIV data of the 12CL mixer at set point 310 in Figure A.2. In this figure the white ‘x’ markers represent the 50 calculated centerline locations and the final averaged centerline location is shown with a bold blue ‘x’. In addition, the original PIV reference frame axes are shown by the white dashed lines. The final averaged centerline locations for each plane of PIV data are shown in Figure A.3. It is assumed that the shift in the centerline location is due to a simple misalignment of the PIV and jet centerline axes. In addition it is assumed that the PIV reference frame was centered on the jet centerline at the nozzle exit. Based on these assumptions a linear fit is assumed for the horizontal and vertical shifts in the jet centerline, with a value of 0 at the nozzle exit plane (PIV data and jet reference frames are assumed to be coincident at $X/D=0$). The assumed linear shift is then applied to all of the PIV data planes.

Once the centerline location of the PIV data was shifted the data in each plane was then interpolated from the cartesian grid to a uniform polar grid. This process was performed to aid in further post-processing and comparison with the CFD results. In particular, this process greatly simplified the azimuthal averaging of the PIV data. The uniform grid was constructed using a uniform radial and azimuthal spacing (100×97). The dimensions of the uniform polar grid were selected so that the resolution near the main jet shear layer would be similar to that of the cartesian grid. An example of the cartesian and cylindrical grids are shown in Figure A.4.

During the course of this research project a number of questions were raised concerning the quality of the PIV data. These issues resulted from observations in differences between PIV data that were processed in the beginning of the experimental program (‘June 2003 data’) and the data that were issued at the end of the test

program ('October 2003 data'). In particular, it was noticed that the 'June 2003' data appeared to have a higher quality parameter, which is calculated for each point in the flow field based on the ratio of the number of rejected velocity vectors to the total number of velocity vectors (200 image pairs were taken for each plane of PIV data). In addition, the earlier data showed better trends in the turbulence intensities, particularly in the downstream planes when compared to the 'October 2003' data. It was observed that the 'June 2003' data showed a more uniform distribution of turbulence kinetic energy in the far downstream planes, which is expected in the fully mixed jet region. On the other hand, the 'October 2003' data showed patches of relatively high turbulence levels in the far downstream plane, particularly for the 12UM and 12UH configurations. After discussing these differences in the two data sets with the researchers at the NASA Glenn Research Center it was learned that a different method was used to post-process the PIV data for the 'October 2003' data. In particular, for this data set when converting the particle images to velocity vectors the individual PIV data particle images were artificially warped in an attempt to account for refraction effects as the light passed from the particle location through the density gradients in the heated jet shear layer. Using this technique, the warping for each image was determined by finding the lowest variance in the mean velocity field. It is believed that although this approach may have improved the mean velocities, it adversely affected the calculated turbulence intensities. Unfortunately the 'June 2003' processed data files were no longer available from the NASA Glenn Research Center. Consequently, the only the 'October 2003' PIV data files were utilized in the current research work.

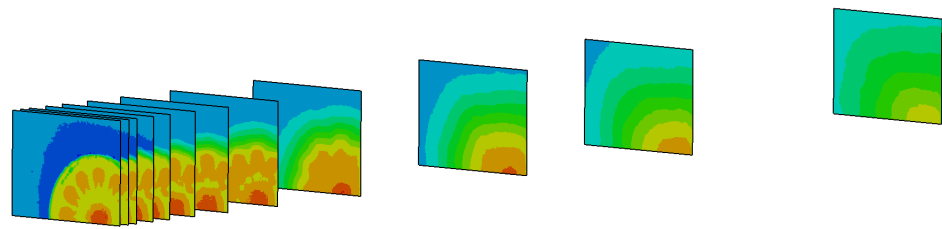


Figure A.1. PIV data mean streamwise velocities in the jet plume for the 12CL mixer at set point 310.

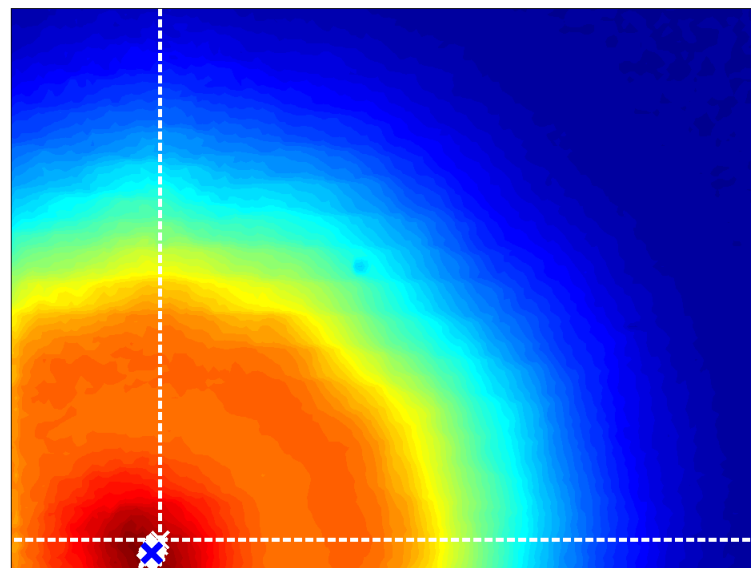


Figure A.2. PIV data jet centerline location results for the 12CL mixer at set point 310.

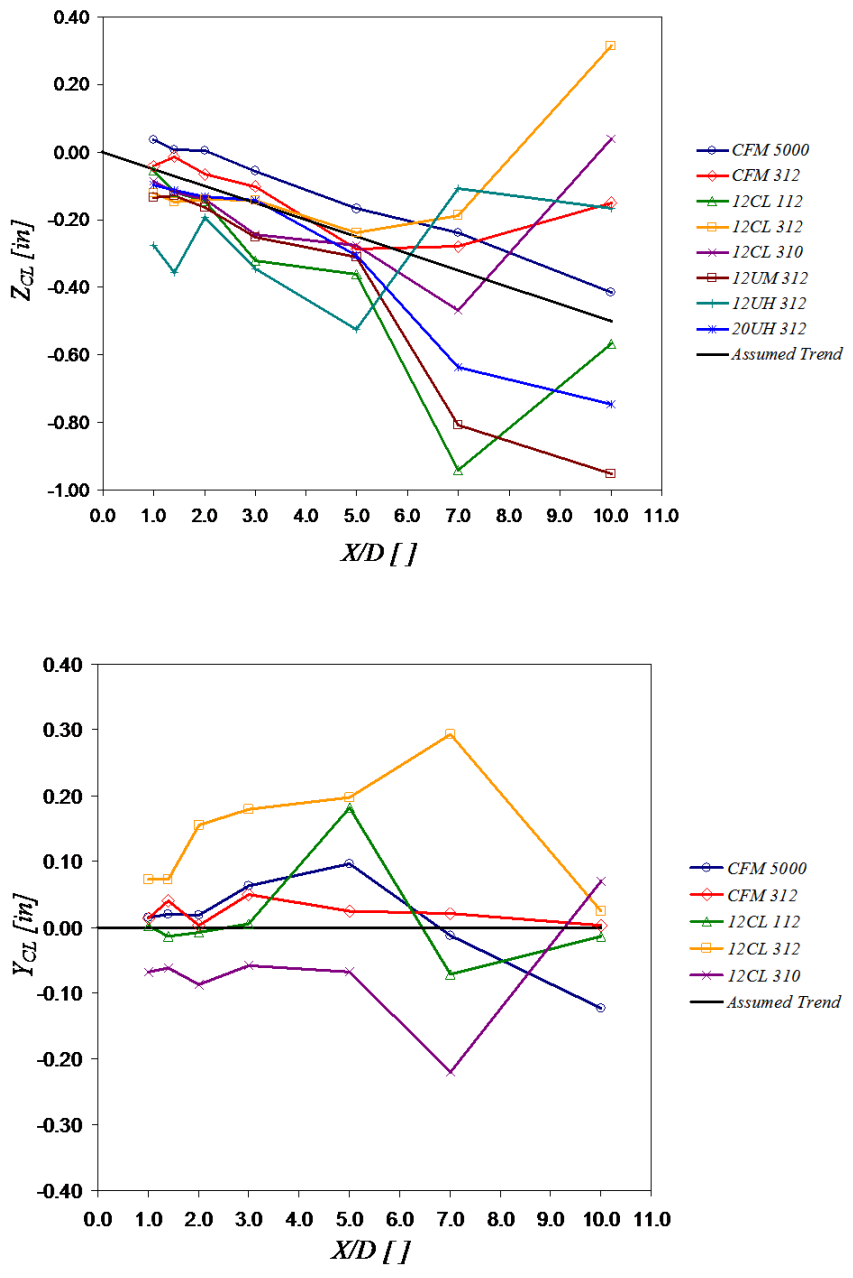


Figure A.3. PIV data final averaged jet centerline location results:
(a) vertical shift, (b) horizontal shift.

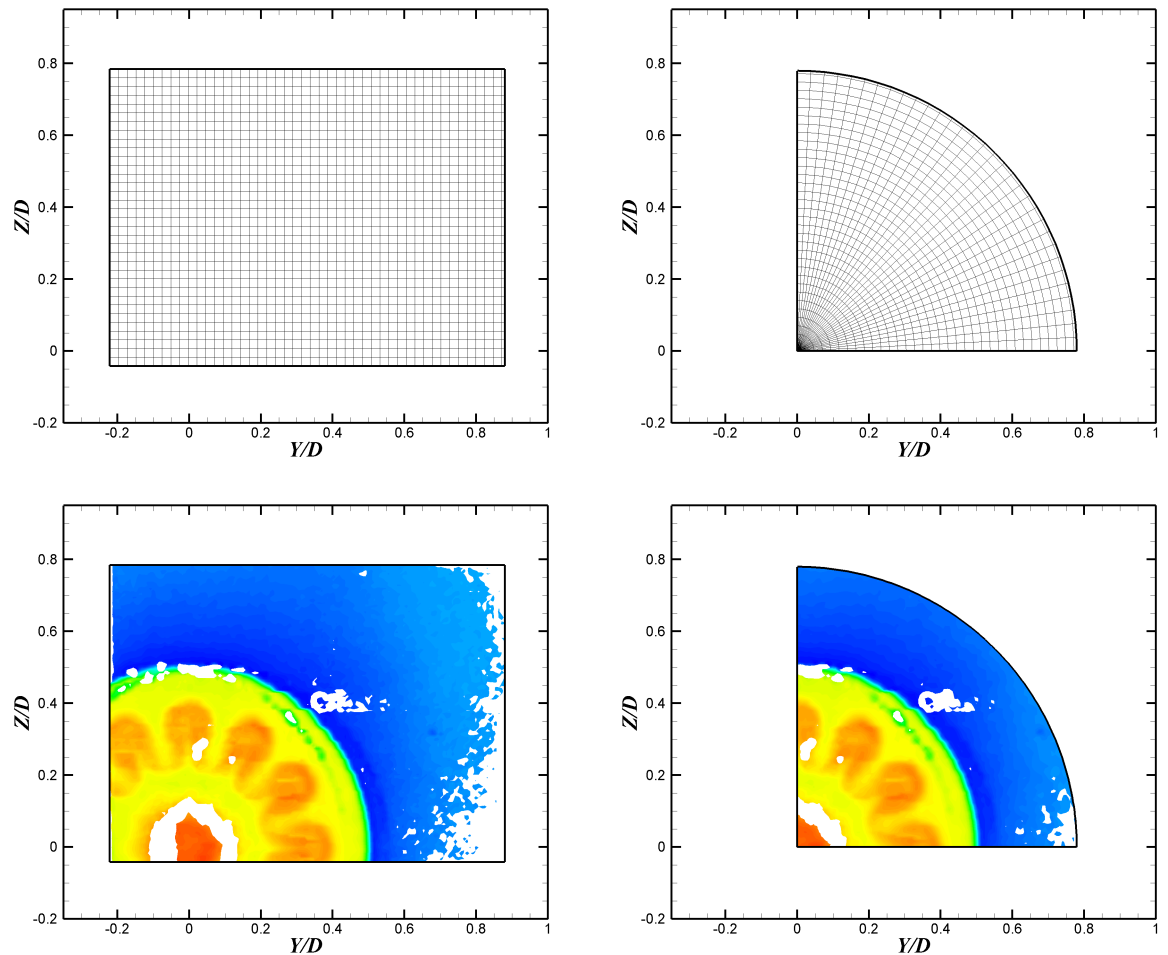


Figure A.4. Comparison of the Cartesian and cylindrical PIV data grids (every 3rd grid point is shown).

B. Grid Generation

To facilitate the grid generation process a small Matlab toolbox was developed. This toolbox consisted of a number of functions that aid in the generation of 1-D and 2-D grids. In particular functions were developed that space points along an arbitrary arc length using linear, exponential, or hyperbolic tangent spacings. Also, a 2-D transfinite interpolation (TFI) function was developed. These routines were used in the development of both the axisymmetric confluent mixer and 3-D lobed mixer grids.

The computational grids for the axisymmetric confluent mixer cases are generated using a Matlab script. The computational domain for the confluent mixer is divided into 6 primary zones as shown in Figure B.1. The confluent mixer grid generator script builds each zone separately in the order listed in Figure B.1. During this process grid points are packed in regions where the flow field has large gradients. Four regions of particular interest are the wall boundary layers, the primary/secondary flow shear layer, the main jet shear layer, and the nozzle exit. Points are packed near the nozzle exit to resolve the normal shock that occurs at the high power set points (310 and 312). Grid points are packed near all of the solid surface boundaries to resolve the wall boundary layers. These boundaries are the tailcone, the mixer splitter plate surface, and the nozzle wall surfaces. Grid points are also packed in the shear layer regions. For each zone the boundary grid points are defined using either geometric relations or database values for the solid wall surfaces. The interior points for each of the zones are determined using 2-D transfinite interpolation.

The boundary grid point spacing specifications for each zone are shown in Figures B.2 to B.6. For zones 1 and 2 the radial grid points are spaced using a two-sided hyperbolic tangent stretching function and the axial grid points are linearly spaced. The zone boundary point specifications for zone 3 are shown in Figure B.3. For

this zone the upstream boundary points are determined from zones 1 and 2. The axial grid points are linear spaced. The downstream boundary uses a quadratic profile to improve the quality of the cells near the end of the tailcone. Zone 3 is constructed in two parts, one that spans from the tailcone surface to the middle of the primary/secondary shear layer, and a second that spans from the middle of the shear layer to the nozzle wall. The location of the shear layer edges are determined from a previous CFD solution of the confluent mixer configuration. A Fortran code was developed to extract the edges of the primary/secondary shear layer based on total temperature profiles inside the nozzle. These shear layer edge locations are then supplied to the Matlab confluent mixer grid generation code. In each half of zone 3 a small region from the shear layer mid point to the shear layer edge is linearly spaced. Two-sided hyperbolic tangent spacing is used for the remainder of the radial grid points. A similar process is used in the definition of the grid points for zone 4 as shown in Figure B.4. In zone 4 two-sided hyperbolic tangent spacing is used for the axial grid points to pack points near the nozzle exit. One-sided hyperbolic tangent spacing is used for both the axial and radial grid points for zone 5, as shown in Figure B.5. The plume region (zone 6) is created in three parts, as shown in Figure B.6. The first section spans from the nozzle exit to the approximate location where the primary-secondary and secondary-ambient shear layers begin to merge. The second section spans from this point to the approximate location of the end of the primary flow potential core. The final section spans from this location to the domain exit. Equal spacing is used to define the radial distribution of points inside the shear layer. One-sided hyperbolic tangent spacing is used for the radial spacing of points outside the shear layer and for the axial distribution.

The three dimensional lobed mixer grid are generated using a combination of Matlab scripts and Gridgen, a commercial grid generating program. In this process the faces for the 3-D zones are defined using a Matlab script. The axial and radial spacing for each zone is determined by a process similar to the previously described method for the confluent mixer grids. In addition, a constant azimuthal spacing

is used for each zone of the lobed mixer grids. The Matlab script writes the grid point information from all of the zone faces to a plot3d formatted grid file. The surface grids points for each of the zone faces are then loaded into Gridgen. The grid points on these faces are then smoothed to improve the grid quality using Gridgen's elliptical solver. Interior points are then generated by Gridgen using 3-D transfinite interpolation. The grid cells are checked for negative volumes and skewed edges. Finally the full grid is exported in plot3d format.

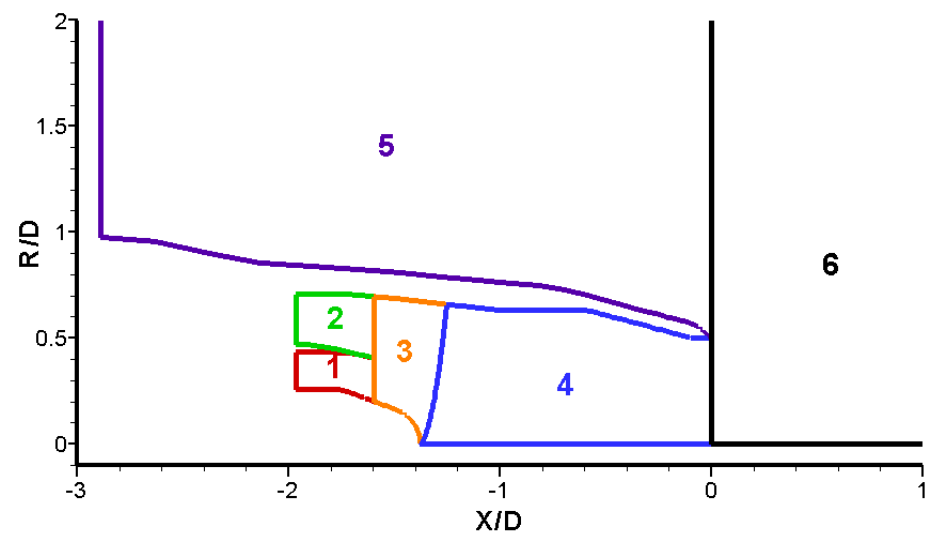


Figure B.1. Zone arrangement for the confluent mixer grid.

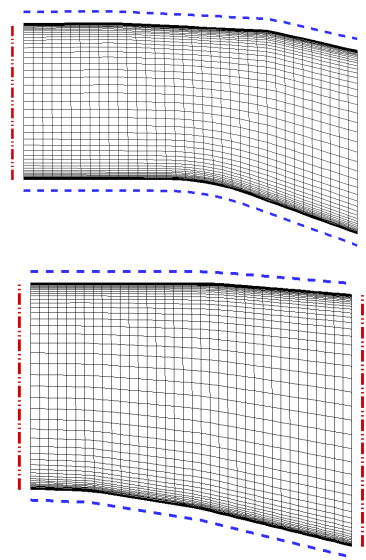


Figure B.2. Boundary grid point specification for zones 1 and 2.

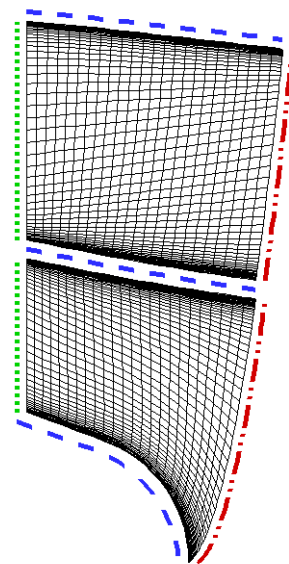


Figure B.3. Boundary grid point specification for zone 3.

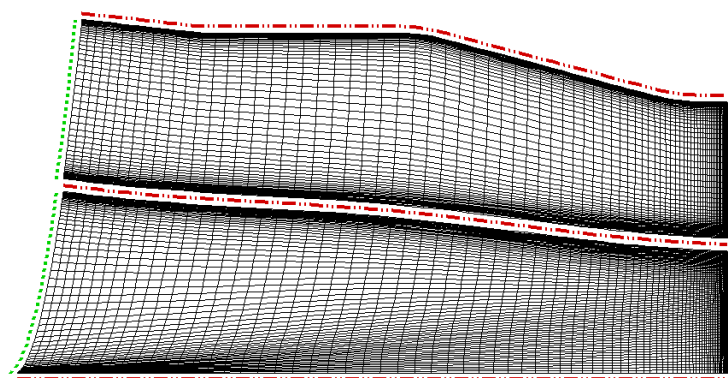


Figure B.4. Boundary grid point specification for zone 4.

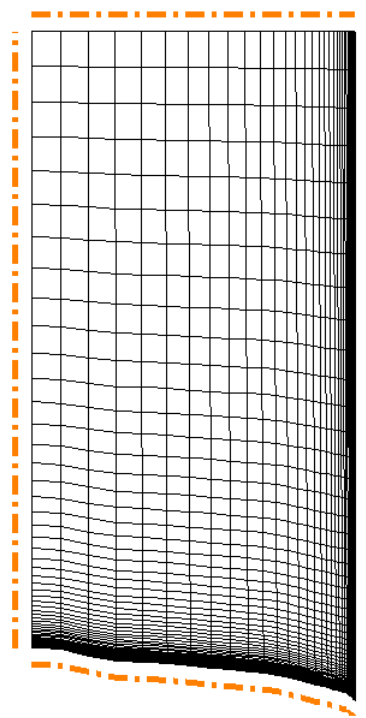


Figure B.5. Boundary grid point specification for zone 5.

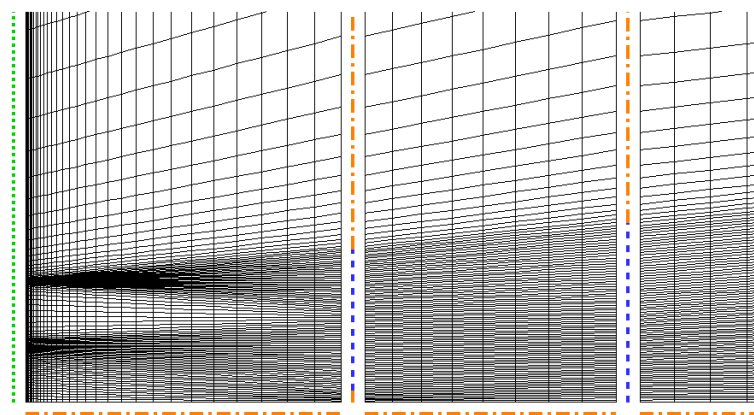


Figure B.6. Boundary grid point specification for zone 6 (every other grid point is shown).

VITA

VITA

Loren Garrison received his B.S in Aeronautical and Astronautical Engineering in May of 1997 from Purdue University. He continued studying at Purdue University and received his M.S. in Aeronautical and Astronautical Engineering in December of 2001 under the direction of Professor A. S. Lyrintzis and Professor G. A. Blaisdell. As part of his masters thesis he researched the application of semi-empirical noise models for jets with internal forced mixers as part of a project funded by the Indiana 21st Century Research and Technology Fund. During this time he spent a semester in the Fall of 2002 as a visiting researcher at the Institute of Sound and Vibration Research (ISVR) in Southampton, UK. Following the completion of his masters, he continued his graduate work at Purdue and begin doctoral level studies in the Spring of 2004. His Doctoral research focused on computational fluid dynamics analysis and noise prediction of jets with internal forced mixers. His Doctoral research work was funded partly the Aeroacoustics Research Consortium as part of a joint project with Dr. Brian Tester and Dr. Mike Fisher at the ISVR. Throughout his graduate research he has worked closely with researchers at the ISVR and at the Rolls-Royce Corporation, where he spent the summer of 2001 and 2004 as an intern. After completing his Ph.D. degree in May 2006 he will be joining the Design Methods and Technology division of the Rolls-Royce Corporation in Indianapolis, Indiana.